Rayleigh wave method for measuring the frequency-dependent shear modulus of soft biomaterials

Marius Joannis Müller

Master of Engineering

Mechanical Engineering

McGill University

Montreal,Quebec

November 2017

A dissertation submitted to McGill University in partial fulfillment of the requirements for the degree of Master of Engineering

ABSTRACT

This thesis investigates the dynamics of Rayleigh and compressional wave propagation in viscoelastic materials. A variety of experiments were performed and computational models were created to quantify homogeneous and inhomogeneous material properties. The present research highlights the mathematical and physical principles of Rayleigh wave propagation. A basic mathematical model for single- and multi-mode Rayleigh wave propagation was created. Model predictions were used to interpret experimental observations. Spectral analysis in the wavenumber-frequency domain was performed to provide detailed information about the wave propagation phenomena, obtained both numerically and experimentally. The frequency-dependent viscoelastic material properties of silicon rubbers and one injectable hydrogel biomaterial were quantified based on the Rayleigh wave method and torsional rheometry. Compressional wave propagation experiments were performed using a traveling wave approach for verification purposes. The measured wave speed and the dispersion curves confirmed the results from the Rayleigh wave experiment. Viscoelastic inhomogeneous structures with embedded nylon fibers were then investigated. The influence of the fibers on the anisotropy of the wave propagation was analyzed. A detailed numerical simulation of the laboratory experiment was finally performed. The results were found to be in agreement with measured data, thereby validating the approach. A parametric study uncovered the possibility to adjust material parameters to fit the numerical envelope function of the peak amplitudes obtained from experimental data. The simulation and experimental methods enabled the inverse

determination of the frequency-dependent material properties up to a frequency of 2 kHz.

ABRÉGÉ

Ce travail de thèse avait pour but d'étudier le comportement dynamique de la propagation d'ondes de Rayleigh et de compression dans des matériaux viscoélastiques. Diverses mesures exprimentales ont été faites et des modèles numériques ont été construits afin de quantifier les propriétés homogènes et inhomogènes des matériaux. Le présent travail met en evidence les principes physiques et mathématiques de la propagation d'ondes de Rayleigh. Des modèles mathématiques de propagation unimodale ou multimodale d'ondes de Rayleigh ont été développés. Les prédictions ont permis d'interpréter les comportements expérimentaux observés. L'analyse spectrale dans le domaine nombre d'onde versus fréquence a été utiliseée afin d'obtenir des informations détaillées sur la vitesse de propagation d'ondes, tant expérimentalement que numériquement. Les propriétés du silicone et d'un biomatériau, un hydrogel injectable, ont été quantifiées en fonction de la fréquence grâce à la théorie d'ondes de Rayleigh et à un rhéomètre de torsion. Les résultats confirment les tendances observées pour les ondes de Rayleigh. Des matériaux viscoélastiques inhomogènes avec des fibres de nylon incorporées ont ensuite été étudiés. L'influence des fibres sur l'anisotropie de propagation de l'onde a été analysée. Dans le cas des ondes progressives, il a été observé que l'approche d'onde stationnaire n'était pas appropriée pour de hautes fréquences. Un model d'onde progressive de compression a été implémenté. Une simulation numérique détaillée de l'expérience en laboratoire a été exécutée. Les résultats obtenus correspondent aux données expérimentales,

validant ainsi cette approche. Une étude paramétrique a mis en avant la possibilité d'ajuster les paramètres des matériaux pour faire correspondre la fonction d'enveloppe obtenue numériquement avec les données expérimentales. Les méthodes numériques et expérimentales ont ainsi permis l'identification inverse des propriétés matériau jusqu'à une fréquence de 2 kHz.

TABLE OF CONTENTS

LIST OF TABLES

LIST OF FIGURES

NOMENCLATURE

Roman symbols

E'	Real part of the elastic modulus
E''	Imaginary part of the elastic modulus
$\hat{E}$	Complex elastic modulus
G'	Real part of the shear modulus
G''	Imaginary part of the shear modulus
$\hat{G}$	Complex shear modulus
f	Frequency
h	Sample thickness
$\hat{k}_C$	Complex compressional wavenumber
$\hat{k}_R$	Complex Rayleigh wavenumber
$\hat{k}_S$	Complex shear wavenumber
$\hat{c}_S$	Complex shear wave speed
$\hat{c}_C$	Complex compressional wave speed
$\hat{c}_{bk}$	Complex bulk velocity
L	Distance between two locations on the surface of the sample
$\hat{H}(\omega)$	Transfer function
$\bar{u}$	Displacement vector
$\bar{u}_n$	Nodal displacement vector
$\hat{u}_{x_1}$	Displacement along x_1-direction
$\hat{u}_{x_2}$	Displacement along x_2-direction
v_{x_1}	Velocity along x_1-direction

v_{x_2}	Velocity along x_2-direction
a_1	Amplitude of the compressional wave potential in the first layer
b_1	Amplitude of the compressional wave potential in the first layer
c_1	Amplitude of the shear wave potential in the first layer
d_1	Amplitude of the shear wave potential in the first layer
b_2	Amplitude of the compressional wave potential in the second layer
d_2	Amplitude of the shear wave potential in the second layer
h	sample thickness
m	added mass
$\bar{F}(t)$	Load vector
M	Termination mass
$\bar{\bar{M}}$	Mass matrix
A_f	Simulation amplitude coefficient
A_d	Normalized displacement amplitude
$\bar{\bar{A}}_c$	Coefficient matrix
C	Courant-Friedrichs-Lewy number
$\bar{\bar{C}}$	Damping matrix
$\bar{\bar{K}}$	Stiffness matrix
$\mathcal{Q}$	Volume velocity
$\mathcal{H}$	Hilbert transform
$H_n^{(x)}$	Hankel function of n'th order and x'th kind
J_n	Zeroth order Bessel functions of the n'th kind
T	Temperature

l	Sample length
d	Sample Diameter
d_i	Incompressibility parameter
t	time
	Greek symbols
α	Imaginary part of the compressional wavenumber
α_d	Mass-proportional Rayleigh damping
β	Real part of the compressional wavenumber
β_d	Stiffness-proportional Rayleigh damping
$\hat{\lambda}(\omega)$	Frequency-dependent Lame function
$\hat{\mu}(\omega)$	Frequency-dependent Lame function
ν	Poissons ratio
ρ	Density
δ_{ij}	Kronecker delta
δ	Phase angle
ϵ_{ij}	Strain tensor components
σ_{ij}	Stress tensor components
ω	Angular frequency
ϕ	Compressional wave potential
ψ	Shear wave potential
$\bar{\psi}$	Shear wave vector potential
φ	Phase of the transfer function
η	Loss factor

λ	Real part of the Rayleigh wavenumber
λ_{bk}	Bulk wave wavelength
λ_S	Shear wave wavelength
λ_R	Rayleigh wave wavelength
γ	Imaginary part of the Rayleigh wavenumber
ζ	Damping ratio
$\bar{\psi}$	Normalized eigenvector
$\bar{\xi}$	Transformed displacement

CHAPTER 1
Introduction

1.1 Overview

Viscoelastic materials are increasingly used over a wide range of biomedical applications. In the field of tissue engineering, viscoelastic materials have been used to help tissue regeneration following injury. One typical example is the injection of a viscoelastic material into vocal fold scar [1]. Scaring increases the stiffness of vocal fold tissue due to an increase in amount of collagen type I, in contrast to unscarred tissue which has a higher density of collagen type III [2]. This change in stiffness has a significant impact on voice production. Voice is created by an oscillatory motion of the vocal folds due to forced airflow through the glottis. This forced vibration induces a wavy motion on the folds surface, often called a mucosal wave. Latifi et al. [1] suggested that the use of an injectable viscoelastic material can help to restore the original vocal fold tissue properties after scarring. Other investigations proposed that viscoelastic materials can be used to create functional grafts for the replacement of different organs [3], [4]. Kozin et al. [4] presented a method to produce a 3D printed tympanic membrane (TM) to fully replace the eardrum. The prosthetic replacement of the original TM needs to transmit sound from the surroundings to the ossicular chain of the middle ear. The goal of this study was to measure the viscoelastic properties, including the wave speed and phase velocity, of the prosthetic replacement and to tune the properties to match those of the native human TM. The vocal folds and the TM, are the only organs which are mechanically solicited at high frequency. The vocal folds vibrate over the frequency range between 0.1 to 2 kHz [5], [6] and the eardrum is excited over the range between 0.1 to 30 kHz [3]. A method to quantify the frequency-dependent material properties of the viscoelastic material used is needed to perfectly restore the behavior and the function of the replaced organs.

1.2 Literature review

Lagakos et al. [7] 1986 studied the frequency and temperature dependence of the elastic moduli for numerous viscoelastic materials. The conclusion drawn from their work was that material properties change with decreasing temperature in a way that is proportional to their change with increasing frequency. Based on this assumption, frequency-dependent material characterizations with a vast number of experimental methods have been developed and performed [8], [9], [10]. Conventional methods to quantify viscoelastic biomaterials are most frequently related to parallel plate rheometry [11]. Chan and Titze [12], [13] quantified the viscoelastic material parameters of implantable polytetrafluoroethylene and other phonosurgical biomaterials. Their experiments were performed by a parallel-plate rotational rheometer with frequencies up to 15 Hz. Klemuk et al. [14] used a controlled stress parallel plate rheometer in the frequency range of 0.001 Hz to 100 Hz. Viscoelastic parameters were determined and extrapolated to obtain the viscoelastic properties for frequencies up to 1000 Hz. In 2004 a significant paper was published on high frequency injectable biomaterial testing by Titze et al [14]. Based on an error analysis of the results obtained by rheometry, an accurate prediction of the elastic and shear modulus in the audible frequency range of 20 Hz to 150 Hz was obtained. Jia et al. [15] developed a galvanometer which is based on a slightly modified rheometer. The fundamental idea of their experimental method was to isolate the response of the shear wave components traveling in the material tested at high frequencies. In that way accurate predictions of the material behavior up to a frequency of 500 Hz were made. Based on the reviewed literature, no experimental approach based on parallel plate rheometry is known to determine material properties above 500 Hz.

Pritz [16] developed a mathematical model and experimental method for the characterization of a high frequency-dependent viscoelastic material. A rod-like specimen was produced and excited. The frequency-dependent response was used to quantify the material properties. Based on this work Park et al. [8] characterized numerous materials and obtained their Young's modulus over a wide frequency range. Lai and Rix [17] performed a near-surface site characterization with the help of the simultaneous inversion of Rayleigh phase velocity and attenuation. Their work explained in detail how to predict surface layer propagation and multi-mode excitation. The thesis contained a detailed analysis of known surface wave methods, mathematical analysis, including the Green's function approach and a proposed reformulation of the linear theory of viscoelasticity regarding Rayleigh wave eigenproblems. Moreover, a detailed explanation on how to calculate the effective Rayleigh phase velocity for superimposed modes of propagation was proposed. Finally an algorithm to predict the shear wave velocity profile was implemented and tested. The results calculated from the numerical implementation were in good agreement with the predictions from the theoretical model.

Foti [18] proposed a new testing method for surface characterization based on the experimental transfer function. It included the measurement and investigation of coupling between Rayleigh dispersion and attenuation, a regression process to quantify numerical simulation data, and the determination of the stiffness and the damping of layered viscoelastic materials. The basic idea of the before mentioned surface wave dispersion equation was derived from [19] and [20]. Royston et al. [10] proposed a surface wave propagation method to determine viscoelastic material properties caused by surface excitation at a low audible frequency, below 1 kHz. Two different approaches were proposed. The first one was based on optimizing coefficients through the regression of experimental dispersive Rayleigh phase speed data. The second one focused on optimizing coefficients in a proposed linear viscoelastic model to fit the dynamic frequency response function between the displacement at two known locations. Boeckx et al. [21] proposed a new method to quantify the wave speed of guided acoustic waves in poroelastic or poroviscoelastic plates. The experimental setup was similar to the one of Royston et al. and included an electrodynamic shaker and laser doppler vibrometer (LDV). Different phase velocities for different modes were identified with the help of the relationship between wave number and frequency. Kazemirad et al. [22], [23] proposed a method to quantify the dynamic frequency-dependent material properties of a layered viscoelastic structure based on Rayleigh surface wave phase speed and attenuation. The determination was possible up to a frequency of 4 kHz. The developed method was reported to be accurate and cost effective. One of the limitation of all the reviewed papers was that there were a limited number of experimental methods to cross validate the obtained results.

Moreover, there was no way to compare wave field and phase velocity distributions for the proposed approaches.

Gucunski et al. [24] simulated the behavior of multi-mode Rayleigh wave propagation for layers with different stiffness. It was shown that the dominance of different modes is dependent on the arrangement of the layers with increasing or decreasing stiffness. Bhashyam [25] explained how to choose the correct model to simulate viscoelastic material and do a correct analysis. Adhikari and Chowdhury [26] proposed simulating frequency-dependent damping of viscoelastic material based on the Rayleigh damping approach and explained in detail the underlying mathematics and physics, [27].

1.3 Research objectives

The literature review showed that much numerical and experimental work has been done in the field of viscoelastic material characterization. Numerous experiments and simulations were performed to determine wave attenuation and phase velocities. What is missing from the literature is a detailed analysis of the complex wave propagation and the underlying wave field between the performed experiments. Little work was done on differentiating between different kind of wave types propagating, interfering and maybe invalidating the fundamental assumptions. Moreover, few comparison between numerical and experimentally obtained results were made. The main goal of the present study was to understand the behavior of frequency-dependent viscoelastic materials, and to develop a reproducible characterization method to quantify injectable hydrogel and other viscoelastic materials.

Moreover, a detailed numerical model was needed to distinguish between interfering waves and multi-mode waves.

The first goal was to identify the most accurate experimental method to quantify the material properties. Different methods were compared to cross-validate the obtained results. The method should not be limited to one specific material, but should work for a variety of viscoelastic materials. The bandwidth of the experimental method should be in the frequency range of interest, up to 2 kHz. The developed surface wave quantification method should enable a detailed investigation of the underlying wave field. A frequency-wavenumber spectrum approach was followed [28], [29], [30].

The second aim was to develop a numerical model replicating the experiments performed in the laboratory. The analysis of the numerically obtained results reveals any shortcomings of the assumptions, and help identify experimental errors. A mathematical simulation of Rayleigh wave propagation and multi-mode behavior based on a mathematical model proposed in [31] was thus created.

1.4 Thesis organization

The theoretical model for three different methods to quantify the viscoelastic material properties and an analytical expression to simulated Rayleigh wave propagation is described in Chapter 2. The experimental methods, including sample preparation, detailed apparatus description and method implementation is presented in chapter 3. Chapter 4 presents the numerical implementation of the physical experiment. In Chapter 5, the results of the experimental methods are discussed, analyzed and correlations between them were made. Chapter 6 contains a summary of the work, and of suggested future work.

CHAPTER 2
Theoretical model

2.1 Rayleigh wave propagation in a homogeneous half-space

Compressional and shear waves propagate inside extended viscoelastic or solid materials upon dynamic excitation. When structural waves strike a surface or an interface between two different materials, their energy is scattered. Different wave components are reflected or transmitted. A fraction of the incident wave energy is used to produce a surface wave at the interface, traveling along the boundary between different media. These surface waves are called Rayleigh or Love waves. Love waves are characterized by a horizontally polarized in plane motion, which is hard to detect. Rayleigh waves have a vertically polarized out-of-plane motion, which is easier to observe. There is no difference in the physics of the Rayleigh wave propagation at an interface between two media or at a boundary. The surface of a material constitutes an interface between the medium and it's surrounding environment. Surface waves are attenuated at a certain rate along the direction of propagation. The wave phase velocity and it's amplitude attenuation rate fully characterize wave propagation [32], which can be represented by a complex wavenumber, $\hat{k}$. It is possible to calculate the wave speed and the attenuation rate by measuring the displacement and phase at different locations. The attenuation rate and speed of propagation carry information about the frequency-dependent material properties. The complex shear modulus can be described as $\hat{G} = G' + iG''$, with G' and G'' representing the storage and loss modulus, respectively. Both of these parameters can be obtained from the theoretical models, provided that the type of surface wave is known. In the present work, a method to extract the dynamic shear modulus $\hat{G}$ from the measured Rayleigh wavenumber $\hat{k}_R$ is investigated. The theoretical model for traveling Rayleigh wave in one single layer medium is relatively simple. The limitation is that there should be no reflection from the medium boundaries which create reflected wave components that could interfere with the original propagating wave.

Figure 2–1 illustrates the ideal situation of a surface wave generated on the surface of a soft material by the vibration of a plunger. The plunger creates a sinusoidal displacement along the vertical x_2-direction with a known frequency. This perturbation created one or several compression and shear waves propagating inside the material [33], with the complex speeds represented by $\hat{c}_C$ and $\hat{c}_S$, respectively. These waves are measurable byproducts of the excitation. To obtain a purely traveling wave, the wave must be sufficiently attenuated before reaching the boundary. The surface wave created is confined to the interface and is assumed to exhibit a typical Rayleigh wave behavior. It is assumed that a near-field exists. i.e. the region within one wavelength from the excitation source may not exhibit an ideal propagating wave. The theory of surface wave propagation predicts one single wave propagating for a homogeneous half-space [18].

2.1.1 Mathematical model

The material was assumed to be viscoelastic, isotropic and homogeneous. Therefore, the constitutive equation relating stress, σ_{ij} and strain, ϵ_{ij} is

$$\sigma_{ij} = \hat{\lambda}(\omega)\delta_{ij}\epsilon + 2\hat{\mu}(\omega)\epsilon_{ij}, \tag{2.1}$$

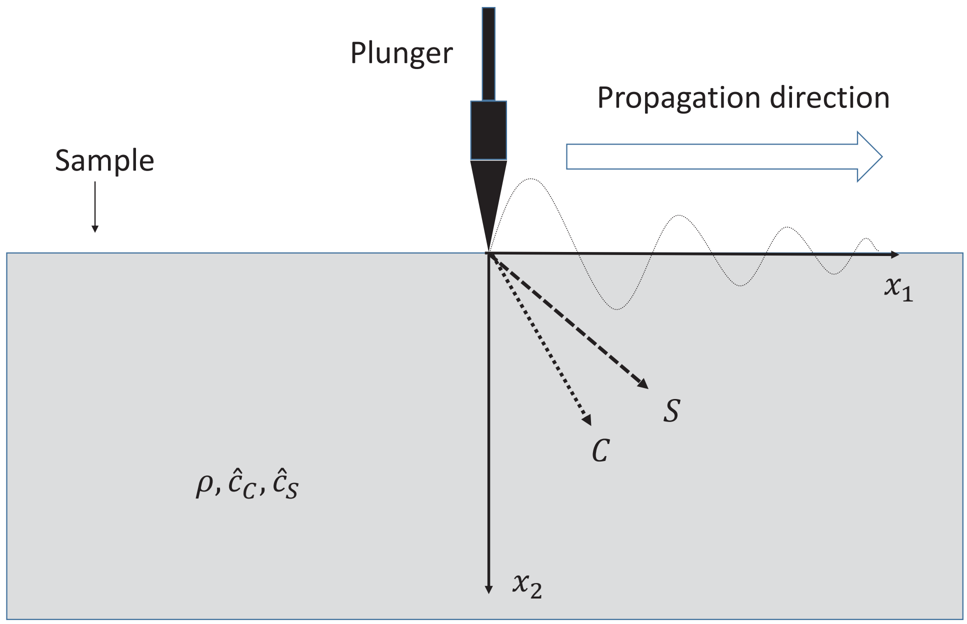

Figure 2–1: Sketch illustrating compressional, shear and Rayleigh wave propagation inside a homogeneous half-space. One Rayleigh wave is propagating on the surface of the material. The wave propagates along the x_1-direction.

where $\hat{\lambda}(\omega)$ and $\hat{\mu}(\omega)$ represent the complex, frequency-dependent Lame functions, δ_{ij} is the Kronecker delta function and ω is the angular frequency. The Lame functions are defined as

$$\hat{\mu}(\omega) = \hat{G}(\omega), \tag{2.2}$$

$$\hat{\lambda}(\omega) = \frac{2\nu}{1 - 2\nu}\hat{G}(\omega), \tag{2.3}$$

where ν is the Poisson's ratio of the material and $\hat{G}(\omega) = G^{'}(\omega) + iG^{''}(\omega)$ represents the complex shear modulus. The displacement of any point within the solid must obey Navier's equation [34]

$$\rho \frac{\partial^2 \bar{u}}{\partial^2 t} = \hat{\mu} \nabla^2 \bar{u} + (\hat{\mu} + \hat{\lambda}) \bar{\nabla} (\bar{\nabla} \cdot \bar{u}), \tag{2.4}$$

where ρ represents the density of the material, and $\bar{u}$ is the displacement vector. According to Helmholtz, the displacement may be expressed as the sum of the gradient of a scalar potential, ϕ and the curl of a vector potential, $\bar{\psi}$, as

$$\bar{u} = \bar{\nabla} \phi + \bar{\nabla} \times \bar{\psi}, \tag{2.5}$$

with the assumption that $\bar{\nabla} \cdot \bar{\psi} = 0$. The vector potential may be caused to be $\bar{\psi} = (0, 0, \psi)$ Substitution of Eq. (2.5), into Eq. (2.4) and equating each term to zero yields a system of two Helmholtz equations

$$(\hat{k}_C^2 + \nabla^2) \hat{\phi} = 0, \tag{2.6}$$

$$(\hat{k}_S^2 + \nabla^2) \hat{\psi} = 0, \tag{2.7}$$

with $\hat{\psi}$ and $\hat{\phi}$ representing the shear and the compressional wave potentials [35]. The complex wavenumber $\hat{k}_c$ and $\hat{k}_s$, can be expressed as

$$\hat{k}_C = \frac{\omega}{\hat{c}_C} = \frac{2\pi f}{\sqrt{(\hat{\lambda} + 2\hat{\mu})/\rho}}, \tag{2.8}$$

$$\hat{k}_S = \frac{\omega}{\hat{c}_S} = \frac{2\pi f}{\sqrt{\hat{\mu}/\rho}}, \tag{2.9}$$

where f is the frequency of excitation, and $\hat{c}_c$ and $\hat{c}_s$ represent the complex compressional and shear wave speed, respectively. The potentials help us to express the directional displacement component in a Cartesian coordinate system

$$\hat{u}_{x_1} = \frac{\partial \hat{\phi}}{\partial x_{x_1}} + \frac{\partial \hat{\psi}}{\partial x_{x_2}}, \tag{2.10}$$

$$\hat{u}_{x_2} = \frac{\partial \hat{\phi}}{\partial x_{x_2}} - \frac{\partial \hat{\psi}}{\partial x_{x_1}}. \tag{2.11}$$

To satisfy the stress free boundary condition at $x_2 = 0$ the wave motion is expressed in x_1-direction in the following form [34]

$$\hat{\phi} = \hat{A}e^{i\hat{k}_R x_1 - \hat{\eta} x_2}, \tag{2.12}$$

$$\hat{\psi} = \hat{B}e^{i\hat{k}_R x_1 - \hat{\beta} x_2}, \tag{2.13}$$

where $\hat{k}_R$ represents the complex Rayleigh wavenumber, $\hat{A}$ and $\hat{B}$ the potentials amplitudes and the time-dependence $\exp(-i\omega t)$ is implicit. It is worth noticing that ψ and ϕ decay exponentially with increasing x_2. This condition is in agreement with the assumption that the Rayleigh wave is confined to the surface of the material. Substitution of Eqs. (2.12) and (2.13) into Eqs. (2.6) and (2.7) yields

$$-\hat{k}_R^2 + \hat{\eta}^2 - \hat{k}_C^2 \longrightarrow \hat{\eta} \quad = \quad \sqrt{\hat{k}_R^2 - \hat{k}_C^2}, \tag{2.14}$$

and

$$-\hat{k}_R^2 + \hat{\beta}^2 - \hat{k}_S^2 \longrightarrow \hat{\beta} \quad = \quad \sqrt{\hat{k}_R^2 - \hat{k}_S^2}. \tag{2.15}$$

The set of boundary conditions which satisfy the stress free interface are $\hat{\sigma}_{12} = \hat{\sigma}_{22} = 0$. Applying this and substituting Eqs. (2.10) and (2.11) into Eq. (2.1) one gets

$$\begin{aligned} \hat{\sigma}_{22} &= -\hat{\mu}\{\hat{k}_S^2\hat{\phi} + 2(\frac{\partial^2\hat{\psi}}{\partial^2 x_2 x_1} + \frac{\partial^2\hat{\phi}}{\partial^2 {x_1}^2})\} \\ &= -\hat{\mu}\{(\hat{k}_S^2 - 2\hat{k}_R^2)\hat{A}e^{i\hat{k_R}x_1 - \hat{\eta}x_2} - 2i\hat{k}_R^2\hat{\beta}\hat{B}e^{i\hat{k}_R^2 x_1 - \hat{\beta}x_2}\}, \end{aligned} \tag{2.16}$$

$$\begin{aligned} \hat{\sigma}_{12} &= \hat{\mu}\{2\frac{\partial^2\hat{\phi}}{\partial^2 x_1 x_2} + \frac{\partial^2\hat{\psi}}{\partial^2 x_2^2} - \frac{\partial^2\hat{\psi}}{\partial^2 x_1^2}\} \\ &= \hat{\mu}\{(-2i\hat{k}_R\hat{\eta})\hat{A}e^{i\hat{k}_R x_1 - \hat{\eta}x_2} + (\hat{k}_R + \hat{\beta})\hat{B}e^{i\hat{k}_R x_1 - \hat{\beta}x_2}\}, \end{aligned} \tag{2.17}$$

with confinement to the surface $x_2 = 0$ one gets

$$\{(2\hat{k}_R^2 - \hat{k}_S^2)\hat{A} + 2i\hat{k}_R\hat{\beta}\hat{B}\}e^{i\hat{k}_R x_1} = 0, \tag{2.18}$$

$$\{-2i\hat{k}_R\hat{\eta}\hat{A} + (2\hat{k}_R^2 - \hat{k}_S^2)\hat{B}\}e^{i\hat{k}_R x_1} = 0. \tag{2.19}$$

The before mentioned equations can be rearranged in matrix format and are satisfied if

$$\begin{bmatrix} (2\hat{k}_R^2 - \hat{k}_S^2) & 2i\hat{k}_R\hat{\beta} \\ -2i\hat{k}_R\hat{\eta} & (2\hat{k}_R^2 - \hat{k}_S^2) \end{bmatrix} \begin{pmatrix} \hat{A} \\ \hat{B} \end{pmatrix} = \begin{Bmatrix} 0 \\ 0 \end{Bmatrix} \tag{2.20}$$

A nontrivial solution of $\hat{A}$ and $\hat{B}$ is obtained when the determinant is equal to zero

$$(2\hat{k}_R^2 - \hat{k}_S^2)^2 - 4\hat{k}_R^2\hat{\beta}\hat{\eta} = 0. \tag{2.21}$$

Eq. (2.21) simplified leads to the following dissipation equation

$$\left(2\frac{w^2}{\hat{c}_R^2} - \frac{w^2}{\hat{c}_S^2}\right)^2 - 4\frac{w^2}{\hat{c}_R^2}\left(\frac{w^2}{\hat{c}_R^2} - \frac{w^2}{\hat{c}_C^2}\right)^{\frac{1}{2}}\left(\frac{w^2}{\hat{c}_R^2} - \frac{w^2}{\hat{c}_S^2}\right)^{\frac{1}{2}} = 0, \tag{2.22}$$

$$\left(2 - \frac{\hat{c}_R^2}{\hat{c}_S^2}\right)^2 - 4\left(1 - \frac{\hat{c}_R^2}{\hat{c}_C^2}\right)^{\frac{1}{2}}\left(1 - \frac{\hat{c}_R^2}{\hat{c}_S^2}\right)^{\frac{1}{2}} = 0, \tag{2.23}$$

$$(2 - \hat{\xi}^2)^2 - 4\sqrt{(1 - \hat{\xi}^2)\left(1 - \frac{\hat{\xi}^2}{\hat{\kappa}^2}\right)} = 0, \tag{2.24}$$

where

$$\kappa^2 = \left(\frac{\hat{c}_C}{\hat{c}_S}\right)^2 = \left(\frac{\hat{k}_S}{\hat{k}_C}\right)^2 = \frac{\hat{\lambda} + 2\hat{\mu}}{\hat{\mu}} = \frac{2 - 2\nu}{1 - 2\nu}, \tag{2.25}$$

and $\hat{\xi} = \frac{\hat{c}_R}{\hat{c}_S} = \frac{\hat{k}_S}{\hat{k}_R}$. From Eqs. (2.14) and (2.15) $\hat{\eta} = \hat{k}_R\sqrt{1 - \frac{\hat{\xi}^2}{\hat{\kappa}^2}}$ and $\hat{\beta} = \hat{k}_R\sqrt{1 - \hat{\xi}^2}$. The Rayleigh wave is thus treated as the superposition of a compressional and a shear wave. Taking a closer look at Eqs. (2.25) and (2.24), it can be observed that the relationship between shear and Rayleigh wave $\hat{\xi}$ is dependent on $\hat{\kappa}$ which can be expressed in terms of the Poisson ratio. It is known that if $\hat{\xi}$ is smaller than unity, and if $\hat{\kappa}$ is greater than unity, then $\hat{\eta}, \hat{\beta}$ are real numbers $\hat{\eta}, \hat{\beta} \in \mathfrak{R}$. Mal and Singh [36] proved that Eq. (2.24) has only one root between 0 and 1. To show that, first the radicals have to be eliminated and Eq. (2.24) rearranged

$$\left(2 - \hat{\xi}^2\right)^4 = 16\left(1 - \hat{\xi}^2\right)\left(1 - \hat{\xi}^2\left(\tfrac{1}{\hat{\kappa}^2}\right)\right), \tag{2.26}$$

$$\hat{\xi}^6 - 8\hat{\xi}^4 + \left(24 - 16\tfrac{1}{\hat{\kappa}^2}\right)\hat{\xi}^2 - 16\left(1 - \tfrac{1}{\hat{\kappa}^2}\right) = 0 = f(\hat{\xi}^2). \tag{2.27}$$

If $\hat{\xi}^2 = 0$ and $\hat{\xi}^2 = 1$ and solve for f

$$f(0) = -16(1 - \tfrac{1}{\hat{\kappa}^2}) < 0, \tag{2.28}$$

$$f(1) = 1 - 8 + 24 - 16 = 1 > 0. \tag{2.29}$$

is obtained. The term $\hat{\xi}^2$ has a maximum of three roots since the equation of $\hat{\xi}^2$ is a third order polynomial. It was shown that $f(\hat{\xi}^2)$ switches its sign between 0 and 1 and therefore it can have either a maximum of all three roots or a minimum of 1 in between. Furthermore, the behavior of f between 0 and 1 can be identified by looking at it's slope f'. The slope is positive between 0 and 1 because $f(0) = 24 - 16\frac{1}{\hat{\kappa}^2} > 0$, $f''(\hat{\xi}^2) = 6\hat{\xi}^2 - 16 < 0$. Therefore, $\hat{\xi}^2$ has only a single root between 0 and 1. From now on, this root is called $\hat{\xi}_R = \frac{\hat{c}_R}{\hat{c}_S}$. This is very important to understand because it proves that there is one unique solution and therefore only <u>one mode of propagation</u> in homogeneous viscoelastic materials. This mode of propagation is confined to the surface of the material, and constitute the canonical Rayleigh wave.

Finally the corresponding surface displacement field can be obtained by substituting Eqs. (2.12), (2.13) into Eqs. (2.10), (2.11)

$$\begin{aligned}
\hat{u}_{x_1}(i\omega, x_1, x_2) &= \Big(i\hat{k}_R\hat{A}e^{-\hat{\eta}x_2} - \hat{\beta}\hat{B}e^{\hat{\beta}x_2}\Big)e^{i\hat{k}_R x_1}, && (2.30)\\
&= i\hat{k}_R\hat{A}\left(e^{-\hat{\eta}x_2} + \left[\frac{\hat{k}_S^2}{2\hat{k}_R^2} - 1\right]e^{-\hat{\beta}x_2}\right)e^{i\hat{k}_R x_1}, && (2.31)\\
&\overset{(x_2=0)}{=} i\hat{k}_R\hat{A}\left(\frac{\hat{k}_S^2}{2\hat{k}_R^2}\right)e^{i\hat{k}_R x_1}, && (2.32)
\end{aligned}$$

$$\hat{u}_{x_2}(i\omega, x_1, x_2) = \Big(- \hat{\eta}\hat{A}e^{-\hat{\eta}x_2} - i\hat{k}_R\hat{B}e^{-\hat{\beta}x_2}\Big)e^{i\hat{k}_R x_1}, \tag{2.33}$$

$$= \hat{\eta}\hat{A}\Big(- e^{-\hat{\eta}x_2} - \frac{i^2\hat{k}_R^2}{2\hat{k}_R - \hat{k}_S}e^{-\hat{\beta}x_2}\Big)e^{i\hat{k}_R x_1}, \tag{2.34}$$

$$\overset{(x_2=0)}{=} \hat{\eta}\hat{A}\Big(- 1 + \frac{\hat{k}_R^2}{2\hat{k}_R - \hat{k}_S}\Big)e^{i\hat{k}_R x_1}. \tag{2.35}$$

In these equations, the time-dependence $e^{i\omega t}$ is implicit. The coefficients of the exponential terms of $\hat{u}_{x_1}$ and $\hat{u}_{x_2}$ are imaginary and real. That indicates that the displacements components are 90° out-of-phase. Moreover, the Rayleigh wave penetrates the material below it's surface as well. The elliptical motion can be shown by calculating the real part of Eqs. (2.32) and (2.35)

$$Real\Big(\hat{u}_{x_1}(i\omega, x_1, x_2)\Big) \overset{(x_1=0)}{=} -\hat{k}_R\hat{A}\left(e^{-\hat{\eta}x_2} + \left[\frac{\hat{k}_S^2}{2\hat{k}_R^2} - 1\right]e^{-\hat{\beta}x_2}\right)sin(i\omega t), \tag{2.36}$$

$$Real(\hat{u}_{x_2}(i\omega, x_1, x_2)) \overset{(x_1=0)}{=} \hat{\eta}\hat{A}\Big(- e^{-\hat{\eta}x_2} + \frac{\hat{k}_R^2}{2\hat{k}_R - \hat{k}_S}e^{-\hat{\beta}x_2}\Big)cos(i\omega t). \tag{2.37}$$

2.1.2 Transfer function method

The transfer function between the oscillatory displacements at two different locations along the wave propagation direction was calculated. The transfer function between the vertical components, u_{x2}, at two different locations along the propagation direction, x_1 , on the interface of the specimen is defined as

$$\hat{H}(i\omega) = \Big|\hat{H}(i\omega)\Big|\, e^{i\varphi} = \frac{\hat{u}_{x_2}(i\omega)|_{x_1=x_{12}}}{\hat{u}_{x_2}(i\omega)|_{x_1=x_{11}}}, \tag{2.38}$$

where $|\hat{H}(i\omega)|$ and φ are the amplitude and phase of the transfer function. Substitution of Eqs. (2.32) and (2.35) into Eq. (2.38) yields

$$\hat{H}(i\omega) = \frac{\hat{u}_{x_2}(i\omega)|_{x_1=x_{12}}}{\hat{u}_{x_2}(i\omega)|_{x_1=x_{11}}}, \tag{2.39}$$

$$= e^{i\hat{k}_R(x_{12}-x_{11})}, \tag{2.40}$$

$$= e^{\gamma L}e^{i\lambda L}, \tag{2.41}$$

$$\left|\hat{H}(i\omega)\right| = e^{\gamma L} \quad , \quad \varphi = \lambda L, \tag{2.42}$$

where $\hat{k}_R = \lambda - i\gamma$ and $L = x_{12} - x_{11}$ is the distance between the two measured points on the surface of the specimen. The complex shear modulus can be expressed in terms of the Rayleigh wavenumber

$$\hat{G} = \frac{\omega^2\rho}{\hat{k}_S^2} = \frac{\omega^2\rho}{\hat{k}_R^2\xi_R^2} = \frac{\hat{c}_R^2\rho}{\xi_R^2}. \tag{2.43}$$

Furthermore, the Young's modulus can be expressed in therms of the shear modulus

$$\hat{E} = 2(1+\nu)\hat{G}, \tag{2.44}$$

and the loss modulus can be expressed as the ratio of loss and the storage modulus

$$\eta = \frac{E''}{E'} = \frac{G''}{G'}. \tag{2.45}$$

2.2 Rayleigh wave propagation in an inhomogeneous, two layered half-space

It was shown that Rayleigh waves are confined to a stress free boundary and they do not propagate inside the material. However, for a multilayer medium an additional Rayleigh wave is trapped at the interface between the two layers and propagates parallel to the Rayleigh wave on the free surface of the medium (Figure 2–2). The Rayleigh waves are created at the interface between different material layers when compressional and a shear waves reach the interface between the two layers. Some energy is reflected or transmitted, and one portion of the energy is transformed into a Rayleigh wave. Since the layers are parallel to each other, the propagation of the interface Rayleigh wave is parallel to the propagation of the surface Rayleigh wave. The energy reflected from the interface of the layers may propagate back to the surface of the material to create another Rayleigh wave. This usually happens when the top layer is very thin and C and S waves don't disperse before reaching the surface again. The interference between different Rayleigh modes changes the motion of local points on the surface [37]. Therefore, the motion is not necessarily anti-clockwise anymore! It is important to notice that, based on this theory, multiple Rayleigh waves, and therefore multiple Rayleigh wave numbers, can be measured on top of the surface. The governing equations are very similar to those for the mono-layer method and are therefore omitted.

The potentials satisfying the before mentioned wave propagation are [34]

$$\hat{\phi}_1 = (a_1 e^{-i\hat{\eta}_1 x_2} + b_1 e^{i\hat{\eta}_1 x_2}) e^{i\hat{k}_R x_1}, \tag{2.46a}$$

$$\hat{\psi}_1 = (c_1 e^{-i\hat{\beta}_1 x_2} + d_1 e^{i\hat{\beta}_1 x_2}) e^{i\hat{k}_R x_1}, \tag{2.46b}$$

$$\hat{\phi}_2 = b_2 e^{-i\hat{\eta}_2 x_2} e^{i\hat{k}_R x_1}, \tag{2.46c}$$

$$\hat{\psi}_2 = d_2 e^{-i\hat{\beta}_2 x_2} e^{i\hat{k}_R x_1}, \tag{2.46d}$$

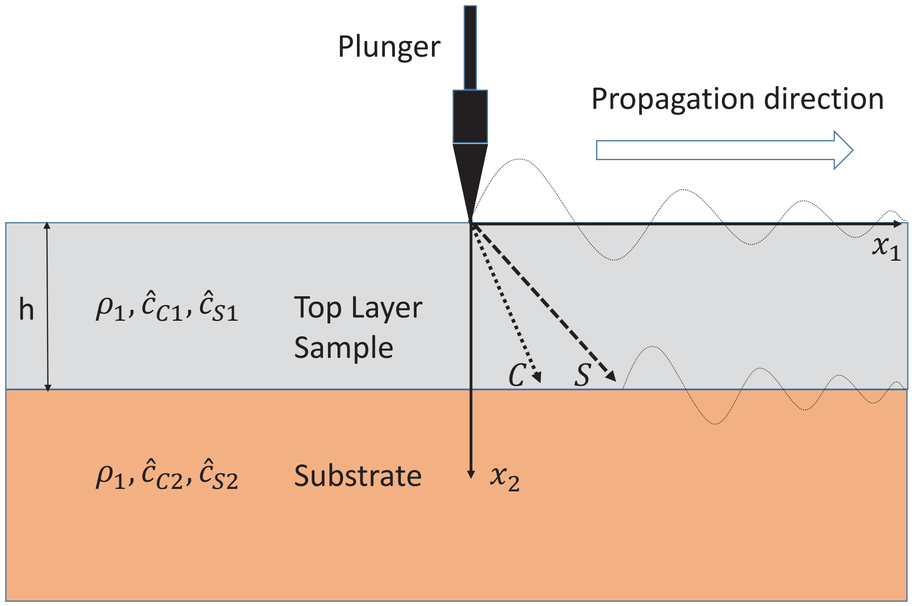

Figure 2–2: Compressional, Shear and Rayleigh wave propagation inside a two-layer system. At least two Rayleigh waves propagate inside the sample. One Rayleigh wave on the surface of the sample and one in the interface between both materials. The wave propagates along the x_1-direction.

where a_1, b_1, c_1, d_1, b_2 and d_2 are the unknown coefficients and represent the amplitudes of the potentials of incident and reflected waves. Taking into account the relationship between compressional and shear wave

$$\kappa_i^2 = \left(\frac{\hat{c}_{Ci}}{\hat{c}_{Si}}\right)^2 = \left(\frac{\hat{k}_{Si}}{\hat{k}_{Ci}}\right)^2 = \frac{\hat{\lambda}_i + 2\hat{\mu}_i}{\hat{\mu}_i} = \frac{2 - 2\nu_i}{1 - 2\nu_i}, i = 1, 2, \tag{2.47}$$

and substitution of the potentials into the governing wave equations, we get

$$\hat{\eta}_1 = \sqrt{\hat{k}_{C_1}^2 - \hat{k}_R^2}, \qquad \hat{\beta}_1 = \sqrt{\hat{k}_{S_1}^2 - \hat{k}_R^2},$$
$$\hat{\eta}_2 = \sqrt{\hat{k}_R^2 - \hat{k}_{C_2}^2}, \qquad \hat{\beta}_2 = \sqrt{\hat{k}_R^2 - \hat{k}_{S_2}^2}.$$

The subscripts 1 and 2 refer to each layer. Substitution of the potential Eq. (2.46) into the stress-free boundary condition at $x_2 = 0$ yields

$$\hat{\sigma}_{22}^1|_{x_2=0} = -\hat{\mu}_1\Big[\hat{k}_{S_1}^2\hat{\phi}_1 + 2\Big(\frac{\partial^2\hat{\psi}_1}{\partial^2 x_2 x_1} + \frac{\partial^2\hat{\phi}_1}{\partial^2 x_1^2}\Big)\Big]_{x_2=0}, \tag{2.48a}$$

$$= -\hat{\mu}_1\Big[(\hat{k}_{S_1}^2 - 2\hat{k}_R^2)(a_1 + b_1) + 2\hat{k}_R\hat{\beta}_1(c_1 - d_1)\Big]e^{i\hat{k}_R x_1}, \tag{2.48b}$$

and

$$\hat{\sigma}_{12}^1|_{x_2=0} = \hat{\mu}_1\Big[2\frac{\partial^2\hat{\phi}_1}{\partial^2 x_1 x_2} + \frac{\partial^2\hat{\psi}_1}{\partial^2 x_2^2} - \frac{\partial^2\hat{\psi}_1}{\partial^2 x_1^2}\Big], \tag{2.49a}$$

$$= \hat{\mu}_1\Big[(2\hat{k}_R\hat{\eta}_1)(a_1 - b_1) + (\hat{k}_R^2 - \hat{\beta}_1^2)(c_1 - d_1)\Big]e^{i\hat{k}_R x_1}. \tag{2.49b}$$

Moreover, the substitution of the potential Eq. (2.46) into the stress-free boundary condition, at the interface of the layers at $x_2 = h$ yields

$$\hat{\sigma}_{22}^1|_{x_2=h} = \hat{\sigma}_{22}^2|_{x_2=h}, \tag{2.50a}$$

$$\hat{\mu}_1\left[\hat{k}_{S_1}^2\hat{\phi}_1 + 2\Big(\frac{\partial^2\hat{\psi}_1}{\partial^2 x_2 x_1} + \frac{\partial^2\hat{\phi}_1}{\partial^2 x_1^2}\Big)\right] = \hat{\mu}_2\Big[\hat{k}_{S_2}^2\hat{\phi}_2 + 2\Big(\frac{\partial^2\hat{\psi}_2}{\partial^2 x_2 x_1} + \frac{\partial^2\hat{\phi}_2}{\partial^2 x_1^2}\Big)\Big], \tag{2.50b}$$

$$\hat{\mu}_1\Big[\Big(\hat{k}_{S_1}^2 - 2\hat{k}_R^2\Big)\Big(a_1\hat{E}_1^{-1} + b_1\hat{E}_1\Big) + 2\hat{k}_R\hat{\beta}\Big(c_1\hat{B}_1^{-1} - d_1\hat{B}_1\Big)\Big]e^{i\hat{k}_R x_1} = 0, \tag{2.50c}$$

$$\hat{\mu}_2\Big[\Big(\hat{k}_{S_2}^2 - 2\hat{k}_R^2\Big)b_2\hat{E}_2 - 2i\hat{k}_R\hat{\beta}_2 d_2\hat{B}_2\Big]e^{i\hat{k}_R^2 x_1} = 0, \tag{2.50d}$$

and

$$\hat{\sigma}_{12}^{1}|_{x_2=h} = \hat{\sigma}_{12}^{2}|_{x_2=h}, \tag{2.51a}$$

$$\hat{\mu}_1\Big[2\Big(\frac{\partial^2\hat{\phi}_1}{\partial^2 x_2 x_1} + \Big(\frac{\partial^2\hat{\psi}_1}{\partial^2 x_2^2} + \frac{\partial^2\hat{\psi}_1}{\partial^2 x_1^2}\Big)\Big] = \Big[2\Big(\frac{\partial^2\hat{\phi}_2}{\partial^2 x_2 x_1}1 + \Big(\frac{\partial^2\hat{\psi}_2}{\partial^2 x_2^2} + \frac{\partial^2\hat{\psi}_2}{\partial^2 x_1^2}\Big)\Big], \tag{2.51b}$$

$$\hat{\mu}_1\Big[\Big(\hat{2}k_R^2\hat{\eta}_1\Big)\Big(a_1\hat{E}_1^{-1} - b_1\hat{E}_1\Big) + \Big(\hat{k}_R^2 - \hat{\beta}_1^2\Big)\Big(c_1\hat{B}_1^{-1} + d_1\hat{B}_1\Big)\Big]e^{i\hat{k}_R x_1} = 0, \tag{2.51c}$$

$$\hat{\mu}_2\Big[\Big(-2i\hat{k}_R\hat{\eta}_2\Big)b_2\hat{E}_2 + \Big(\hat{k}_R^2 + \hat{\beta}_2^2\Big)d_2\hat{B}_2\Big]e^{i\hat{k}_R x_1} = 0. \tag{2.51d}$$

Substitution of Eq. (2.46) into the displacement boundary conditions along the x_1 and x_2-direction yields

$$\hat{u}_1^1|_{x_2=h} = \hat{u}_1^2|_{x_2=h}, \tag{2.52a}$$

$$\Big[\frac{\partial\hat{\phi}_1}{\partial x_1} + \frac{\partial\hat{\psi}_1}{\partial x_2}\Big]_{x_2=h} = \Big[\frac{\partial\hat{\phi}_2}{\partial x_1} + \frac{\partial\hat{\psi}_2}{\partial x_2}\Big]_{x_2=h}, \tag{2.52b}$$

$$\Big[i\hat{k}_R\Big(a_1\hat{E}_1^{-1} + b_1\hat{E}_1\Big) + i\hat{\beta}_1\Big(-c_1\hat{B}_1^{-1} + d_1\hat{B}_1\Big)\Big] = \Big[i\hat{k}_R b_2\hat{E}_2 - \beta_2 d_2\hat{B}_2\Big], \tag{2.52c}$$

and

$$\hat{u}_2^1|_{x_2=h} = \hat{u}_2^2|_{x_2=h}, \tag{2.53a}$$

$$\Big[\frac{\partial\hat{\phi}_1}{\partial x_2} + \frac{\partial\hat{\psi}_1}{\partial x_1}\Big]_{x_2=h} = \Big[\frac{\partial\hat{\phi}_2}{\partial x_2} + \frac{\partial\hat{\psi}_2}{\partial x_1}\Big]_{x_2=h}, \tag{2.53b}$$

$$\Big[i\hat{\eta}_1\Big(-a_1\hat{E}_1^{-1} + b_1\hat{E}_1\Big) + i\hat{k}_R\Big(-c_1\hat{B}_1^{-1} + d_1\hat{B}_1\Big)\Big] = \Big[-i\hat{\eta}_2 b_2\hat{E}_2 - i\hat{k}_R d_2\hat{B}_2\Big]. \tag{2.53c}$$

Variables $\hat{E}_1$, $\hat{E}_2$, $\hat{B}_1$ and $\hat{B}_2$ are defined as

$$\hat{E}_1 = e^{i\hat{\beta}_1 h}, \tag{2.54}$$

$$\hat{E}_2 = e^{-i\hat{\eta}_2 h}, \tag{2.55}$$

$$\hat{B}_1 = e^{i\hat{\eta}_1 h}, \tag{2.56}$$

$$\hat{B}_2 = e^{-i\hat{\beta}_2 h}. \tag{2.57}$$

The before mentioned boundary conditions can be rearranged in matrix format and are satisfied if

$$\bar{\bar{A}}_c \begin{pmatrix} a_1 \\ b_1 \\ c_1 \\ d_1 \\ b_2 \\ d_2 \end{pmatrix} = \begin{Bmatrix} 0 \\ 0 \\ 0 \\ 0 \\ 0 \\ 0 \end{Bmatrix} \tag{2.58}$$

where the matrix $\bar{\bar{A}}_c$ is defined as

$$[A] = \begin{bmatrix} \tau & \tau & -2\hat{k}_R\hat{\beta}_1 & 2\hat{k}_R\hat{\beta}_1 & 0 & 0 \\ 2\hat{k}_R\hat{\eta}_1 & -2\hat{k}_R\hat{\eta}_1 & \tau & \tau & 0 & 0 \\ \tau\mu_1\hat{E}_1^{-1} & \tau\mu_1\hat{E}_1 & -2\hat{k}_R\hat{\beta}_1\hat{B}_1^{-1} & 2\hat{k}_R\hat{\beta}_1\hat{B}_1 & -\chi\mu_2\hat{B}_2 & -2i\hat{k}_R\hat{\beta}_2\mu_2\hat{B}_2 \\ 2\hat{k}_R\hat{\eta}_1\mu_1\hat{E}_1^{-1} & -2\hat{k}_R\hat{\eta}_1\mu_1\hat{E}_1 & \tau\mu_1\hat{B}_1^{-1} & \tau\mu_1\hat{B}_1 & 2i\hat{k}_R\hat{\eta}_2\mu_2\hat{E}_2 & -\chi\mu_2\hat{B}_2 \\ i\hat{k}_R\hat{E}_1^{-1} & i\hat{k}_R\hat{E}_1 & -i\hat{\beta}_1\hat{B}_1^{-1} & i\hat{\beta}_1\hat{B}_1 & -i\hat{k}_R\hat{E}_2 & \hat{\beta}_2\hat{B}_2 \\ -i\hat{\eta}_1\hat{E}_1^{-1} & i\hat{\eta}_1\hat{E}_1 & -i\hat{k}_R\hat{B}_1^{-1} & -i\hat{k}_R\hat{B}_1 & \hat{\eta}_2\hat{E}_2 & i\hat{k}_R\hat{B}_2 \end{bmatrix}. \tag{2.59}$$

with $\tau = 2\hat{k}_R^2 - \hat{k}_{S1}^2$ and $\chi = 2\hat{k}_R^2 - \hat{k}_{S2}^2$. A nontrivial solution for the coefficients a_1, b_1, c_1, d_1, b_2 and d_2 is obtained when the determinant is equal to zero. This relationship is also called dispersion equation, since it links the different Rayleigh wave numbers to a specific frequency. It is important to understand that in a layered system, the wave propagation is no longer dispersive as in the homogeneous case. In fact the wave propagation is highly dispersive. This means that the propagation speed of Rayleigh waves is dependent on its frequency. Also, as mentioned in the introduction, there are multiple Rayleigh waves (different modes) traveling in the sample. This is in agreement with the dispersion equation, since it yields multiple solutions for different $\hat{k}_R$. The dispersion equation can be rewritten in a coefficient matrix $A_{c_{i,j}} = f_{i,j}(\hat{k}_R, \hat{k}_{S1}, \hat{k}_{S2}, \hat{\mu}_2, \nu_1, \nu_2, \rho, \omega, h)$; $i, j = 1, 2, ..., 6$. The only unknowns in this equation before the experiment are $\hat{k}_R$ and $\hat{k}_{S1}$. After measuring the different $\hat{k}_R$ the high order polynomial can be solved for $\hat{k}_{S1}$. Once solved for $\hat{k}_{S1}$ the complex shear and elastic moduli and the loss factor of the top layer can be determined.

2.3 Compressional wave propagation method

2.3.1 Standing wave method

The compressional wave propagation method is a well understood and commonly used technique for the characterization of viscoelastic materials. The fundamental idea is to create a longitudinal wave, propagating inside a rod-like specimen. The wave is usually created by attaching one end of the rod to an electrodynamic shaker, while the displacement of the other end is recorded, Figure 2–3. The data can be used to calculate the Complex shear modulus based on a transfer function method

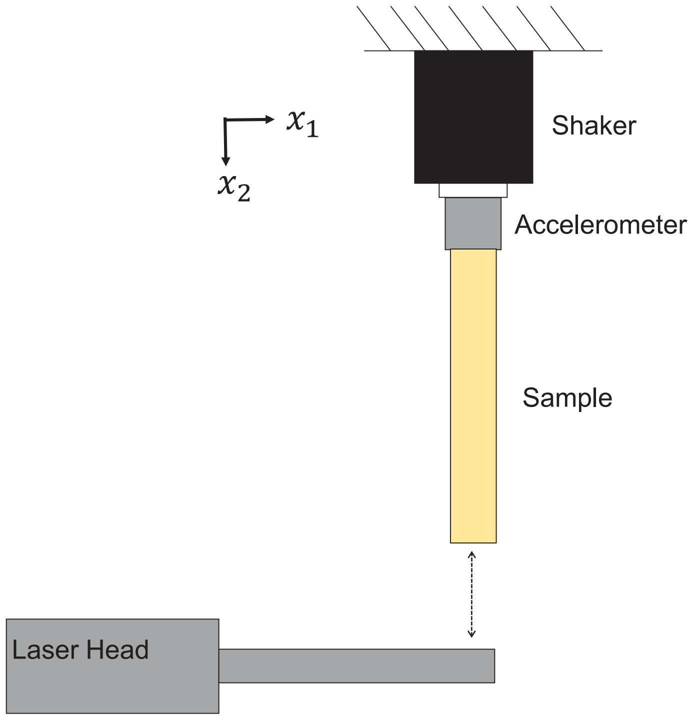

Figure 2–3: Sketch of the standing compressional wave method. An electrodynamic shaker creates a standing wave in a rod-like specimen. The laser measures the displacement of the free end

[16]. The displacement traverse to the propagation direction can be assumed to be homogeneous.

Deriving the transfer function based on the assumption that the rod specimen consists of a homogeneous and isotropic material, constant diameter, which is much smaller than the wavelength of the propagating wave , specific boundary conditions, one can write [16]

$$Re\left[\frac{1}{\hat{H}(i\omega)}\right] = cosh(\alpha l)cos(\beta l) + \frac{M}{m}(\alpha l sinh(\alpha l)cos(\beta l) - \beta l cosh(\alpha l)sin(\beta l)), \tag{2.60a}$$

$$Im\left[\frac{1}{\hat{H}(i\omega)}\right] = sinh(\alpha l)sin(\beta l) + \frac{M}{m}(\alpha l cosh(\alpha l)sin(\beta l) - \beta l sinh(\alpha l)cos(\beta l)), \tag{2.60b}$$

where $\hat{H}(i\omega)$ defines the transfer function between the induced vibration and the measured response of the sample, l is the length of the rod, α and β represent the amplitude decay and phase shift, respectively and $\hat{k}_c = \beta - i\alpha$ describes the wavenumber.

From the frequency-dependent wavenumber one can calculate the complex Young's modulus

$$\hat{k}_c = \frac{\omega}{\hat{c}_c} = \sqrt{\frac{\omega^2\rho}{\hat{E}}}, \tag{2.61}$$

$$\hat{E} = \frac{\omega^2\rho[(\beta^2 - \alpha^2) + 2i\alpha\beta]^2}{(\beta^2 + \alpha^2)}. \tag{2.62}$$

The loss factor can be described as the relationship between absorbed and stored energy

$$\eta = \frac{E''}{E'} = \frac{2\alpha\beta}{\beta^2 - \alpha^2}. \tag{2.63}$$

At this point it is important to understand that the relationship between diameter, d, and wavelength, β, with ($d << \beta$), defines an upper frequency limit, because with an increase in frequency the wavelength decreases. Therefore, to obtain a wide frequency spectrum of properties for one material tested, several experiments, with different diameters, need to be conducted.

2.3.2 Transient wave method

The major difference between the standing and the transient wave methods was that in the later, the wave dissipates before reaching the free end of the sample. Therefore, no standing wave pattern was created.

For this new method the setup was slightly changed. Instead of measuring the displacement of the free end along x_2-direction, it was measured on the side of the rod along the x_1-direction (Figure 2–4). The compression wave, propagating inside the sample, created a transverse expansion due to the Poisson effect. As for the Rayleigh wave approach, the speed of the expansion wave propagating along the rod, can be measured. Once the speed of the compression wave is known the material properties can be calculated [38]. Gordon S. Kino [39] published the relationship between Young's modulus, E, and longitudinal bulk velocity, c_{bc}, as

$$\hat{c}_{bc} = \sqrt{\frac{\hat{E}}{\rho}\frac{1-\nu}{(1+\nu)(1-2\nu)}}, \tag{2.64}$$

where ν represents the Poisson ratio and ρ the density. This equation can be rewritten into

$$\hat{E} = \hat{c}_{bc}^2\frac{(1+\nu)(1-2\nu)}{1-\nu}\rho, \tag{2.65}$$

$$\hat{G} = \hat{c}_{bc}^2 \frac{(1 - 2\nu)}{2(1 - \nu)} \rho. \tag{2.66}$$

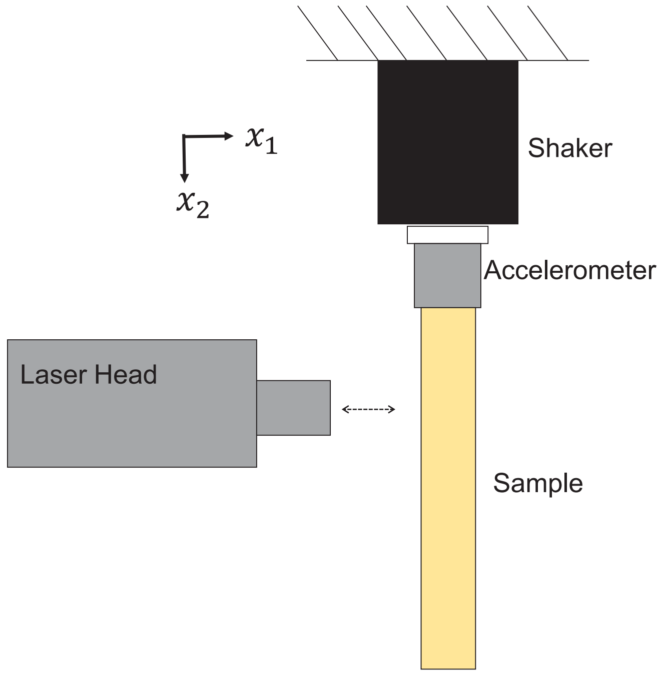

Figure 2–4: Sketch of the transient compressional wave method. An electrodynamic shaker creates a compression wave propagating along the rod. The traveling wave dissipates before reaching the free end. The laser records the displacement on the side of the rod.

2.4 Analytical Rayleigh wave model

Before any experiments and simulations, a simple numerical Rayleigh wave simulation in Matlab was performed. This provided insight into the behavior of Rayleigh waves and it's underlying mechanical behavior. The implementation was based on a volume point source on a surface creating an arbitrary oscillatory wave field in an homogeneous, isotropic elastic half-space [31]. In the following only the basic equations on which the wave propagation was implemented are mentioned. The local motion of any particle along $x_1, x_2 = 0$ in the x_1, x_2 plane is defined as

$$\bar{u}(x_1) = \frac{\pi^2 s \tau u_0^2}{\rho \hat{c}_C^2}\{f_{x_1}(x_1, \hat{k}_R)\bar{e}_{x_1} + f_{x_2}(x_1, \hat{k}_R)\bar{e}_{x_2}\}, \tag{2.67}$$

where

$$f_{x_1}(x_1, \hat{k}_R) = (\hat{\xi}_S + \hat{\tau})\{\mathcal{H}[\hat{k}_R^2 J_1(|\hat{k}_R|x_1) sgn(\hat{k}_R)]\hat{k}_R + i\hat{k}_R^2 J_1(\hat{k}_R x_1) sgn(\hat{k}_R)\}, \tag{2.68a}$$

$$f_{x_2}(x_1, \hat{k}_R) = -i\hat{k}_R^2(1 + \hat{\tau}\hat{\xi}_C)H_0^{(2)}(|\hat{k}_R|x_1), \tag{2.68b}$$

and

$$\hat{\xi}_C = \sqrt{1 - \frac{\hat{c}_R^2}{\hat{c}_C^2}}, \qquad \hat{\xi}_S = \sqrt{1 - \frac{\hat{c}_R^2}{\hat{c}_S^2}},$$

$$\hat{\tau} = -2\frac{\sqrt{1 - \frac{\hat{c}_R^2}{\hat{c}_C^2}}}{2 - \frac{\hat{c}_R^2}{\hat{c}_C^2}}, \qquad \hat{s} = -\frac{\rho \hat{c}_C^2}{i\omega}\mathcal{Q},$$

where $\bar{e}$ stands for the related unit vectors, $\mathcal{Q}$ is the volume velocity of the point source. $H_0^{(2)}$ is the zeroth order Hankel function of the second kind, J_1 is the zeroth order Bessel functions of the first kind and $\mathcal{H}$ is the Hilbert transform. In the derivation process the influence of bulk waves were ignored and therefore the solution is incomplete. But experiments performed by Zabolotskaya et al. [31] showed an increasing accuracy of the solution with increasing distance from the source of excitation. However this approximation should serve as a good platform to start a more detailed surface wave analysis.

CHAPTER 3
Experimental methods

In this chapter, the different methods which were utilized are mentioned and explained. The material preparation procedure, the actual experiments and the experimental challenges are discussed. The performed rheometry and the accuracy of the data is described. Finally, an outline of a detailed simulation model in ANSYS is described.

3.1 Sample preparation

The material response of three major materials was investigated: 1) silicon rubber; 2) chitosan gel; and 3) silicon rubber with embedded nylon fiber fibers.

3.1.1 Single and two layer method

The silicon rubber used (Ecoflex 10 Platinum Cure Silicone Rubber Smooth-On, Inc) was made of three components: 1) part A; 2) part B; and 3) silicon thinner. The mixing ratios were varied and represented in the form of 1:1:1 which meant in this case an equal mass of component A, B and silicon thinner. The amount of each component was varied. For example a mixing ratio of 1:1:0.5 represented in a 250 g sample 100 g of component A, 100 g of component B and 50 g of silicon thinner. The addition of silicon thinner had a direct impact on the dispersive behavior of the wave propagation. The stiffness of the material was decreased. Softer materials tended to be more dispersive.

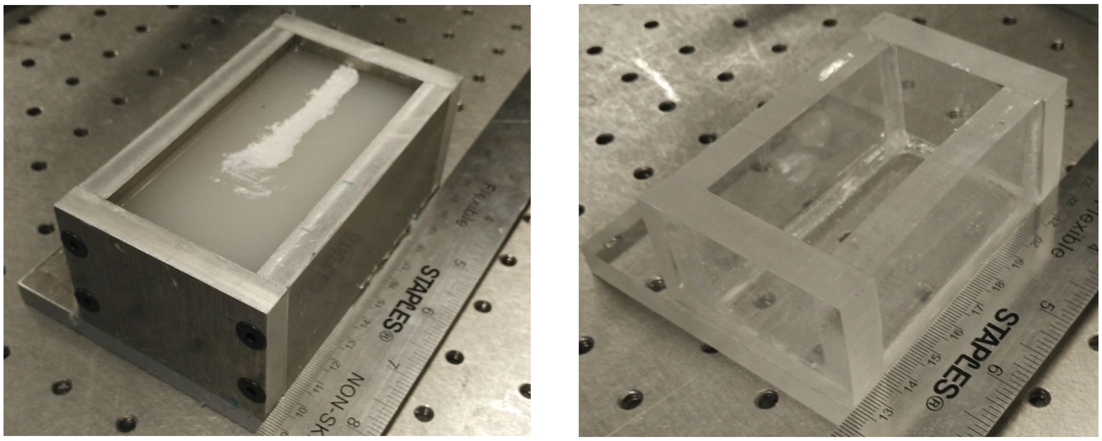

(a) 5 cm x 5 cm x 10 cm steel tray (b) 3.5 cm x 4 cm x 7.5 cm plexiglas tray

Figure 3–1: The different trays served as a mold to cure the material. For the experiment the trays were bolted onto the table to avoid rattling during the excitation.

The silicon rubber samples were inexpensive to manufacture, and served to develop and troubleshoot the wavenumber-frequency method, which is described later. The tray size was 5 cm x 5 cm x 10 cm for silicon rubber Figure 3–1 (a), and a smaller tray of 3.5 cm x 4 cm x 7.5 cm used for the hydrogels, Figure 3–1 (b).

One of the challenges was to produce a bubble free material sample. When the required mixing ratio was reached, the components had to be mixed, which entrained air inside the material. The gel had to be degassed to avoid bubble formation. Degassing a large amount of gel requires air to escape trough the free surface connecting though the body. The speed of this process depends on the amount of gel used and the power of the vacuum pump. For large amounts of gel, the gel may cure before the air is completely removed from the sample. This had to be avoided, since air trapped inside the sample creates an inhomogeneity which influences the wave field. Many different methods have been used in the attempt to prevent the formation of bubbles. The best solution was to vacuum the sample for 30 minutes, and pour it in a way that the distance between the tray and the bucket was large enough (around 1.5 m) to stretch the stream into a small thread. This caused the bubbles to stretch while flowing and to burst. The material was finally cured for 3-6 hours at room temperature. This period doubled when the amount of silicon thinner was doubled.

For hydrogels, Glyoxal and Glycol-Chitosan 40% were acquired from Sigma Aldrich Corporate. The components were mixed in deionized water with a concentration of GCs 5% and Gy 10%. The final solution was placed in a laboratory rotator, and spun at 30 rpm for 24 hours. Efforts were made to keep the chitosan gel hydrated. A humidifier was constantly blowing saturated humid air over the surface. The final concentration of GCs and Gy was 2.5% and 0.005%, respectively. The reason for this specific concentration of cross linker and natural polymer is that it showed no cytotoxicity, and it is therefore a viable candidate for injection [1]. At last, the hydrogel was cured in the tray, as shown in Figure 3–1 (b).

The creation of a two-layer sample was very similar to that of a single layer sample. A material with similar properties to the one which was investigated was used and a sandwich structure created. A substrate with known material properties served as the base of the two layered structure. A very thin layer of the biomaterial of interest was cured on top of the substrate. Both layers were produced following the previously described single layer procedure. The advantage of this procedure is, that only a very small volume of the material to be investigated is needed. This reduces the cost of the experiment.

3.1.2 Fibrous structure

To create a fibrous structure, two flat pieces of cardboard were sutured, such that nylon fibers were stretched between them. The cardboards were glued to the inner walls of the tray, which was prepared for the experiment, Figure 3–2. The tray itself was 7 cm x 7 cm x 12 cm to ensure a reflection free wave field. Once the glue

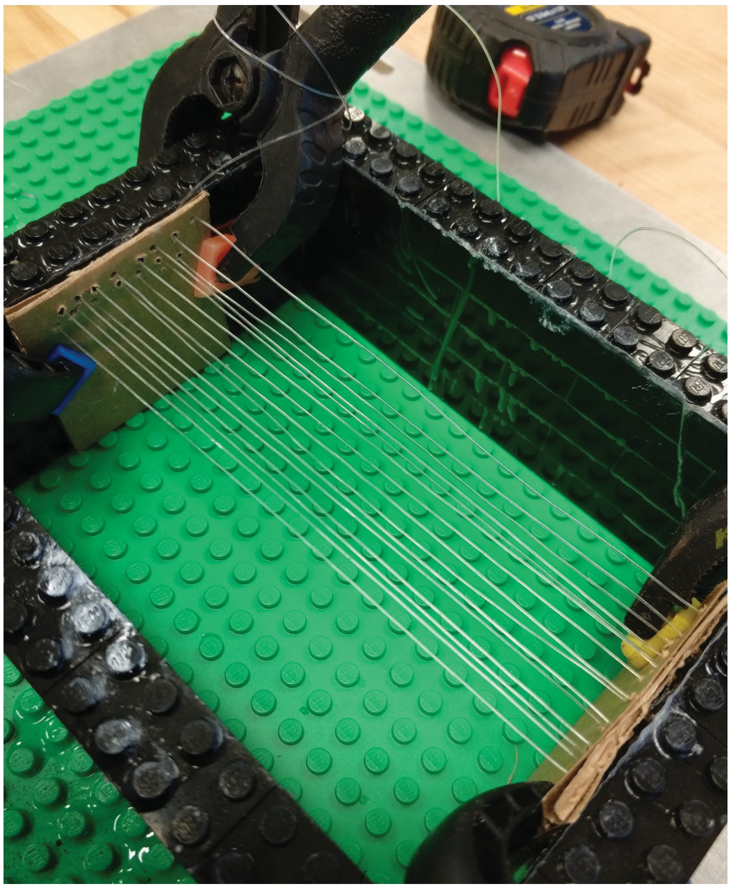

Figure 3–2: Fishing rod was sutured between two cardboard pieces. The pieces were disassembled and glued to the inner walls of the tray.

has dried, the tray was filled with the silicon rubber. The rubber was mixed and degassed, following the previously described procedures. The fibers were embedded near the surface, to ensure an interaction between Rayleigh wave and nylon fiber. Figure 3–3 shows the cardboard embedded inside the gel. The cardboard had no effect on the wave propagation, since the tray was large enough that the wave field dispersed before it could reach the boundaries. The nylon fibers spacing was 5 mm.

Figure 3–3: The tray containing the silicon rubber.

The fibers were laid only in the center of the tray, since the Rayleigh wave was assumed to propagate linearly along this path. There were only two rows of fibers since the penetration depth of the Rayleigh wave is usually no more than one or two wavelength, which are at high frequency a few millimeters. The material was left to cure for 12 hours, Figure 3–4.

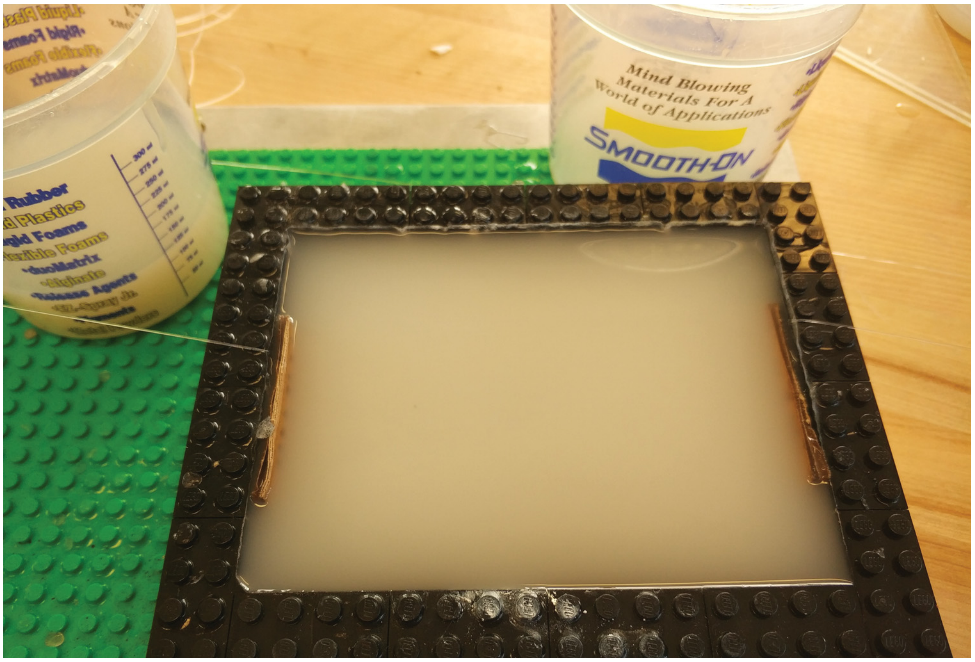

Figure 3–4: Final sample, with nylon fibers embedded, left to cure.

3.1.3 Compressional wave method

For the compressional wave method, cylindrical, homogeneous, bubble free, rod-like specimens had to be manufactured. The material used was the same as for the wave propagation experiment, i.e. Ecoflex silicon rubber. To study the influence of silicon thinner on the material properties and the wave propagation. Different ratios of silicon thinner were examined. Once the components were mixed in the required ratio, the material was put into a vacuum chamber to degas for 20 minutes. Pipettes of 25 mL, 15 mL and 10 mL volume served as mold to obtain cylindrically shaped samples. To pour the material into the pipettes, the silicon rubber was aspirated by connecting the open end to a vacuum pump, to prevent bubble formation. After the material was cured, the sample was cut into the required length, and glued to the accelerometer attached to the electrodynamic shaker. A standard silicon adhesive was used. The measurement can be performed with an attached mass to the free end of the rod. The weight stretched the sample, which influences the wave propagation.

3.2 Rayleigh wave apparatus

Figure 3–5 shows a schematic of the experimental setup. It consisted of four major components: (1) A source of excitation which induced wave propagation inside the material (B&K Mini-shaker Type 4810); (2) The investigated material (Silicon rubber or Chitosan gel); (3) An LDV receiver which measured the displacement generated by the propagating wave (OFV-534 Compact Sensor Head, Vibrometer Controller OFV-5000) (4) An accelerometer which measured the blade displacement (PCD PIEZOTRONICS Model 352C44). The displacement of the shaker was based on a predefined sinusoidal impulse generated in LabVIEW and amplified by a power amplifier (AudioSource AMP100). The displacement of the surface of the sample was measured using the LDV and saved. The procedure was repeated several times for each sample. Once the gel was cured, the tray was bolted into the laser table. The shaker was installed and the blade was positioned near the center of the sample to minimize reflections. The blade was homogeneously driven into the surface to produce a symmetric wave field.

Two different procedures were used to measure the wave propagation speed. The first was based on a 10 s sinusoidal input with a constant frequency. The shaker excited the surface at one single frequency while the accelerometer measured the displacement of the blade and the LDV recorded the out-of-plane motion of a single location on the sample surface. The frequency was varied between 100 Hz and 2000

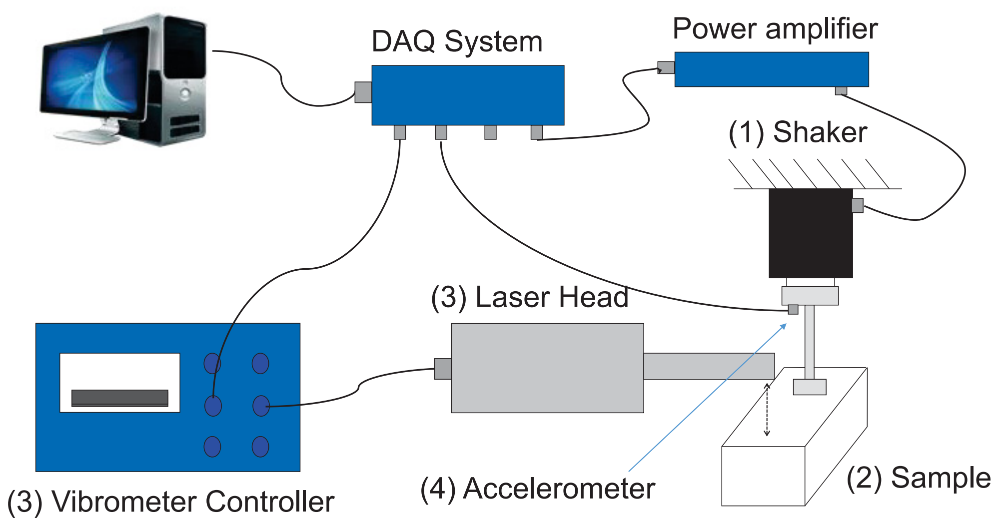

Figure 3–5: Schematic of the experimental setup.

Hz. After 10 s, the shaker stopped for 1 s and the stage drove the laser head to the next position on a predefined path. The shaker excited for another 10 s and the accelerometer and LDV recorded the signals. This procedure was repeated until the entire measurement grid was scanned. Usually the spacing between the points was between 0.5 mm and 1 mm and the pattern contained between 100 (simple line) to 3000 (whole surface) points.

The second method used a frequency sweep generator. The procedure was the same as mentioned before, but the excitation was a 20 s frequency sweep instead of 10 s constant frequency input. The results were the same, but with a different resolution. The frequency sweep covered the whole range of frequencies between 100 Hz and 2000 Hz, but had a lower resolution for the wave speed and the amplitude ratio. The constant frequency input yielded a single frequency result but a high resolution in the wave speed and amplitude attenuation [40]. For each sample, both methods were used. In that way, trends were clearly identified in the wavenumber-frequency spectrum but also the propagation speed and attenuation precisely measured.

3.2.1 2D and 3D visualization along the direction of the laser beam

One limitation of the setup was that one can only measure the out-of-plane motion and therefore the surface response at a single point. To overcome this problem, the local velocity was acquired synchronously with the accelerometer, which served as a phase reference [41]. Based on the cross-spectral density the frequency response of multiple surface points was identified. Figure 3–6 shows a typical measurement grid over the top of the sample. From the cross-spectral density the system response

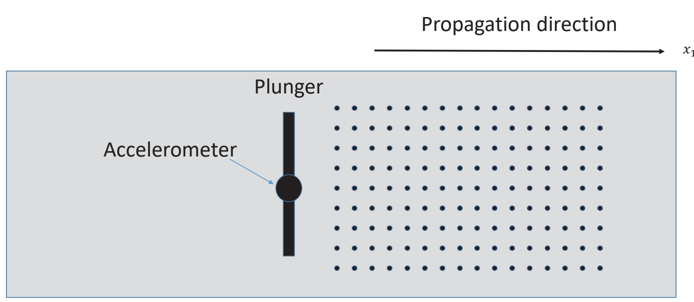

Figure 3–6: Measurement grid on the surface of the sample. The laser scans each point one at the time, using the accelerometer as reference.

for the specific frequency of interest was calculated. Based on this procedure, the maxima were isolated at ever grid point and plotted in Figure 3–7. The envelope function is not exponential. The envelope function in this thesis represents peak amplitudes of the transfer function. There are multiple plausible reasons why this could

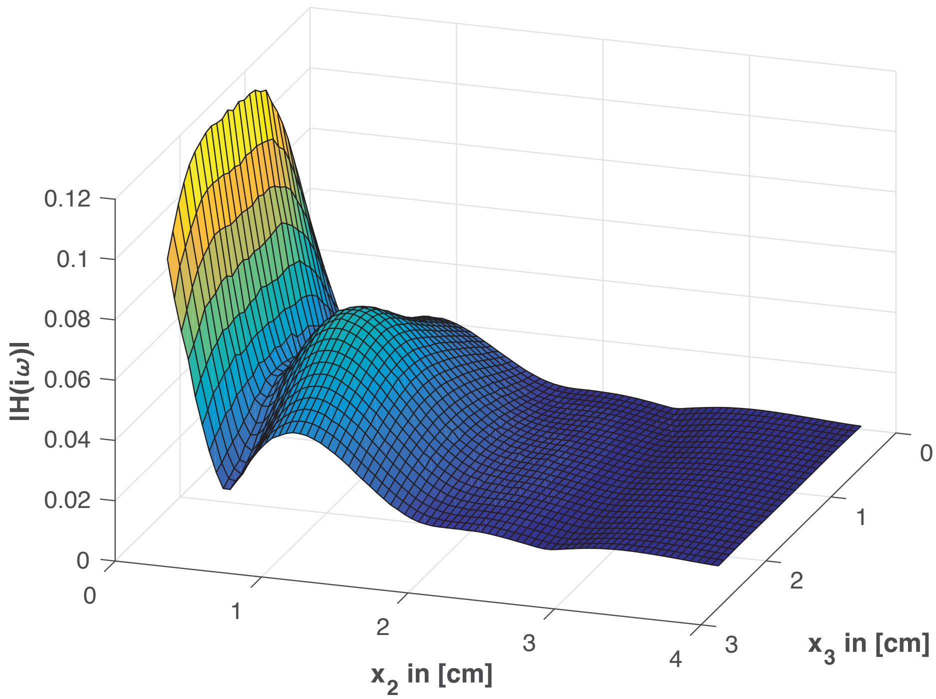

Figure 3–7: Envelope function of a propagating wave at 300 Hz. The amplitude of the transfer function was obtained by using the cross-spectral density.

happen. The first hypothesis was that there are near field effects. Near field effects are phenomena which confine parts of the energy of the propagating wave locally close to the point of excitation. To explain it more visually, the local motion close to the blade consists of a propagating and a stationary component. Both contribute to the surface displacement, but only the propagating component transports energy. This would explain why the envelope function is not exponential close to the point of excitation. Moreover, the cross-spectral density shows only the component at a certain frequency. Therefore, the near field was locally fluctuating at 300 Hz. An argument which contradicts this theory was that past the near field region of one wavelength λ_R the exponential decay didn't recover. This leads to a second possible reason, namely constructive interferences between multiple waves propagating on the surface of the sample. To further tackle this point, additional methods of investigations were used.

3.2.2 Wavenumber-Frequency spectrum

The relative amplitude of Figure 3–7 shows the envelope function of the wave at a frequency of 300 Hz. The cross-spectral density does not provide information about the associated wave type. The pattern in Figure 3–7 may be related to constructive interference between different waves types. Therefore, the spatial Fourier transform was used in an attempt to identify different wave types [42]. First the complete data set was rearranged in a 3-dimensional matrix illustrated in Figure 3–8. The drive point acceleration of the blade and the traverse velocity at each point were measured. This yielded a three-dimensional matrix of mass spectral coefficients in the x_1, x_3 plane. Next, the out-of-plane velocity was differentiated into acceleration and the Fourier transform was calculated. This converted the matrix axis from (x_1, x_3,t) into (x_1, x_3, f)

$$\bar{\bar{A}}(x_1, x_2, f)_{blade} = \int_{-\infty}^{\infty} \bar{\bar{a}}(x_1, x_2, t) e^{-2\pi i t f} dt, \tag{3.1}$$

$$\bar{\bar{A}}(x_1, x_2, f)_{points} = \int_{-\infty}^{\infty} \bar{\bar{a}}(x_1, x_2, t) e^{-2\pi i t f} dt, \tag{3.2}$$

where x_1,x_2 represent the length and with of the sample, respectively and $\bar{\bar{a}}$ the acceleration of each grid point over time. The matrix $\bar{\bar{A}}(x_1, x_2, f)_{points}$ was normalized with respect to the driving point acceleration at each frequency, $\bar{\bar{A}}(x_1, x_2, f)_{blade}$. The

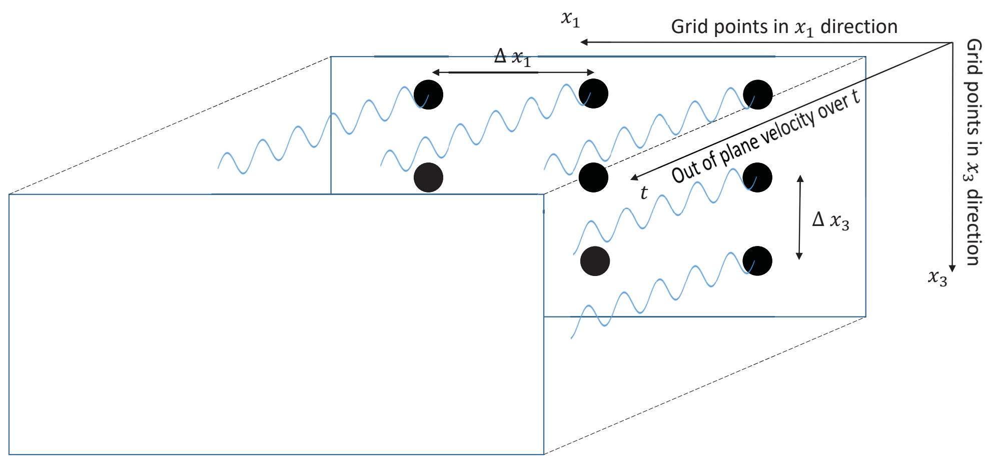

Figure 3–8: The black dots stand for the scanned laser points. The laser measures the velocity along the x_2-direction over time, t. The points are arranged in the x_1, x_2 plane. A temporal Fourier transform was applied along t, and a spatial Fourier transform along the x_1-direction.

x_1 axis was converted with the help of the spatial Fourier transform into wavenumber $\hat{k}_R$

$$\bar{\bar{A}}(\hat{k}_R, x_2, f)_{F-K-Spectrum} = \int_{-\infty}^{\infty} \frac{\bar{\bar{A}}(x_1, x_2, f)_{points}}{\bar{\bar{A}}(x_1, x_2, f)_{blade}} e^{-2\pi i x_1 \hat{k}_R} dx, \tag{3.3}$$

where the plane $(\hat{k}_R, f)$ of $\bar{\bar{A}}_{F-K-Spectrum}$ represents the wavenumber-frequency spectrum. The spatial Fourier transform was applied beyond one wavelength λ_R distance from the source of excitation, to develop the Rayleigh wave characteristics. Each individual line in the wavenumber-frequency spectrum represented one wave propagating on the sample. Multiple lines indicated an interference between surface waves. The sample K-F-plot in Figure 3–9 shows one of these lines. The spectrum is very clear up-to a frequency of 900 Hz. Past that frequency, it was not possible anymore to clearly say in which way the trend develops. One fundamental Rayleigh mode was propagating inside the sample, indicating that a homogeneous material was investigated. Therefore, each frequency had one significant wavenumber value $\hat{k}_R$. From this information it was possible to determine the wave speed, $\hat{c}_R$, corresponding to the Rayleigh mode. This information elucidates the mode of energy propagation in the system.

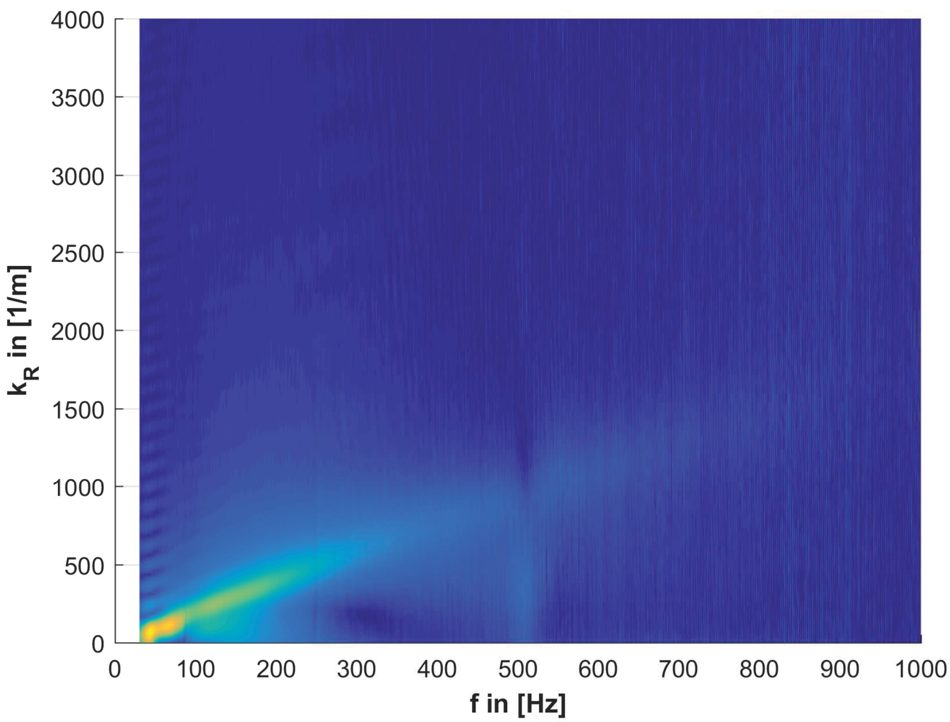

Figure 3–9: Typical Wavenumber-Frequency Plot. The yellow/green line represents the wavenumber, $Real(\hat{k}_R)$, development with increasing frequency. A spurious resonance at 500 Hz contaminated a potion of the data.

Other methods [23] of wave speed determination use measurements of the phase shift at multiple points along a line on the surface. The average phase shift served as an estimate for the speed of propagation. With this approach it was not possible to distinguish between different wave components. Therefore, the phase shift couldn't accurately represent the speed of propagation and was not used to measure the phase speed. The big advantage of the new procedure presented was that all points on the surface were taken into account to evaluate the speed of propagation. Moreover, with the new method, it was possible to distinguish between different modes of propagation. The presented method improved the accuracy of the experiment significantly.

3.2.3 Sources of structure borne noise

For the material tested, it was observed that the lower the frequency of excitation the lower the wave dissipates. This indicated that low frequency waves had a great chance of being reflected from the boundaries. Moreover, there was a lower frequency limit of excitation imposed by the limited bandwidth of the shaker. The lower frequency limit was usually around 100 Hz for most of the samples investigated. This limit varied slightly from material to material. The stiffer the material the higher the frequency limit. The tested hydrogels were much softer than silicon rubber and therefore enabled a high resolution around 100 Hz.

Some artifacts are visible in the data, most likely caused by extraneous vibrations. Examples include the natural frequencies of the receiver, the source or setup holders, the rattling of loose screws or surrounding equipment or a bad setup. The setup had to be repeatedly modified to minimize the sources of interference. The shaker was connected to a shelf separated from the optical table where the LDV was mounted. The only connection between the shaker and the optical table was the blade. Vibration absorbing mounts with the appropriate bandwidth were installed below the laser to minimize laser vibrations. To verify the isolation, a test was performed. The blade was disconnected from the sample and the surface was scanned. The result, shown in Figure 3–10, compared the relative amplitude for an excitation of 100 Hz with and without touching the surface of the sample. The difference is very significant (over 20 dB). The noisy function (b) was without any kind of excitation. The receiver was perfectly isolated from the source of excitation.

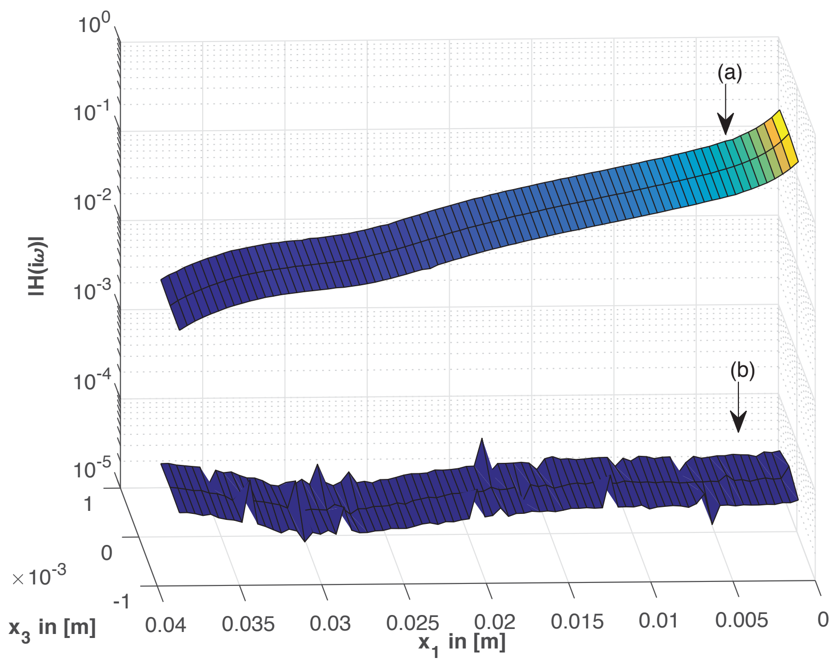

Figure 3–10: Two envelope function of the peak amplitudes. One (a) where the blade was touching the surface of the material and one (b) where it doesn't touch the surface of the sample.

Efforts were made to eliminate the natural frequencies of the setup. The main resonances were related to the shaker holder. The most dominant resonance frequencies were at 300 Hz, 500 Hz and 700 Hz, which were identified because of their smudging effect on the peak in the wavenumber-frequency spectrum. The holder was investigated individually outside of the setup with the same result. Special damping material and additional mass was assumed to solve the problem but the resonance frequencies were impossible to eliminate. The holder was thus excluded from the setup. Instead the shaker was hanged with a rod from the shelf above the table, thereby eliminating essentially all natural frequencies. One natural frequency remained around 500 Hz. Hanging the shaker with the blade not touching the surface, with a sinusoidal input, the acceleration of the plunger was recorded by the accelerometer and the spectrum was calculated. In Figure 3–11 a peak at 500 Hz was detected, disturbing the exponential decay. That means the frequency results at 500 Hz for all the upcoming discussions had to be excluded from the interpretation. It was observed that the accelerometer spectrum was uniform until 500 Hz, but it was noisy beyond 500 Hz. This caused noise for all the results above 500 Hz in the wavenumber-frequency spectra.

3.3 Compressional wave experiment

The compressional wave experiment was described in section 2.3. The thickness of the rod was much smaller than the wavelength to avoid transverse modes. To avoid possible influences of the specimen length, multiple samples, different in length l , diameter d and with or without weight were manufactured and tested. The parameters of the different samples are listed in the following Table 3-1.

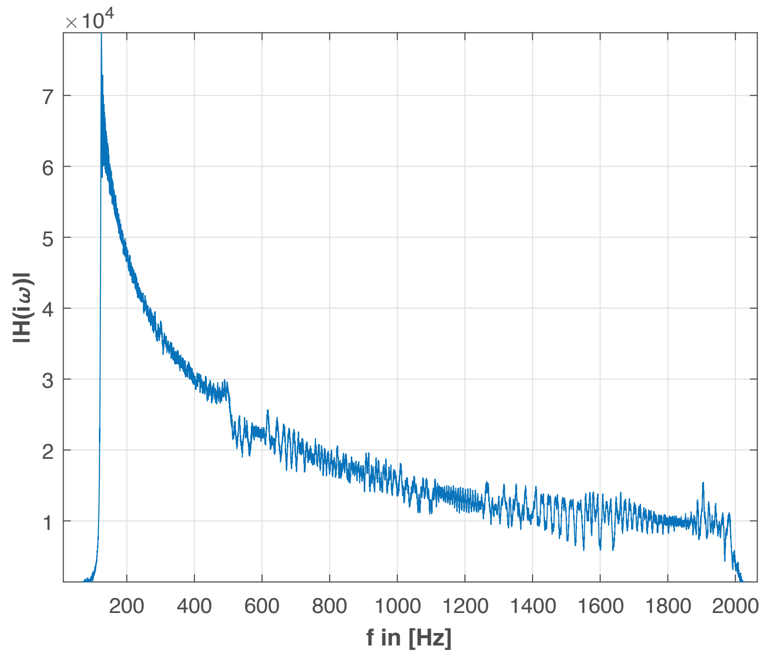

Figure 3–11: Accelerometer Spectrum during a frequency sweep. This plot served to identify natural frequencies.

Experiment	Diameter d in cm	Length l in cm	Mixing ratio	Added mass
Nr.1	0.55	7	1:1:1	No
Nr.2	0.55	7	1:1:0	No
Nr.3	0.55	12	1:1:0	No
Nr.4	1.4	10	1:1:1	No
Nr.5	1.4	12	1:1:1	No
Nr.6	1.4	15	1:1:1	No
Nr.7	1.4	21	1:1:1	No
Nr.8	1.4	27	1:1:1	No
Nr.9	1.4	12	1:1:1	No
Nr.10	0.55	7	1:1:0	Yes

Table 3–1: Different manufactured rod samples

3.4 Torsional rheometry

Rheology was used to obtain an initial guess for the numerical simulations and also as a baseline to compare with the results obtained from the Rayleigh wave method. For all the experiments the Hybrid Rheometer DHR-2 by TA Instruments was used in the stress-controlled mode. The adapter plate was a centered cylinder with a diameter of 2 cm. The material was placed in the narrow gap between the two plates. Depending of which material, a few minutes was needed for curing. The curing procedures for silicon rubber and hydrogels were different. The silicon rubber samples were separately manufactured in the shape of a small disc with a radius of 1 cm and thickness of 1.5 mm. The hydrogels were cured for 25 minutes between the two cylinders. To avoid dehydration, a film of water was poured over the gel. The top plate was rotated and the sinusoidally angular response of the material was recorded. The effect of sliding created jumps in the dynamic shear modulus which were rarely observed, thus no special modification was needed. Each experiment was repeated to validate the acquired data. The material parameters obtained from the experiments were the frequency-dependent dynamic shear modulus, $\hat{G} = G' + G$", and loss modulus, η.

The bandwidth of the rheometer was different than that of the Rayleigh wave method. The frequency range of the rheometry experiment was 0.01 Hz to 100 Hz and the Raleigh wave method 100 Hz to 2000 Hz. Therefore, the Rayleigh wave method complimented the rheometer. However, above a certain frequency, standing shear waves propagated inside the sample and invalidated the rheometry results. This specific frequency was identified when a downturn in the phase angle $tan^{-1}(G''/G')$ occurred (Figure 3–12). This leads to a frequency gap of roughly 70 Hz between Rayleigh wave method and rheometry. Interpolation between the two results looks reasonable, which validated the Rayleigh wave method approach. Interpolation

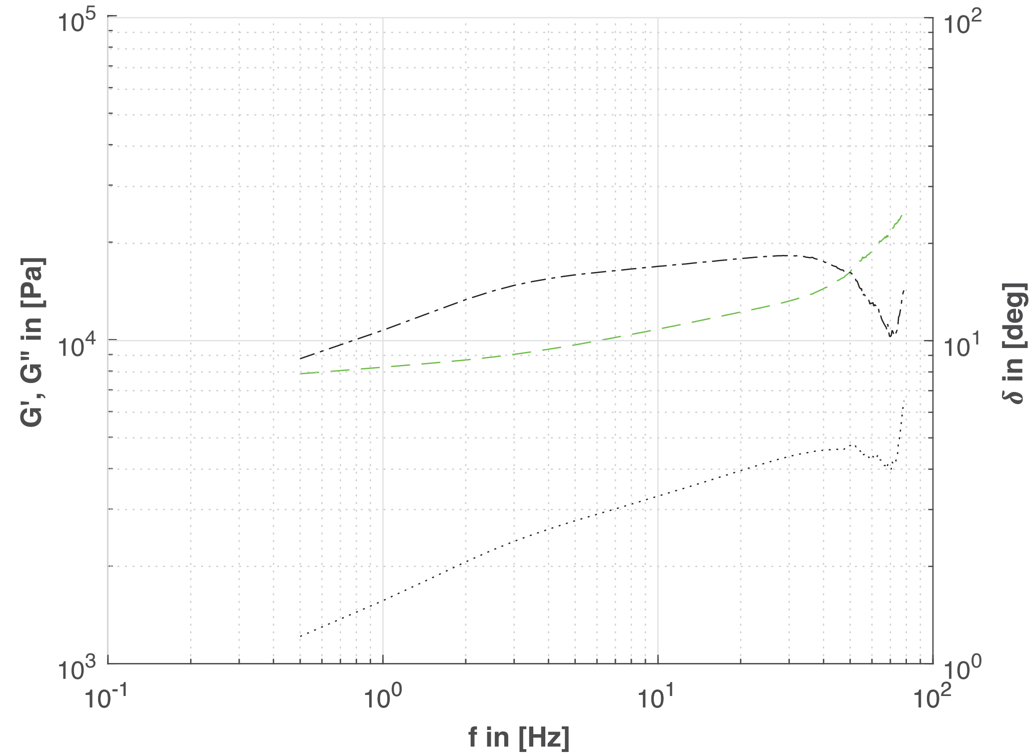

Figure 3–12: Complex shear modulus and phase angle vs. frequency. ·−: Phase angle ; ·: Loss modulus ; −: Storage modulus. Obtained results past 31.5 Hz are invalid due to standing wave propagating inside the sample.

has been used before to predict trends in the determination of viscoelastic material properties [14].

CHAPTER 4
Simulation and virtual experimentation

A computational model of the Rayleigh wave propagation apparatus was created to provide a better physical understanding of the wave field, and to provide a tool for the inverse determination of the material constants.

4.1 Courant-Friedrichs-Lewy condition

The Courant-Friedrichs-Lewy condition, also called CFL number, is a metric for numerical stability. The CFL criterion is as follows

$$C\frac{v\Delta t}{\Delta x} \leq C_{max}, \tag{4.1}$$

where v is the magnitude of the velocity, Δx is the length interval and Δt is the time step. The numerator of the equation describes the distance a cell or the content of a cell can move divided by the dimension of the cell. The equation was to fulfill the condition $C \leq C_{max} = 1$. The interpretation of this equation is that the cell or the content of the cell motion can not exceed the element size, otherwise it can cause numerical errors and instability.

4.2 Transient dynamic analysis

The computational model was implemented in ANSYS version 17.2. It was decided to perform a transient analysis, since the constitutive equation is seeked from the dynamic response of the system under time-dependent perturbations. This made it possible to measure the surface displacement in response to a dynamic input.

However, the underlying equation also took damping effects into consideration which was fundamental in simulating viscoelastic behavior. The equation of motion for the transient structural analysis of a viscously damped system is

$$\bar{F}(t) = \bar{\bar{M}}\ddot{\bar{u}}_n + \bar{\bar{C}}\dot{\bar{u}}_n + \bar{\bar{K}}\bar{u}_n, \tag{4.2}$$

where $\bar{F}(t)$ is the load vector, $\bar{\bar{M}}$ is the mass matrix, $\bar{\bar{C}}$ is the viscous damping matrix, $\bar{\bar{K}}$ stiffness matrix, and $\bar{u}_n$ represents the nodal displacement vector. This equation is solved at any given time step by taking inertia $\bar{\bar{M}}\ddot{\bar{u}}_n$, and damping for as $\bar{\bar{C}}\dot{\bar{u}}_n$ into consideration.

Accurate models for damping were investigated. The specific physical mechanisms of energy dissipation are not fully understood. Moreover, the dominant damping behavior of a structure changes under different dynamic load conditions. In the analytical model, the damping is represented in the equation of motion by the damping term $\bar{\bar{C}}$. Viscous damping is assumed. But ideal viscous behavior is only an approximation of the underlying natural damping mechanism.

A Rayleigh damping model was used for the finite element model [26]. This model was chosen because it was the only material-dependent damping for which a full transient analysis under dynamic cyclic loads is possible. A closer look into the formulation of the underlying theory follows. If Eq. (4.2) is orthogonally transformed, it simplifies into

$$\bar{\psi}^T \bar{F}(t) = \bar{\psi}^T \bar{\bar{M}}\bar{\psi}\ddot{\bar{\xi}} + \bar{\psi}^T \bar{\bar{C}}\bar{\psi}\dot{\bar{\xi}} + \bar{\psi}^T \bar{\bar{K}}\bar{\psi}\bar{\xi}, \tag{4.3}$$

where $\bar{\psi}$ is the normalized eigenvector of the system, and $\bar{\xi}$ is the transformed displacement. The transformation is only valid if

$$\bar{\psi}^T \bar{\bar{C}} \bar{\psi} = \begin{bmatrix} \alpha_d + \beta_d \omega_1^2 & 0 & ... & 0 \\ 0 & \alpha_d + \beta_d \omega_2^2 & ... & 0 \\ ... & ... & ... & ... \\ 0 & ... & ... & \alpha_d + \beta_d \omega_i^2 \end{bmatrix} \tag{4.4}$$

which indicates the damping matrix $[C]$ is a linear combination of mass and stiffness matrices in the form of

$$\bar{\bar{C}} = \alpha_d \bar{\bar{M}} + \beta_d \bar{\bar{K}}, \tag{4.5}$$

where α_d specifies the mass-proportional Rayleigh damping and β_d represents the stiffness-proportional Rayleigh damping. Eq. (4.3) can further be reduced into i-individual equations defined as

$$\bar{F}_i(t) = \ddot{\bar{\xi}} + 2\zeta_i \omega_i \dot{\bar{\xi}} + \omega_i^2 \bar{\xi}, \tag{4.6}$$

where ω_i is the natural circular frequency of the specific mode and the damping ratio, ζ_i, is the representation of actual damping to critical damping for a distinct mode of vibration. For this relationship, a line i of the matrix (4.4) can be equated to damping in Eq. (4.6) and further reduced to

$$\zeta_i = \frac{\alpha_d}{2\omega_i} + \frac{\beta_d \omega_i}{2}. \tag{4.7}$$

The coefficients α_d and β_d can be calculated from the modal damping ratios ζ_i.

Based on Eq. (4.7) the constant α_d represents the damping in the low frequency range. As frequency is decreased, the influence of the α_d-term increases and that of the β_d-term decreases. This is important because upon forced response, some energy cascades over the entire bandwidth of the spectrum, regardless if only one frequency component is excited. The α_d-term was used to filter the energy cascading into the low frequency region. The beta coefficient was the value of interest, since it regulates the high frequency damping.

4.3 Geometry, mesh and boundary condition

The dimension and shape of the computational model replicated those of the experimental apparatus, described in chapter 3. It consisted of a homogeneous material block with dimensions of 5 cm x 5 cm x 12.4 cm. All the boundaries, with the exception of the superior surface, were fixed. Near the center of the superior surface (4.3 cm far from the yx-plane of the model), a nodal displacement was imposed along a 2.2 cm long line, replicating the blade perturbation (Figure 4–1). The Displacement magnitude was calculated based on the recorded accelerometer data from the experiment. The acceleration data was twice integrated and a sinusoidal function fit to the displacement. This fit served as input function for the simulation displacement. For 100 Hz, the displacement was defined as $u_{x_2} = A_f sin((2)(100)t180)$, where A_f was the variable to fit the displacement amplitude to the experimental accelerometer data and t the time step. The nodal displacement was defined along a line which replicated the dimensions of the blade. Each experiment was done for one single frequency to avoid unexpected dynamic transition effects which were observed in experiments. Otherwise, there was no further confinement to the top surface of the material block.

A coarse mesh was used in regions where there was no wave propagation to limit computational loss. The excitation amplitude was selected to create surface waves and avoid body waves propagating and reflecting inside the sample. The damping of the material mesh near the bottom of the domain was high enough to dissipate body waves very quickly. A low damping would allow refections from the lower boundary. In addition, the low mesh resolution at the bottom would significantly increase the error for the results obtained.

On the free surface, a mesh was created with a high resolution at the center of the material, where the important energy transition from element to element occurred. By increasing frequency, the wavelength of the propagating wave decreased. At high frequency only a few mesh points would resolve one wavelength. To avoid numerical errors the spatial resolution of the surface mesh had to be sufficient. Consequently, a mesh density of 10 points per wavelength was used for accuracy. A conversion study on the mesh elements supported this assumption thus ensure a mesh-independent solution.

4.4 Material properties

The overall goal was to mimic the viscoelastic behavior in a computational model to obtain the material properties and to further understand the underlying physics of the experimental observations. As previously mentioned, one of the major reasons why Rayleigh damping was used was its frequency-dependence. The frequency-dependence of viscoelastic materials is known to depend on the nature

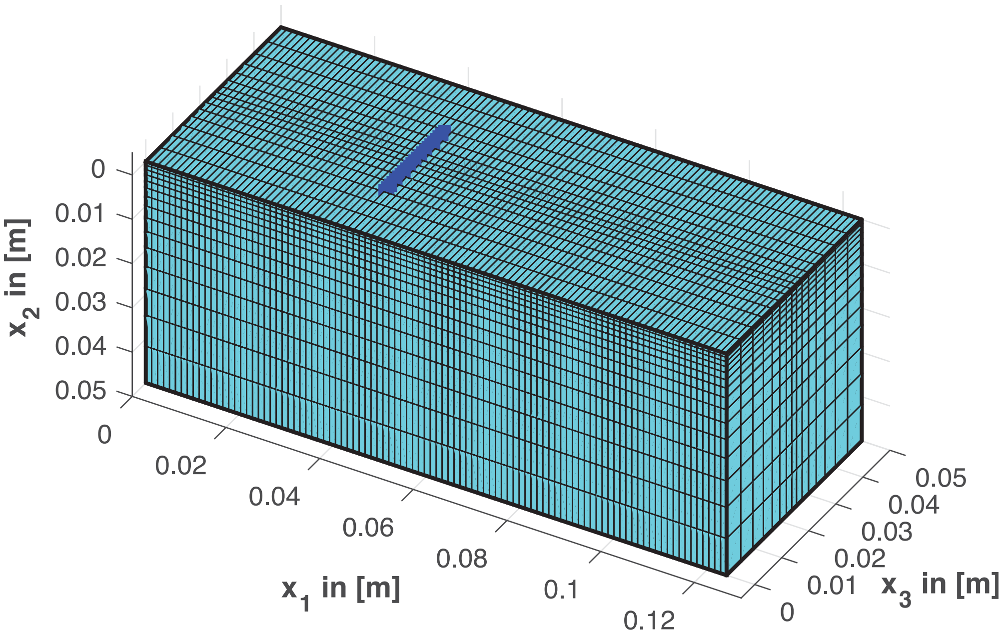

Figure 4–1: Mesh for an excitation of 200 Hz with a predefined line source nodal displacement on the surface of the sample.

of its structural composition. The fibrous structure of viscoelastic materials significantly influences the frequency response of the system. This behavior was simulated by a frequency-dependent damping coefficient, ζ, achieved by the Rayleigh coefficients α_d and β_d, Eq. (4.7).

The simulation was based on a nearly incompressible hyperelastic Neo-Hookean material constitutive law. The hyperelastic model replicated the non-linearly elastic and incompressible rubber-like behavior and is therefore also valid for larger wave amplitudes. This material implementation was tested and showed promising results. Other material models made it difficult to implement frequency dependent damping and were therefore omitted. The Initial shear modulus, G, and stiffness damping, β_d, were the significant parameters manipulated in this simulation. Other material parameters such as the incompressibility, $d_i = 0.00001$, and the density, $\rho = 1086$ of the material were calculated from the laboratory experiments and kept constant [43]. The incompressibility parameter, d_i, must be different from 0 for the Neo-Hookean model to converge. Therefore, d_i was set to the smallest possible value. The material incompressibility parameter is linked to the initial bulk modulus, $K = \frac{2}{d_i}$.

The goal was to find the value of three material constants E, α_d and β_d. Accurate α_d and β_d values may be obtained by fitting Eq. (4.7) to the damping ratio ζ calculated from the rheometry data of the materials. This approach is discussed in detail in the result section. Table 4-1 shows the material properties entered into the

Simulation	α_d	β_d	G
Nr.1	1.948	0.00015	10000
Nr.2	1.948	0.00015	20000
Nr.3	1.948	0.00015	40000
Nr.4	1.948	0.0001	10000
Nr.5	1.948	0.0001	20000
Nr.6	1.948	0.0001	40000
Nr.7	1.948	0.00005	10000
Nr.8	1.948	0.00005	20000
Nr.9	1.948	0.00005	40000

Table 4–1: The different simulations and their related material parameters.

simulation to start a parametric study. The α_d coefficients were unchanged. This was based on the assumption that β_d has a greater effect on the wave propagation at high frequencies (Section 4.2).

CHAPTER 5
Results

5.1 Compression wave results

The goal of this experiment was to generate a standing longitudinal wave propagating in a rod-like specimen to obtain the frequency-dependent Youngs modulus. The specimen dimensions, thickness and length were described in Table 3-1. The material used was silicon rubber with a mixing ratio of 1:1:0 and 1:1:1.

5.1.1 Standing wave method

The first experimental results were obtained by measuring the velocity of the rod specimen tip, while exciting at the other end. The transfer function of the displacement at the two ends of the sample was obtained. Youngs modulus was calculated for different specimen length, and plotted in Figure 5–1.

It was observed that to obtain high quality results for short samples was difficult. When longer samples were produced it increased the quality of the results. This hints that there was a difference in the underlying physics for long or short samples. In experiments explained in section (5.3) it was observed that surface waves, in the same material, dissipated within two to three centimeters (Figure 5–7). Such high dissipation for longitudinal or Rayleigh waves, it is unlikely that the amplitude of the reflected wave would be sufficient to obtain a standing compression wave in the case of 12 cm long samples.

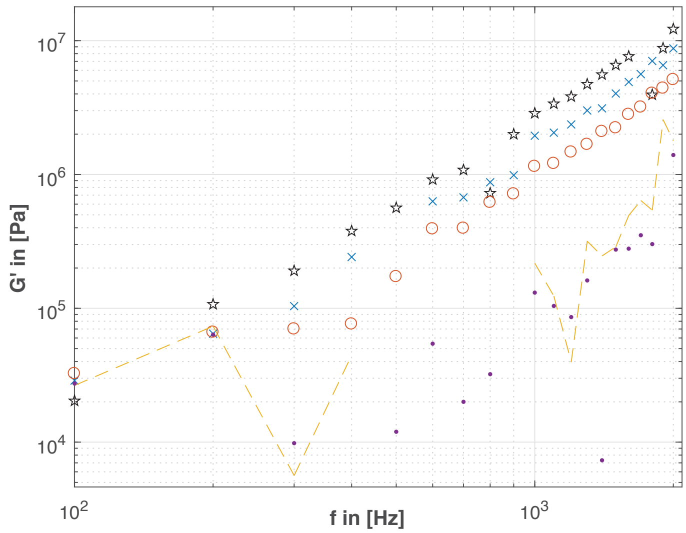

Figure 5–1: Young's modulus vs. frequency. Each line represents a sample with a different rod length. All samples had the same diameter of d = 1.4 cm as well as mixing ratio of 1:1:1. ☆: l = 27 cm ; ×: l = 21 cm ; ∘: l = 15 cm ; —: l = 12 cm ; ·: l = 10 cm.

The complex displacement amplitude and the phase with distance were measured as a function of distance. To avoid transverse waves the diameter, d of the samples had to be much smaller than the wavelength. The results for a diameter of d = 0.55 cm at three different frequencies are shown in Figure 5–2. The plot (a) shows the phase and (b) the amplitude as attenuation of distance traveled. The envelope of the amplitude of the transfer function at 100 Hz in (b) clearly displays a standing wave pattern. Two lobes, at x_1 = 0.003 m and x_1 = 0.046 m, are distinguishable. Moreover, a saddle point in the phase development is identifiable, which is typical for a standing wave. The 500 Hz envelop function has no clear standing wave pattern. A few reflections from the tip of the rod are visible, but they are not strong enough to create a standing wave. This causes the phase development in (a) to be a perfect linearly decaying function. For a greater excitation frequency up to 1000 Hz, no wave propagation was recorded beyond a distance of 0.04 m. The same happened to the phase development. The LDV was barely able to record any signal beyond 0.04 m.

Figure 5–2 shows that no standing wave was present for 1000 Hz or 500 Hz. Moreover, the compression wave dissipated before reaching the end of the sample at 1000 Hz. The response of the sample was not measured when no wave was propagating. The assumption, to calculate the material properties based on a standing wave method for a wide frequency range, was wrong. The experiment was repeated with (Nr.10) and without (Nr.2) weight. No differences between the results were observed. Adding mass to the free end of the rod did not change the propagation behavior.

5.1.2 Traveling wave method

It was found that the standing wave method was not working, at least for frequencies above 100 Hz. To obtain valid result with the experimental apparatus the approach was changed to the traveling wave method. Instead of creating a standing wave propagating in a rod, a traveling wave was created which dissipated before reaching the free end of the rod. The compressional wave speed was measured to calculate the material properties.

In Figure 5–3 the wave speeds (a) and shear moduli (b) are shown vs. frequency for two silicon rubber samples Nr.1 and Nr.2. The development of the wave speed in (a) between both functions was very similar. Up to 700 Hz, the wave speed in silicon rubber with mixing ratio of 1:1:0 and 1:1:1 was in the vicinity of 10 $\frac{m}{s}$ and 6 $\frac{m}{s}$,

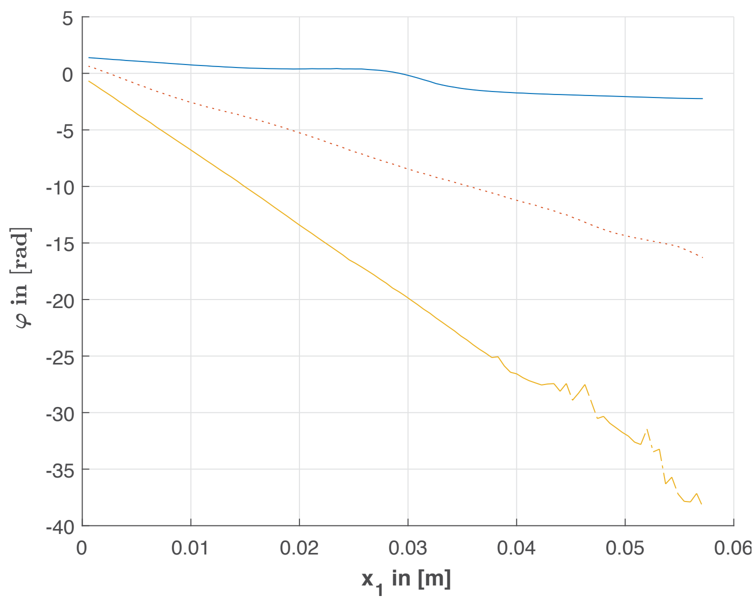

(a)

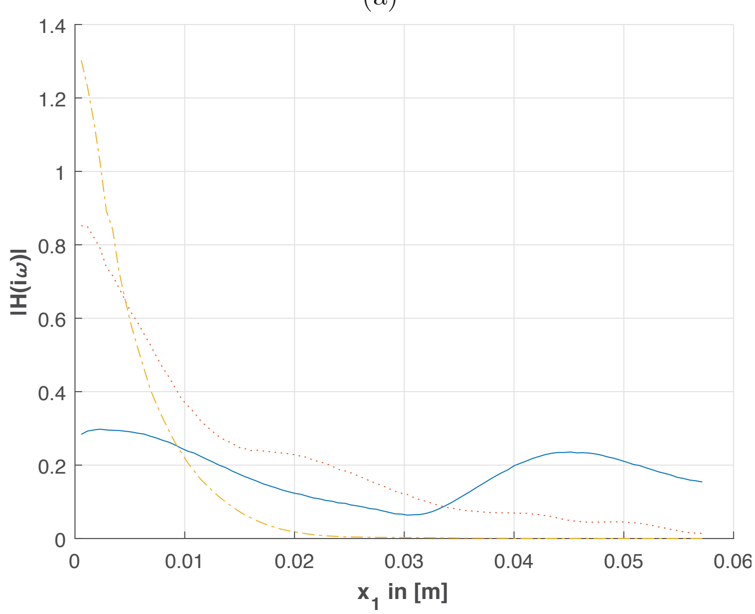

(b)

Figure 5–2: Unwrapped phase (a) and relative amplitude (b) vs. distance propagated. –: 100 Hz ; ·: 500 Hz ; –·: 1000 Hz for sample Nr.5.

respectively. The differences between the propagation speed seemed reasonable, since waves propagate faster in stiffer materials. Beyond 700 Hz, both functions experience a significant change in behavior. It was assumed that at this point the diameter of the sample, d, did not satisfy the necessary condition of $d << \lambda_b k$ anymore. Any value or trend beyond 700 Hz was not valid.

A similar behavior was found in the shear modulus development (b) for both test samples. For silicon rubber with mixing ratio of 1:1:1 and 1:1:0, the values of the shear modulus were around 6x10^3 Pa and 2x10^4 Pa, respectively. Beyond 700 Hz, the data was invalid because the wavelength did not fulfill the required condition $d << \lambda_{bk}$.

5.2 Analytical Rayleigh wave model

Analysis was performed in order to elucidate the characteristics of single Rayleigh waves in comparison to those of multiple Rayleigh wave components propagating along the same direction. The propagation of Rayleigh waves generated by different sources, or the propagation of different Rayleigh modes excited by the same source were investigated. The latter may be encountered when the medium is not perfectly homogeneous, for example if the sample is not homogeneously degassed and gas bubbles are trapped right below the surface of the sample [28]. Inhomogeneous media may cause Rayleigh waves to be scattered into multiple Rayleigh modes which propagate along the same direction [44]. A Matlab script was used to investigate the motion of a single point on the surface, given by Eq. (2.67). For one single Rayleigh wave component propagating in a homogeneous half space, the local motion of a single point on the surface can be described by a anti-clockwise ellipse, as shown in

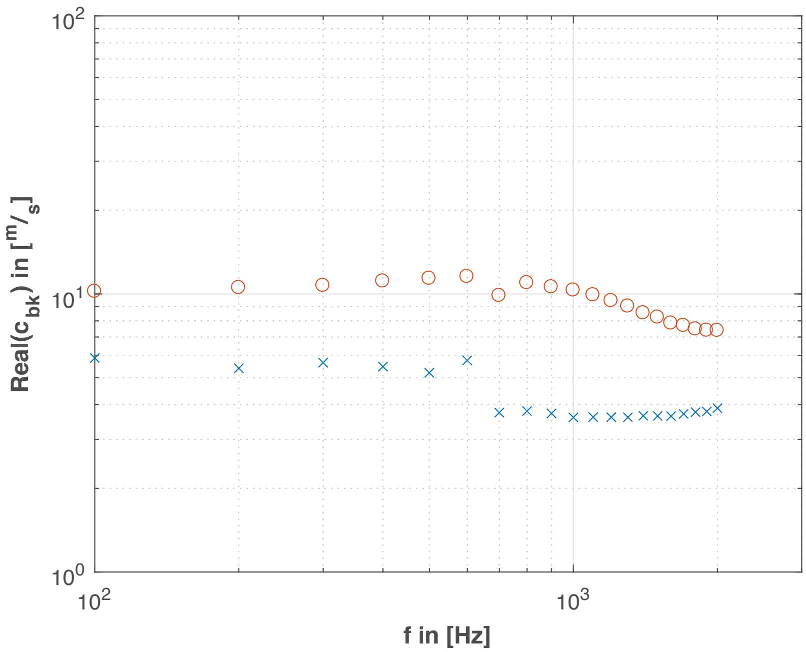

(a)

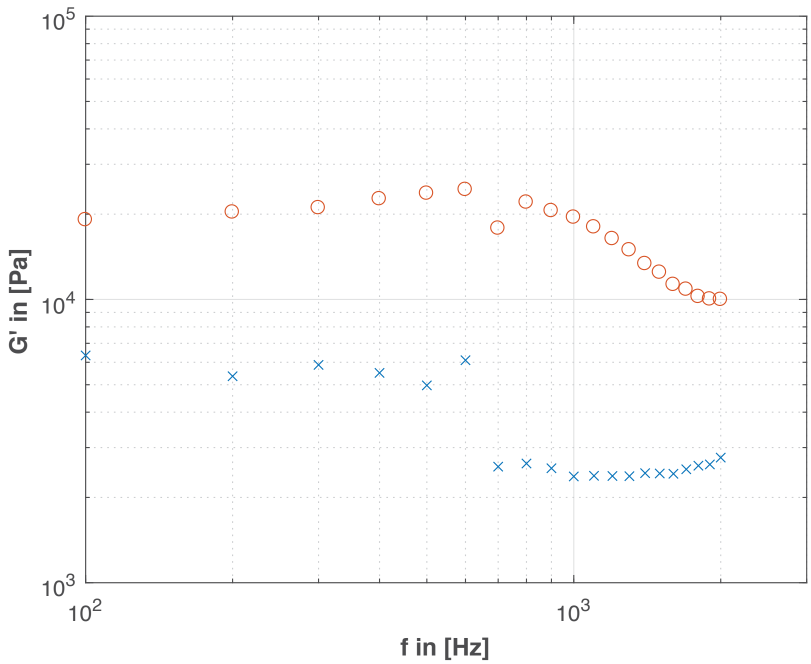

(b)

Figure 5–3: Bulk velocity (a) and shear modulus (b) vs. frequency. ×: Silicon rubber, mixing ratio of 1:1:0 ; ∘: Silicon rubber, mixing ratio of 1:1:1

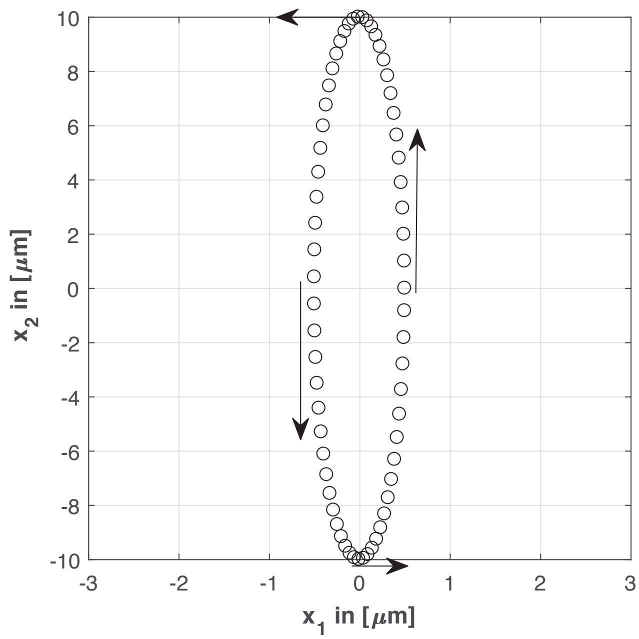

(a)

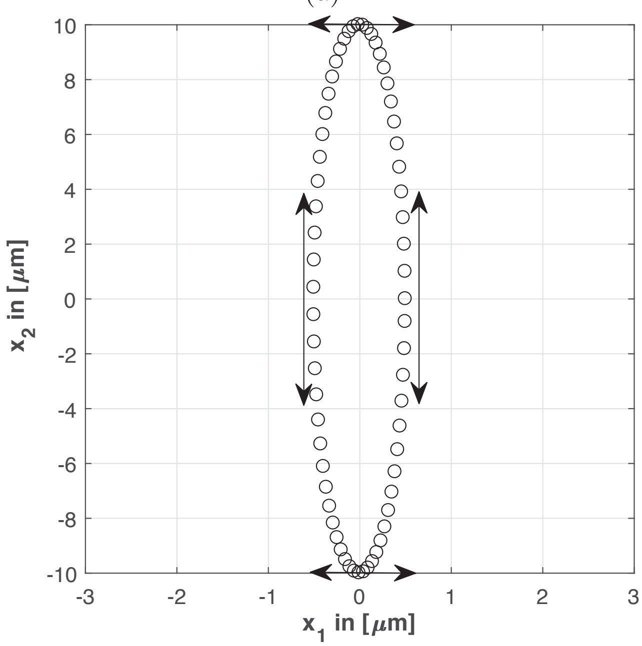

(b)

Figure 5–4: The motion of one local point on the surface for a single Rayleigh wave plot in (a) and for Rayleigh wave interference plot in (b).

Figure 5–4 (a). Wave propagation in an inhomogeneous substrate causes multiple Rayleigh modes with constructive and destructive interferences [45], [46]. This leads to a more complex motion of a local point on the surface of the substrate (b). This may be clockwise or counter clockwise, depending on how many modes are propagating. These differences in particular motion may be used to identify the presence of a scattered field. For example, high speed imaging was used to identify the local motion of a point on the surface. A anti-clockwise motion indicated that the material was homogeneous, with one single Rayleigh mode propagating over the surface of the material.

In Figure 5–5, the envelope functions of the peak displacement amplitudes are drawn. The envelope function in Figure 5–5 (a) is for one single Rayleigh wave, and in (b) for two Rayleigh waves propagating parallel to each other. The envelope function of one single Rayleigh wave in (a) is exponentially decaying, but with interference in (b), it did not decay exponentially. It was possible to fit an exponential function to the amplitude decay in (a) but not in (b). Fitting an exponential function to the amplitude ratio, based on Eq. (2.42), wis of course possible. However, the fit of an exponential function to the interference in (b), yields inaccurate amplitude attenuation rates. Therefore, it must be concluded that obtaining the material properties based on an exponential fit is invalid for a multi-mode system. Previous work, [22], [23], neglected multi-mode propagation and possible interference. The results from these previous studies may not always be very accurate.

Since it is difficult to establish *a priori* if one or several wave components are generated simultaneously at the driving point, a procedure was implemented and

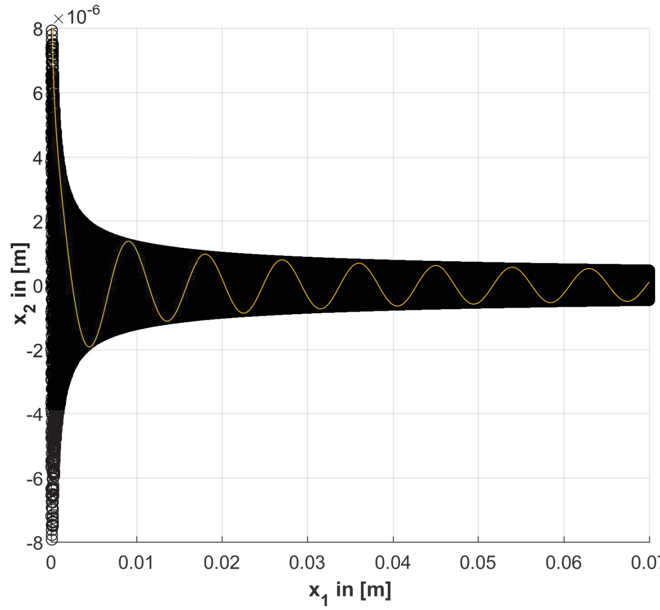

(a)

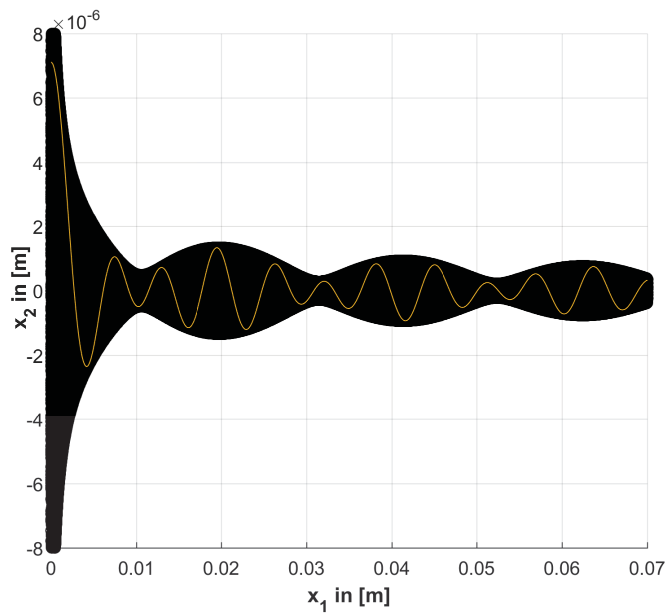

(b)

Figure 5–5: Envelope function of peak amplitudes for (a) one single Rayleigh wave or (b) two Rayleigh waves.

analytically verified for the post processing of the experimental data. The wavenumber spectrum was calculated by using the spatial Fourier transform of the measured amplitudes along the x_1-direction. The real part of the wavenumber of the Rayleigh wave is, $\lambda = Real(\hat{k}_R)$, based on Eq. (2.67). Data analysis should yield the same wavenumber. In Figure 5–6, the spatial Fourier transform of the plots in Figure 5–5 are shown. The exponential decay of the envelope function in Figure 5–5 (a) indicates that one single Rayleigh wave is propagating, which is consistent with the obtained wavenumber spectrum. A clear peak at $\lambda = 700\ \frac{1}{m}$ represents one single wave propagating with a wavelength and wave speed of $\lambda_R = \frac{2pi}{\lambda} = \frac{2pi}{700} = 0.0090$ m and $Real(\hat{c}_R) = \lambda_R f = (0.009)(300) = 2.6928\ \frac{m}{s}$, respectively. The initial wavenumber defined in the code was $\lambda = 700\ \frac{1}{m}$. This verifies the accuracy of this method for the inverse determination of the wavenumber.

The spatial Fourier transform of the peak amplitudes (Figure 5–5 (b)) is shown in Figure 5–6 (b). Two peaks at $\lambda = 1000\ \frac{1}{m}$ and $\lambda = 700\ \frac{1}{m}$ were identified in the wavenumber spectrum. The speed of the second Rayleigh wave was $Real(\hat{c}_R) = \lambda_R f = (0.0063)(300) = 1.8850\ \frac{m}{s}$. The initially defined wavenumbers in the code were $\lambda = 700\ \frac{1}{m}$ and $\lambda = 1000\ \frac{1}{m}$. The procedure allows the accurate determination of both wave speeds.

5.3 Experimental Rayleigh wave propagation

Samples were prepared and experiments were performed following the procedures described in sections (3.1) and (3.2). The first material investigated was a silicon rubber with a mixture of 1:1:0. There were two different plungers used in this setup, a blade of 2.2 cm width, reproducing the effect of a line source excitation and

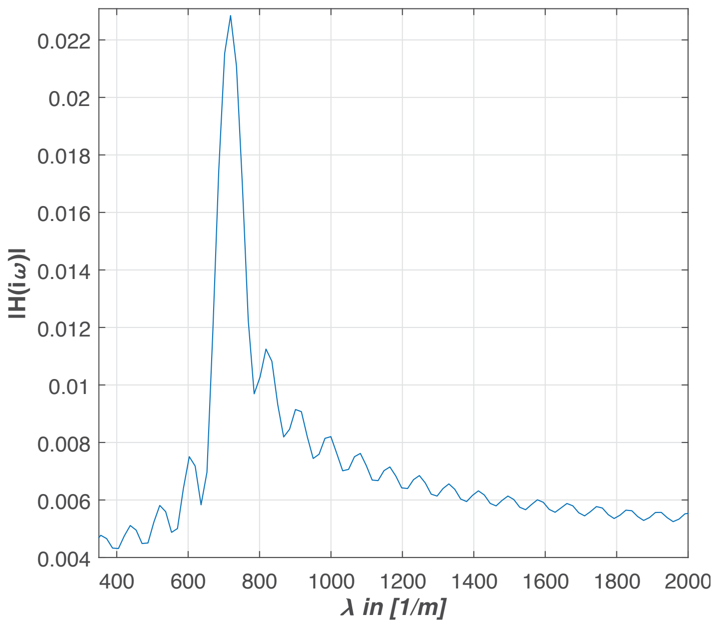

(a)

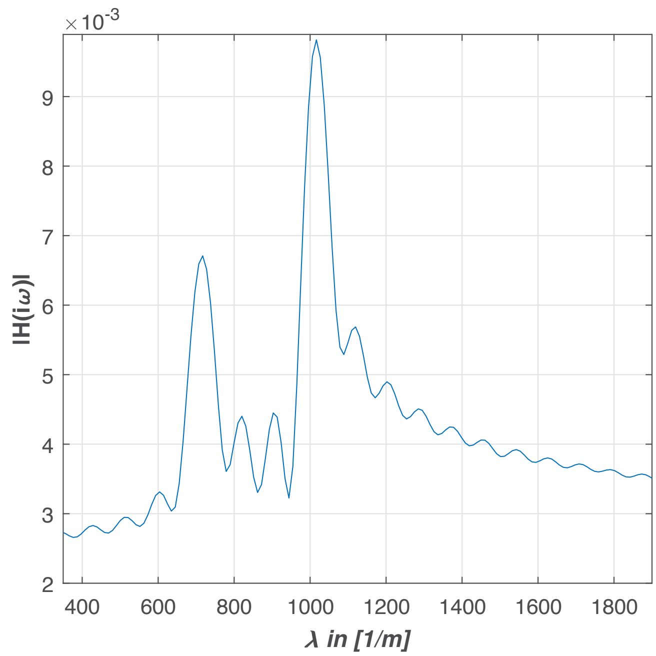

(b)

Figure 5–6: Wavenumber spectrum of (a) one singe Rayleigh wave with a wavenumber of λ = 700, or (b) two Rayleigh waves with wavenumber λ_1 = 700 and λ_2 = 1000.

a circular plunger with a diameter of 1.7 mm, imitating a point source excitation. Figure 5–7 shows the envelope function for the blade and point source excitation for 300 Hz and 900 Hz. The point source excitation created a radial dispersing wave field where the blade excitation created a parallel, more homogeneous wave field. The blade excitation was used since the derivation of the equation was based on parallel propagating wave field and not a radial propagating wave field, which is created by the circular plunger.

At 300 Hz, the wave field died out at around 2 cm to 3 cm. Reflections from the boundaries were negligible since the boundaries were more than 2 cm away from the centerline of the tray. At lower frequency, 200 Hz or 100 Hz, reflections were present and observed. At 900 Hz, the waves propagated in a perfect half circle, with no reflections from the boundaries.

The most significant observation in Figure 5–7 is that none of the amplitude curves exhibit an exponential decay, except maybe the case of Figure 5–7 (c). However, a transition region can be identified. Figure 5–7 (a),(b) and (c) clearly show interference between different waves, or near field effects. To see if the effect was based on constructive interference between waves with different wavelengths, the centerline displacement of plot (c) and (d) was extracted and spatially Fourier transformed. The results are shown in Figure 5–8. The number of points used for the spatial Fourier Transform were 240, consisting of 60 actual displacement values and 180 added zeros to smoothen the spectrum. Zero-padding increased the resolution bandwidth but created side lobes. The spatial Fourier transforms were obtained passed the near field of one wavelength, λ_R, up to the last recorded data point before

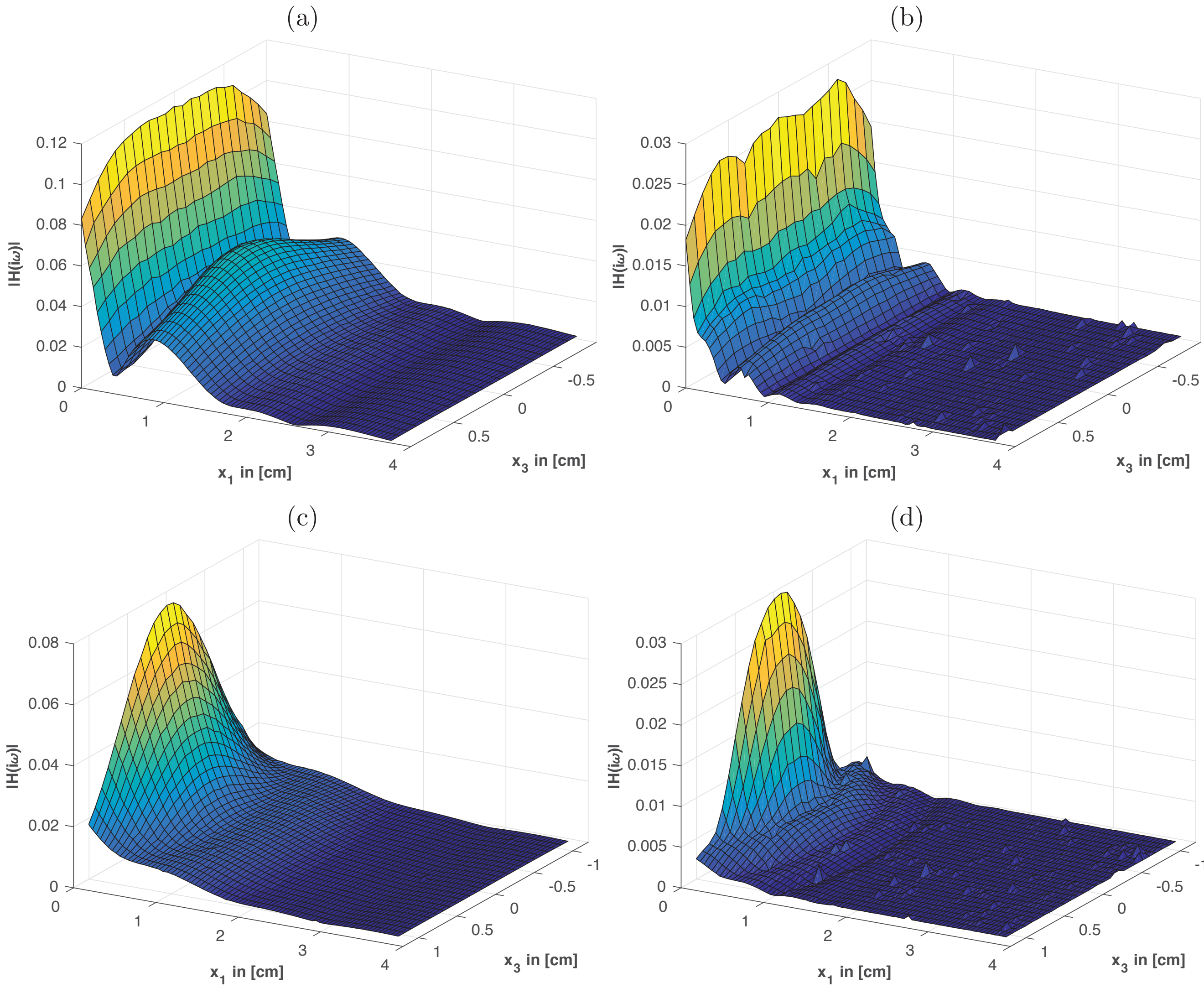

Figure 5–7: The envelope functions of the peak amplitudes for the the wave propagation on the surface of the sample for a (a) 300 Hz line source excitation; (b) 900 Hz line source excitation; (c) 300 Hz point source excitation; and (d) 900 Hz point source excitation.

the wave died out. Therefore, the first point in the time domain displacement field was one wavelength away from the source of excitation.

Each plot has two significant peaks. The first, at $\lambda = 0$, is the DC component and represented a constant value in addition to the sinusoidal displacement in the time spectrum. The value of the second peak were (a) $\lambda = 53$ and (b) $\lambda = 139$. The wavelength and wave speed of the associated waves were (a) $\lambda_R = \frac{1}{53} = 0.0189$ m, $Real(\hat{c}_R) = \frac{\omega}{\lambda} = \lambda_R f = (0.0189)(300) = 5.6700\ \frac{m}{s}$ and (b) $\lambda_R = \frac{1}{139} = 0.0072$ m, $Real(\hat{c}_R) = \frac{\omega}{\lambda} = \lambda_R f = (0.0072)(900) = 6.4800\ \frac{m}{s}$. The material behaved dispersively because the wave speed increases with an increase in frequency. It may be inferred that the wave field in these experiments consisted of either single wave or multiple waves propagating with the same speed along the same direction. The presence of several wave components may be explained as follows. The plunger may have imposed a vertical displacement along with a shear force at the driving point. The necessity of matching the displacement and shear force in the solid at the boundary must require in some cases more than one wave component, as the exact relation between displacement and shear in a single Rayleigh wave may not be representative of the plunger motion. Therefore, the excitation is creating a combination of Rayleigh or other wave components propagating at the same speed, since no other wave types propagating at different speeds were observed. A more detailed investigation of the underlying wave field follows in the computational section.

A second method was used to obtain the wave speed. The approach described in section 2.1.2 measures the phase shift of the propagating wave between two different points with known distance between them. Based on this information, the phase

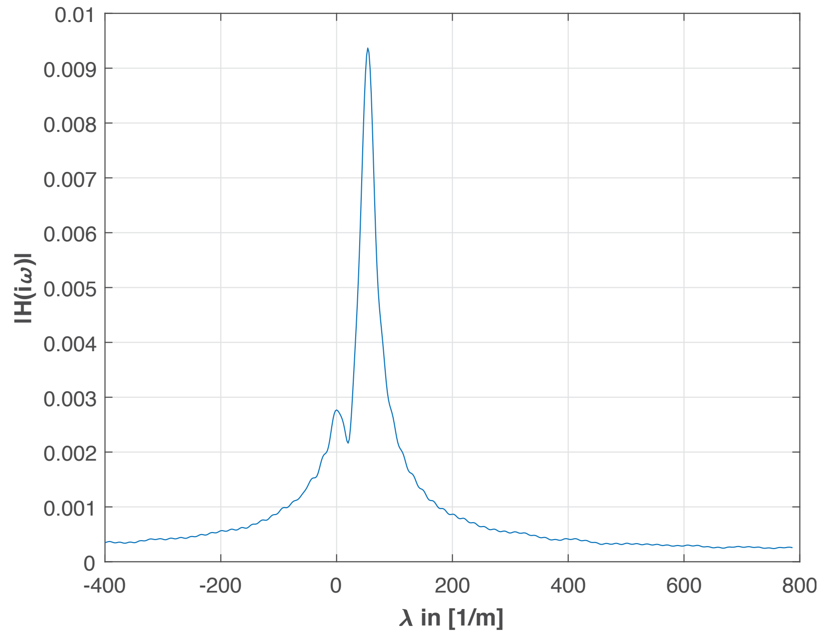

(a)

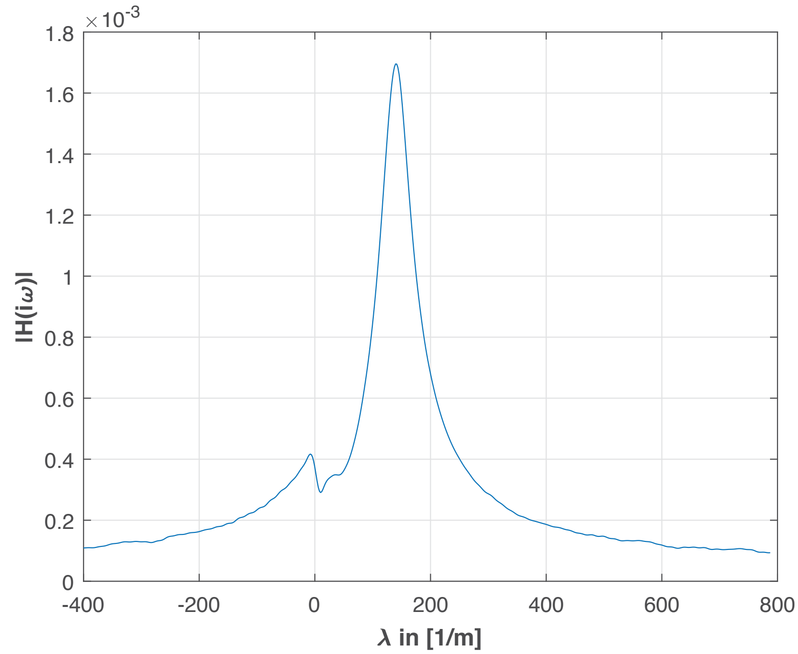

(b)

Figure 5–8: Wavenumber spectra computed from the envelope functions of the peak amplitudes in Figure 5–7. (a) At a frequency of 300 Hz and (b) at a frequency of 900 Hz.

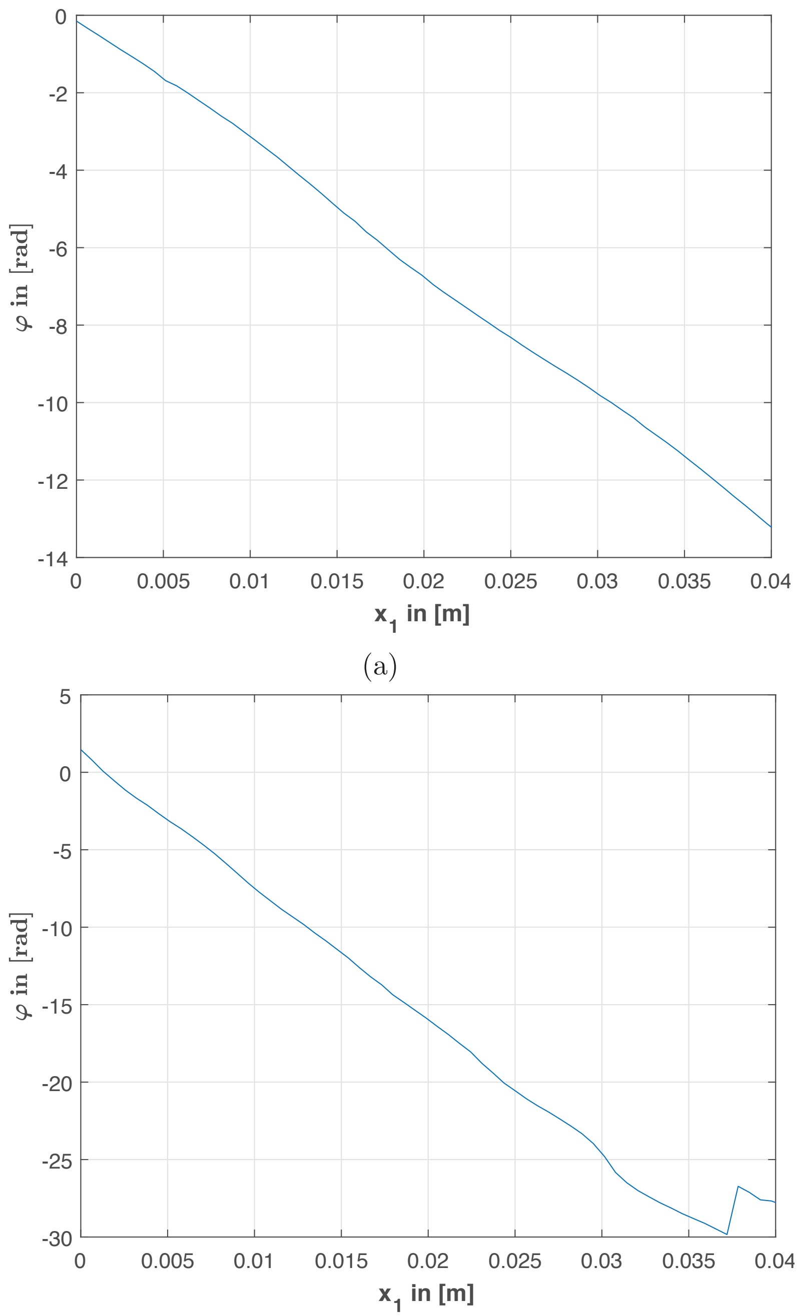

(a)

(b)

Figure 5–9: Unwrapped phase vs. distance traveled for (a) 300 Hz, and (b) 900 Hz excitation.

velocity of the propagating wave was obtained. In Figure 5–9 the radial phase shift along the centerline of Figure 5–7 (c) and (d) was plotted. The phase speed was obtained by either Eq. (2.42) or by taking the equivalent, the slope of the function. The obtained slope from Figure 5–9 (a) was $\frac{\delta\varphi}{\delta x_2} = -334$. This resulted in a wave speed of $Real(\hat{c}_R) = \frac{2pi(300)}{334} = 5.6436\ \frac{m}{s}$. The equivalent value calculated from Figure 5–9 (b) was $Real(\hat{c}_R) = 6.5\ \frac{m}{s}$. The results are in perfect agreement with the spatially Fourier transformed data.

The phase shift method had one big disadvantage. By calculating the phase shift between different points no differentiation between wave types, modes or other propagating energy types can be made [37]. Therefore, the phase shift might be polluted by unrecognized artifacts. The spatial Fourier transform allows discrimination between different propagating energy types, and breaks down propagation into different components [47]. Each of these Fourier components can be identified as an additional line in the wavenumber-Frequency spectrum. This offers a significant advantage because multiple wave components can be identified. The spatial Fourier Transform was subsequently used as it is a more accurate tool.

5.3.1 Rayleigh wave wavenumber-frequency spectrum

The procedure to obtain the wavenumber frequency spectrum and to calculate the material properties was described in section 3.3.2. The shaker generated a sweep function up to 2 kHz and the displacement was measured along the propagation direction, at 100 equally spaced points. The 2D Fourier transform was used to convert the data into the wavenumber-frequency spectrum. The Storage modulus was then obtained.

Figure 5–10 shows the wavenumber-frequency spectrum extracted from the experimental data for all the different materials tested. The different materials tested were characterized by different amplitude curve offsets and slopes.

The silicon rubber with a mixing ratio of 1:1:0 was the stiffest and thus had the lowest wavenumber values. The wavenumber $real(\hat{k}_R)$ linearly increased for all silicon rubber samples with increasing frequency. The silicon rubber with a mixing ratio of 1:1:0.5 was softer and had higher wavenumber values than the silicon rubber with a mixing ratio of 1:1:0. The silicon rubber with a mixing ratio of 1:1:1 was the softest among the silicon rubbers tested. It had the highest wavenumber values. Increasing the amount of silicon thinner increased the offset, with minor changes in slope. This indicated a lower stiffness and a greater viscosity. The hydrogel was more viscous and less stiff than the silicon rubber samples. It had the highest offset. A higher wavenumber indicates a smaller wavelength. The more viscous and less stiff the material, the shorter the wavelength. This affects the cycles per length and therefore the damping. The behavior of the hydrogel follows the trend of the Silicon samples. The increase in wavenumber is linear with increasing frequency. The offset is much higher compared to the silicon rubbers which indicates a much softer material. The differences between the materials tested were more visible in the wave speed plot of Figure 5–11.

The overall wave speed behavior is logarithmic, which is indicated by a linear increase in the wavenumber frequency plot. The wave speed in the hydrogel was the lowest measured. It trends asymptotically towards a value around $Real(\hat{c}_R) = 2\ \frac{m}{s}$. Silicon rubber with mixing ratios of 1:1:1, 1:1:0.5 and 1:1:0 trends towards

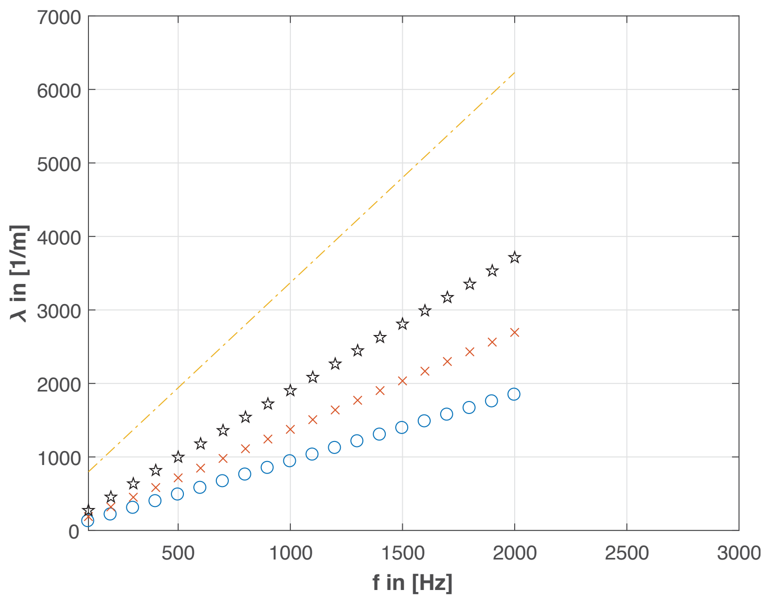

Figure 5–10: Wavenumber-frequency spectrum. ○: Silicon rubber, mixing ratio of 1:1:0 ; ×: Silicon rubber, mixing ratio 1:1:0.5 ; ☆: Silicon rubber, mixing ratio 1:1:1 ; —·: Hydrogel, mixing ratio of GCs 2.5% and Gy 0.005%.

$Real(\hat{c}_R) = 3.4 \ \frac{m}{s}$, $Real(\hat{c}_R) = 5 \ \frac{m}{s}$ and $Real(\hat{c}_R) = 6.8 \ \frac{m}{s}$, respectively. The greater the rigidity of the sample, the faster the wave propagation.

A similar behavior was observed when plotting the shear modulus, shown in Figure 5–12. The relationship between wave speed and the shear modulus is quadratic, therefore the trend was almost maintained. All the samples showed a logarithmic increase and an asymptotic trend towards a constant value at a certain frequency. This was believed to come from the influence of the fibrous structure of the material. At low frequency the fibers have less time to unravel and adhere to each other, which resulted in an increase in stiffness. At a certain frequency the fibrous structure didn't respond anymore. Any further increase in speed did not change the behavior

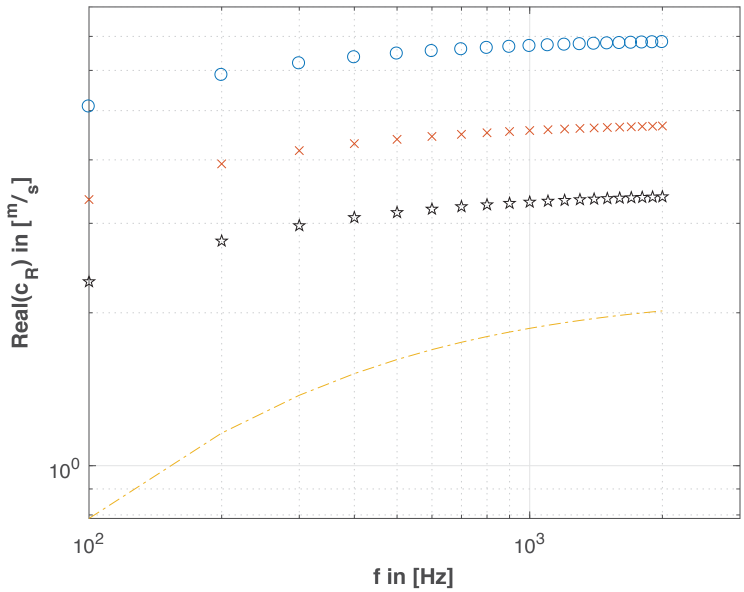

Figure 5–11: Wave speed c_R vs. frequency. ∘: Silicon rubber, mixing ratio of 1:1:0 ; ×: Silicon rubber, mixing ratio 1:1:0.5 ; ☆: Silicon rubber, mixing ratio 1:1:1 ; –·: Hydrogel, mixing ratio of GCs 2.5% and Gy 0.005%.

of the fibers anymore. Among all the materials tested, the wave speed of the hydrogel reaches a constant value at greater frequency. This indicated a difference in the material structure of the hydrogel compared to the Silicon rubbers. Based on the previously mentioned theory, this could result from a less fibrous structure. A less fibrous structure has more space for the polymer chains to unravel. This could lead to a longer logarithmic increase. The opposite was true for the Silicon rubber. The ratio of fibers per matrix is much greater and therefore the whole structure is much more dense. When excited, the fibers have less space to unravel and start to adhere to each other at lower frequency. Therefore, the asymptotically trends towards a constant value showed up later.

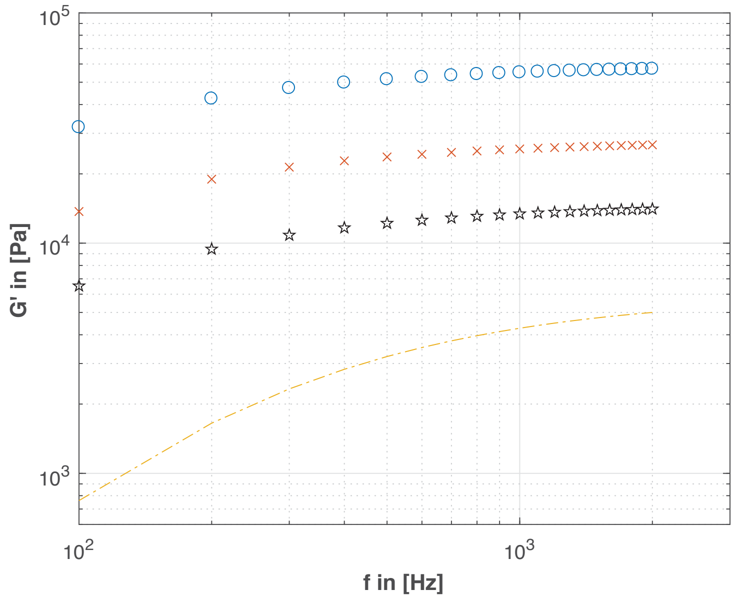

Figure 5–12: Shear modulus vs. frequency for, ∘: Silicon rubber, mixing ratio of 1:1:0 ; ×: Silicon rubber, mixing ratio 1:1:0.5 ; ☆: Silicon rubber, mixing ratio 1:1:1 ; –·: Hydrogel, mixing ratio of GCs 2.5% and Gy 0.005%.

5.3.2 Traveling compression wave method vs. Rayleigh wave method

Figure 5–13 shows the shear modulus obtained with the compression and the Rayleigh wave methods for two silicon rubber samples with different mixing ratios. The rod experimental results were significantly lower than the shear modulus obtained by using the Rayleigh wave method. The trend was the same up to 700 Hz for the silicon rubber with a mixing ratio of 1:1:0. Only the values are different. It was believed that this might be related to the influence of the Poisson ratio in the rod experiment. Due to the nature of the equations, the influence of the Poisson ratio was much greater in the rod experiment than the Rayleigh wave method. If the Poisson ratio was sightly off it had a big influence on the final material properties. It

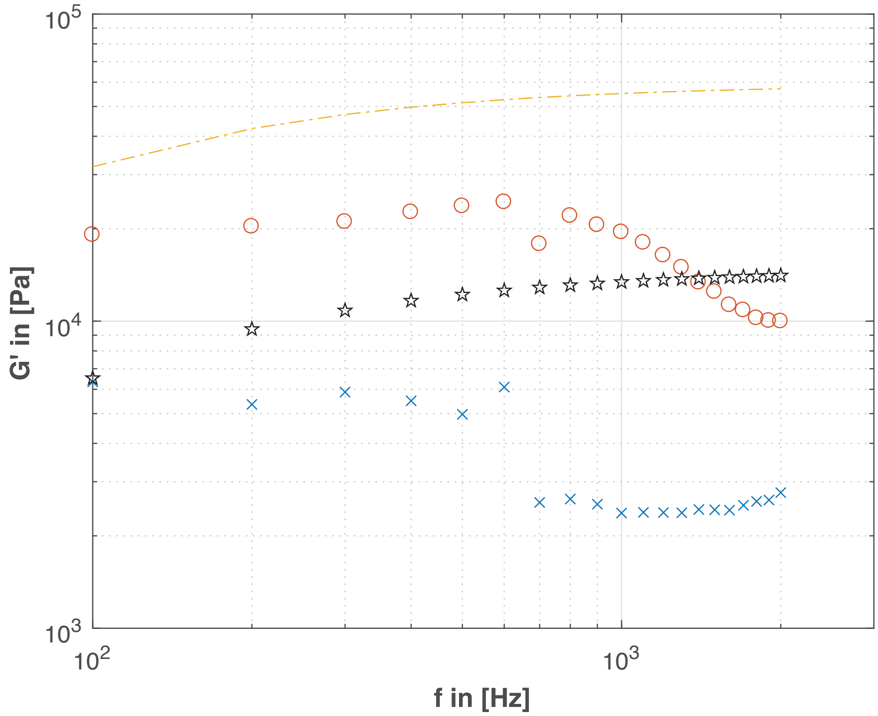

Figure 5–13: Shear modulus vs. frequency for the Rayleigh wave method and traveling compression wave method. ×: Compression wave in silicon rubber, mixing ratio of 1:1:1 ; ∘: Compression wave in silicon rubber, mixing ratio of 1:1:0 ; ☆: Rayleigh wave in silicon rubber, mixing ratio of 1:1:1 ; –·: Rayleigh wave in silicon rubber, mixing ratio of 1:1:0.

was observed that multiple waves were propagating inside the rod during the excitation. The wave speed was calculated based on the spatial Fourier transform described in Chapter 4. The resulting spectrum shows multiple waves propagating inside the sample. Shear and other wave types were present inside the rod. The angle of the shaker might have had an influence on the relative amplitude of the different wave components. This was previously observed in the Rayleigh wave experiment. If the angle between the gel and the blade was 90° the majority of the energy cascaded into the shear wave component. When the angle was change to 45° the energy cascaded into the compression wave increased but into the shear wave decreased. Therefore the Rayleigh wave was much weaker.

5.3.3 Rheometry results

The material used for all experiments was from the same lot and the samples were fabricated (cast) at the same time. All the plots in this section show the frequency-dependent shear modulus. In both the wave propagation and the torsional rheometery experiments, the response of the material under shear was measured. The shear component of the Rayleigh wave was used to obtain the response of the material per Eq. (2.43). In all cases, the modulus vs. frequency plots,

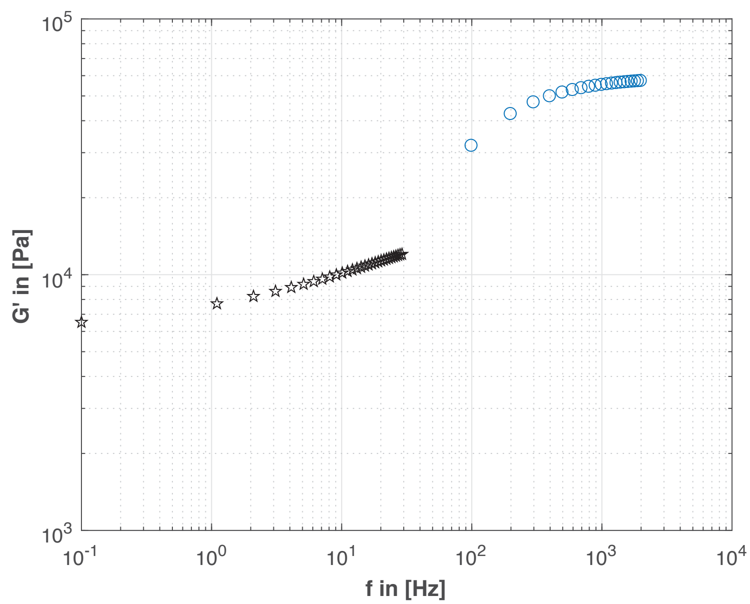

Figure 5–14: Shear modulus vs. frequency for silicon rubber with a mixing ratios of 1:1:0. ☆: representing data obtained by rheometry ; ∘: representing data obtained by Rayleigh wave propagation.

shown in Figures 5–14 trough 5–17, are in a very good agreement. The interpolation between the two different experimental results seems reasonable accurate. The

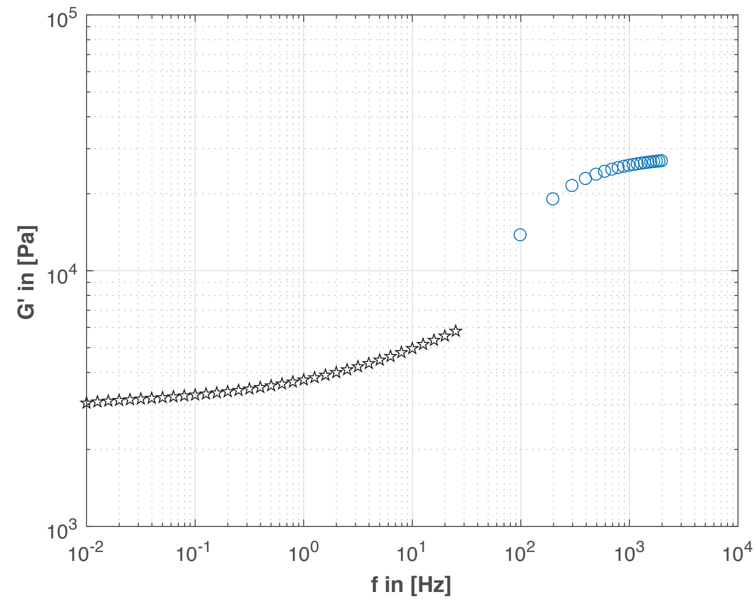

Figure 5–15: Shear modulus vs. frequency for silicon rubber with a mixing ratios of 1:1:05. ☆: obtained by rheometry ; ∘: obtained by Rayleigh wave propagation.

results in Figures 5–16 and 5–17 show a very smooth transition. The shear modulus obtained by rheometry was very typical, and can be compared with that of many other homogeneous viscoelastic materials. The stiffness increased with an increase in frequency, first slowly than faster. It was believed that this behavior is related to the time-dependent response of the material. At low frequency, the polymer chains have time to unravel and to slide relative to each other. At high frequency, the material becomes "frozen". The polymer chains do not have enough time to unravel and pull each other, which resulted in an increase in stiffness of the material. At high frequency, the obtained shear modulus using the Rayleigh wave approach follows a complementary trend. Between 100 Hz and 400 Hz, the increase is logarithmic. It is believed that at a transition point the polymer chain do not unravel anymore. The

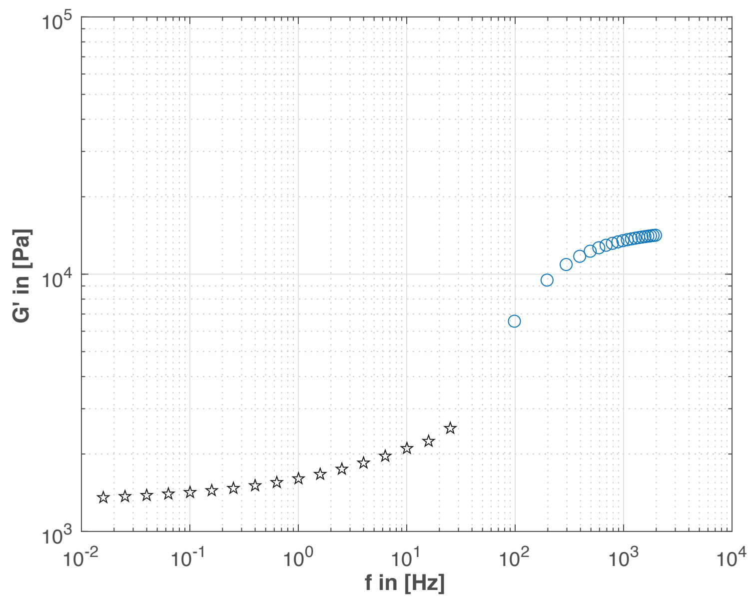

Figure 5–16: Shear modulus vs. frequency for silicon rubber with a mixing ratios of 1:1:1. ☆: obtained by rheometry ; ∘: obtained by Rayleigh wave propagation.

values asymptotically converge towards a constant value, probably representative of the polymer chains modulus.

The high frequency response corresponds to material behavior at low temperature. The temperature-frequency relation for viscoelastic material is $\frac{1}{T} \propto log(f)$, where T and f represent temperature and frequency, respectively. At low temperatures the material was very brittle and hard. It resembles more a metal than a viscoelastic material [7]. The wave propagation in a homogeneous metal is non dispersive, which is perfect agreement with observations. This specific behavior was observed for all materials tested.

The frequency-dependent shear moduli obtained by two different experimental methods were compared. The shear modulus of the Rayleigh wave method was

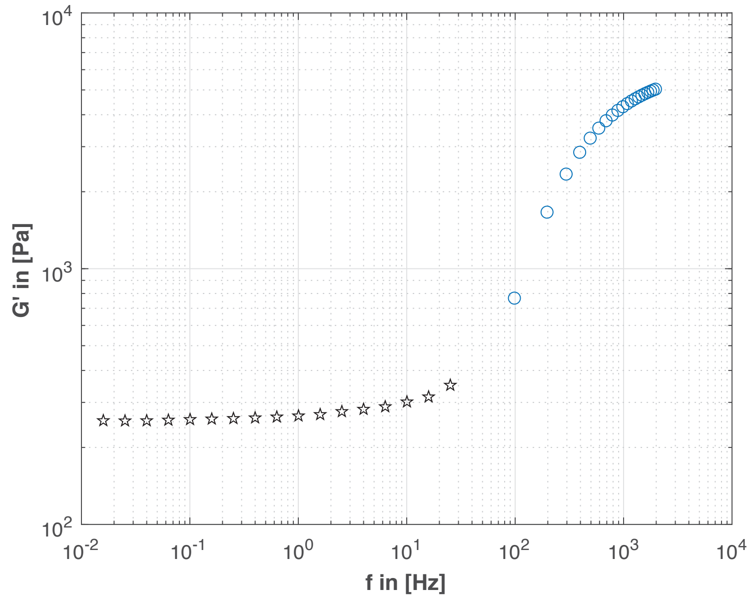

Figure 5–17: Shear modulus vs. frequency for hydrogel with a mixing ratio of GCs 2.5% and Gy 0.005%. ☆: obtained by rheometry ; ∘: obtained by Rayleigh wave propagation.

compared with shear modulus obtained by rheometry. The lower frequency limit of the Rayleigh wave method was 100 Hz and the upper limit of the rheometer was 30 Hz. This created a 70 Hz band gap. However, it was believed that the trend between the two different experiments was in agreement with each other, supporting a the validity of the Rayleigh wave method.

5.3.4 Effects of longitudinal fibers on the shear modulus

The effect of embedded nylon fibers on the material response and properties was tested. The material was prepared and cured following the procedure described in Section 3.1.3. Two different experiments were performed. The wave propagation along as well as transverse to the fiber orientation was investigated. Figure 5–18 shows the wave speed as a function of frequency. The response of the material without fibers is shown for comparison. The wave speed along the fiber direction was much higher throughout a wide frequency range than that transverse to the fiber orientation, or with no fibers. The wave speed function peaked at a frequency of 600 Hz, and started decaying afterwards. It decreased exponentially until it reached the same value as the wave speed of the fibers traverse to the wave propagation. This indicated that the influence of the fibers was highly frequency-dependent. Over the frequency range between 100 Hz and 600 Hz, the wave speed significantly increased with embedded fibers. From 600 Hz to 2000 Hz, this effect decreased exponentially. This indicated that the effect of the fibers on the wave speed was diminished until the wave speed was the same regardless of the fiber orientation. Furthermore, the wave speed along the transverse fiber orientation, and that of homogeneous silicon rubber diverged as well. The results indicated that the transverse fibers decreased the wave speed at low frequency, and increased the wave speed at high frequency. The density of the nylon fibers and silicon rubber with a mixing ratio of 1:1:0 was similar, 1259 $\frac{m}{s}$ and 1087 $\frac{m}{s}$, respectively. Density effects on the wave speed were thus unlikely.

The shear modulus is shown as a function of frequency in Figure 5–19. The same trends as in Figure 5–18 were observed. The shear modulus for the wave propagation along the fibers direction was much greater than the one of the other materials tested. The stiffness of the homogeneous material was greater at low frequency, but lower for high frequencies than the material with transverse fiber orientation.

The general conclusion from this transversely isotropic material was that the fibers have an influence on the frequency-dependent wave speed. Fibers aligned along

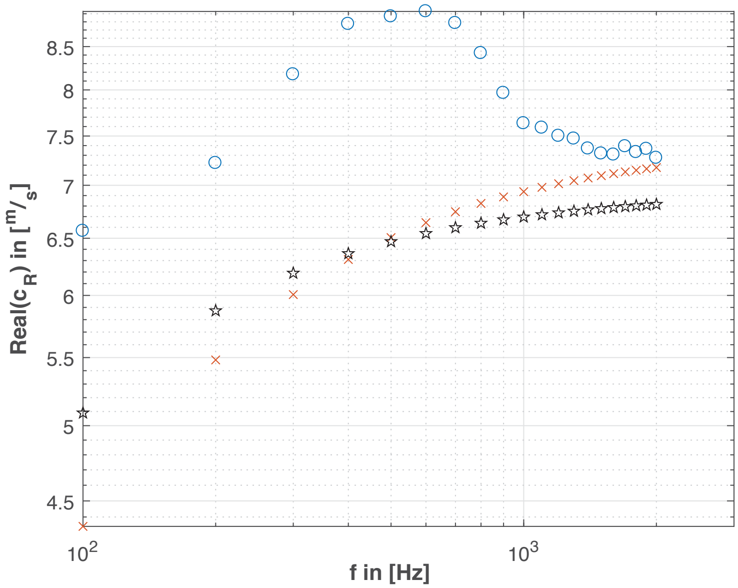

Figure 5–18: Wave speed vs. frequency for different fiber orientations. ×: Fibers transverse to the wave propagation direction ; ☆: Silicon rubber without fibers ; ∘: Fibers aligned along the wave propagation direction.

the wave propagation, stiffened the material drastically. Their influence decreased at higher frequency. Fibers perpendicular to the wave propagation softened the material for low frequency, but stiffened it drastically for high frequency. The orientation of the fibers made no difference at high frequency .

Embedding nylon fibers in a polymer matrix stiffens the material. Such fibrous polymer matrix composites are significantly lighter than comparable material with similar stiffness and strength [48]. The transversely isotropic viscoelastic material structure is hard to compare with other fibrous structures. Wood is a fibrous structure but does not have the same entanglement as polymers do. The proposed theory is based on a significantly entangled structure. Moreover, wood does not have the same matrix-fiber relationship. In the experiments performed a few fibers

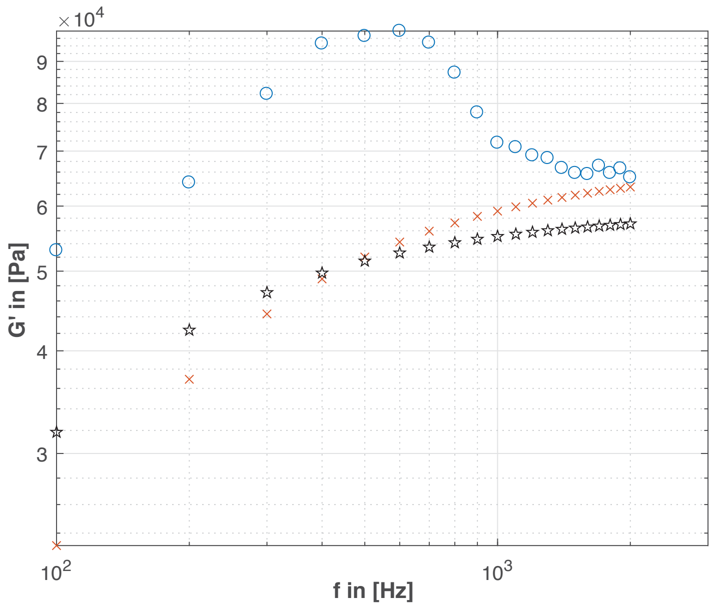

Figure 5–19: Shear modulus vs. frequency for different fiber orientations. ×: Fibers transverse to the wave propagation direction ; ☆: Silicon rubber without fibers ; ∘: Fibers aligned along the wave propagation direction.

were embedded in a large quantity of matrix. In wood, a large number of fibers are surrounded by a small quantity of matrix.

5.3.5 Two-layer method

Samples were prepared following the procedures described in Chapter 3. As for the mono-layer method, an electrodynamic shaker generated a sweep function up to 2 kHz. The wavenumber-frequency spectrum was obtained with the help of the 2D Fourier transform. Attempts were made to replicate previously published results [22], [23].

Different materials with similar Young's modulus were tested to find an optional substrate and top layer sample thickness [49]. A wide range of top layer thicknesses was investigated to understand the relation between sample thickness and substrate interactions. If the top layer sample is very thin (1 mm) the Rayleigh wave observed was exclusively dependent on the substrate used. If the thickness of the top layer was increased up to 1 cm, the wavenumber spectrum was exclusively dependent on the top layer material properties. No interaction between both substrates could be observed.

The shaker excited Rayleigh waves propagating on the surface and compression and shear waves propagating inside the material. When compression and shear waves reach the interface between two materials, they create an additional Rayleigh wave at the interface. It was believed that, for a specific thickness of the top layer, the Rayleigh wave confined to the interface may interact with the surface Rayleigh wave, although such interaction may be mitigated by the high dissipation inside the material. The Rayleigh wave at the interface might have dissipated much faster than the Rayleigh wave on the top surface. This theory was supported by the extremely high dissipation of the Rayleigh waves on the surface. Rayleigh waves above 200 Hz usually dissipated over only 2 cm. A much higher dampened interface Rayleigh wave would have dissipated even earlier.

5.4 Computational model

The simulation was performed using the model described in Chapter 4. Multiple cases were simulated with different damping coefficients and shear moduli (Table 4–1). A suitable method to calculate damping parameters α_d and β_d for the experimentally tested material was found. This approach lead to unrealistic results because no interpolation into the high frequency spectrum was not possible. However, this approach concluded in a new idea for the reverse engineering the material properties. The envelope function of the peak amplitudes was fit to the one of the experiment by adjusting the simulation parameters.

5.4.1 Rayleigh damping model

Efforts were made to quantify the damping coefficients α_d and β_d. Initially the idea was to obtain these by fitting Eq. (4.7) to the damping ratio ζ. The damping ratio ζ was calculated from the rheometry data for the different materials. It was assumed that the trend obtained by fitting Eq. (4.7) would be a good initial guess to start the simulation. Figure 5–20 shows the damping ratio, ζ, over the frequency range from 0 to 25 Hz for all four materials tested. The trend observed for all materials is exponential. The results for the three different silicons tested are almost identical. Only the hydrogel shows a different damping behavior. It was a much slower decaying exponential function. Similarities between silicon rubber damping

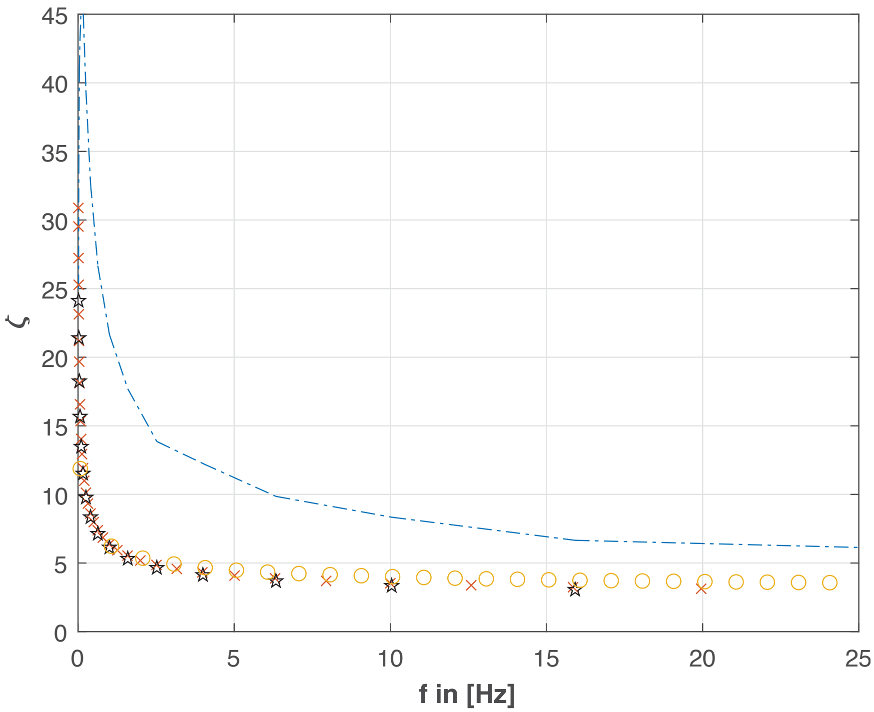

Figure 5–20: Damping ratio ζ vs. frequency. ○: Silicon rubber, mixing ratio of 1:1:0 ; ×: Silicon rubber, mixing ratio 1:1:0.5 ; ☆: Silicon rubber, mixing ratio 1:1:1 ; –·: Hydrogel, mixing ratio of GCs 2.5% and Gy 0.005%.

ratios were observed previously. The shear modulus development for all three silicon rubbers in Figure 5–12 was exactly the same, only the offset of the functions were different. That leads to the conclusion that the logarithmic increase is regulated by the damping and the final asymptotic trend towards a constant value is based on the shear modulus.

The next step was to fit Eq. (4.7) to these damping ratios. For example, the closest fit for the damping ratio of the hydrogel was obtained with $\alpha_d = 150$ and $\beta_d = 0.0914$ (Figure 5–21). For low frequency up to 0.2 Hz the fitting based on the least square method did not replicate the damping behavior. For higher frequency

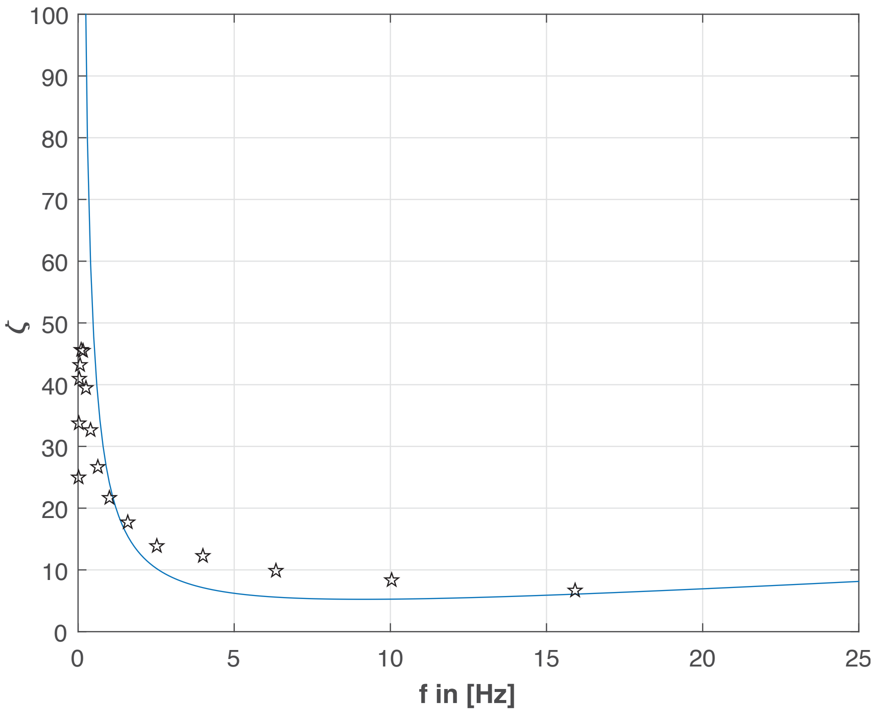

Figure 5–21: Damping ratio ζ vs. frequency. The material investigated was hydrogel with a mixing ratio of GCs 2.5% and Gy 0.005%. ☆: representing data obtained by rheometry ; −·: Fit based on least square method

of 0.2 Hz to 16.5 Hz the fit was acceptable. These values were set as initial damping parameters for the simulation. The first results obtained showed that this method was not valid to obtain reasonable initial guesses for α_d and β_d. The fitting approach was replaced by a parametric study to better understand the effect of damping and shear modulus on the wave propagation.

5.4.2 Parametric study

In the parameter study the damping coefficient and the shear modulus was varied. Other material specifications like incompressibility parameter and density were kept constant. For analytical reasons, the envelope function of the peak amplitudes for the wave propagation was plotted vs. distance traveled. The difference between Figure 5–7 and the following was that only the centerline was plot with the real displacement.

Figure 5–22 shows the effect of different Rayleigh damping parameters on the wave propagation for two frequencies, 300 Hz (a) and 600 Hz (b). The plots show the development of the envelop function of the peak amplitudes vs. distance traveled. The blade was positioned 4.2 cm from the left boundary of the setup (Figure 4–1). Two different waves, to the left and right of the blade were observed. Figure 5–22 (a) shows the peak amplitudes at 300 Hz for three different Rayleigh damping parameters. Simulation Nr. 1 had the highest amplitude along x_1 and the lowest damping value with β_d = 0.00005. Waves propagating to the left of the blade were reflected back and a standing wave pattern was observed. This is related to the fact that the blade was closer to the left boundary of the system than to the right. Simulation Nr. 4 had a greater damping of β_d = 0.0001. The standing wave pattern almost disappeared, and the amplitudes were significantly smaller. Simulation Nr. 7 had the greatest damping value of β_d = 0.00015 and the smallest amplitudes. Looking at the right of the source of excitation, the effect of the damping only influenced the amplitude development. The location of the first lobe to the right was for all simulations exactly the same.

The same behavior was observed in Figure 5–22 (b) for a frequency of 600 Hz. With increasing Rayleigh damping factor, β_d, the amplitudes decreased without effecting the positions of the side lobes. Regardless of frequency, the Rayleigh damping effected only the amplitude development. The wave speed or the wavelength of the propagating wave was not effected. Figure 5–23 shows the effect of different shear moduli on the wave propagation at two frequencies (a) 300 Hz and (b) 600 Hz. The plots show the envelop function of the peak amplitudes vs. distance traveled, similar to the previous Figure 5–22. The damping parameter, β_d, was fixed to one value and only the shear modulus G was varied. Figure 5–23 (a) shows the development at a frequency of 300 Hz. The propagation to the right of the sample was similar to the previously observed behaviors. Two lobes were identified. The major difference between the material responses was the location of the lobes. The first lobe of simulation Nr. 4, with a shear modulus of G = 10 kPa was exactly at the position of 6.04 cm. Increasing the shear modulus to G = 20 kPa in simulation Nr. 5 and to G = 40 kPa in simulation Nr. 6 shifted the lobe with each increase further away from the excitation point, to 6.97 cm and 8.41 cm, respectively. The shift of the lobe further away from the source of excitation indicated an increase in wave speed and wavelength. This is in agreement with the equation $\hat{G} = \frac{\rho\omega^2}{\hat{k}_S^2} = \rho\hat{c}_S^2 = \rho(\hat{\lambda}_S f)^2$ indicating that by increasing the shear modulus the wave speed and the wavelength had to increase, while the density, ρ, and the frequency, f, were kept constant. The amplitude of the lobes decreased when shifted to the right. The decrease in the amplitude was related to the increased distance propagated. The further the wave propagates, the more damping it experiences, which causes a shorter amplitude.

The same behavior was observed for an excitation frequency of 600 Hz in Figure 5–23 (b). With an increase in shear modulus the first side lobe, to the right of the blade, shifted from 5.23 cm to 5.546 cm and than 6.04 cm, for a shear modulus of 10 kPa, 20 kPa and 40 kPa, respectively. Thus, an increase in the damping

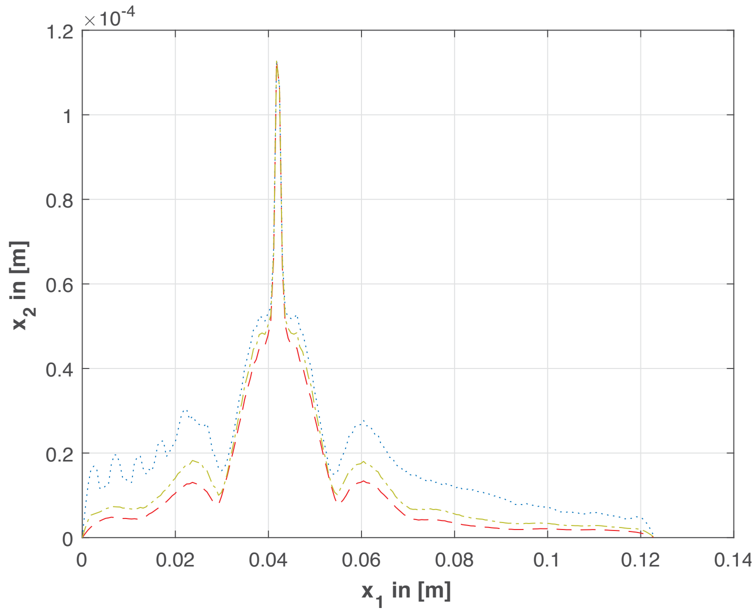

(a)

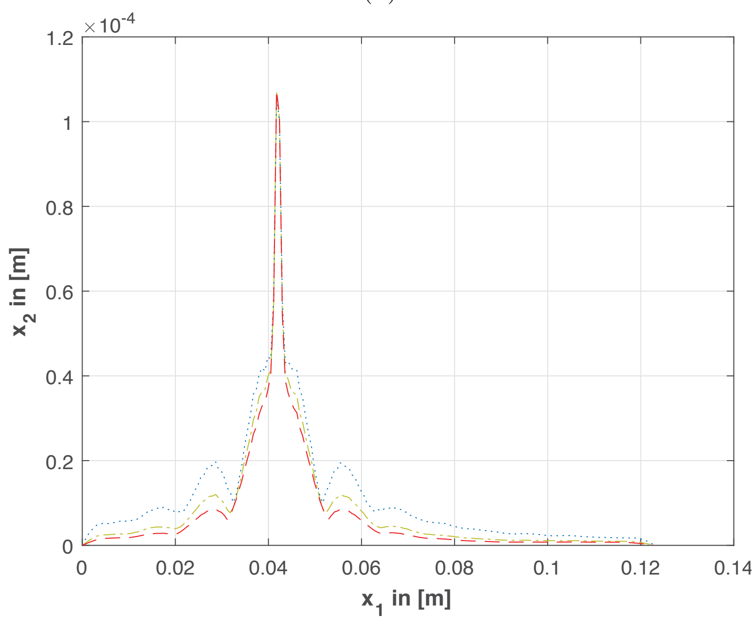

(b)

Figure 5–22: Effects of Rayleigh damping parameters on wave propagation (a) 300 Hz simulation –: Nr.1 ; –·: Nr.4 ; ·: Nr.7 (b) 600 Hz simulation –: Nr.2 ; –·: Nr.5 ; ·: Nr.8.

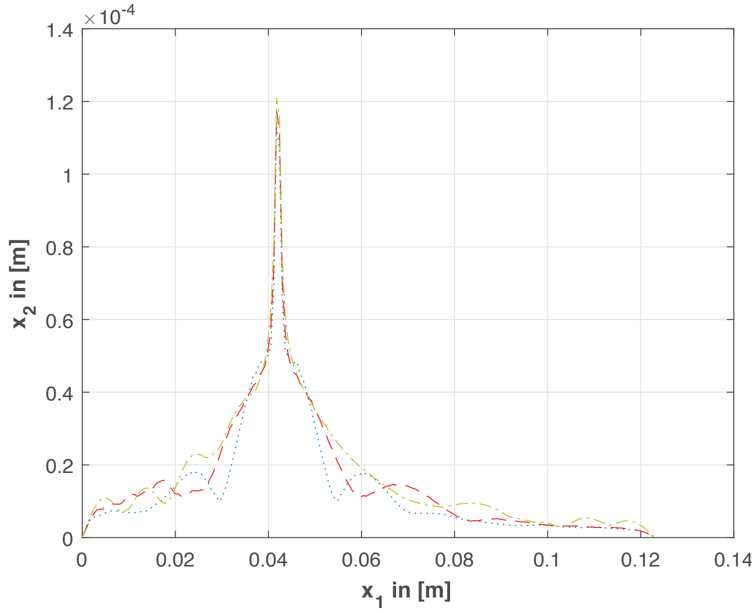

(a)

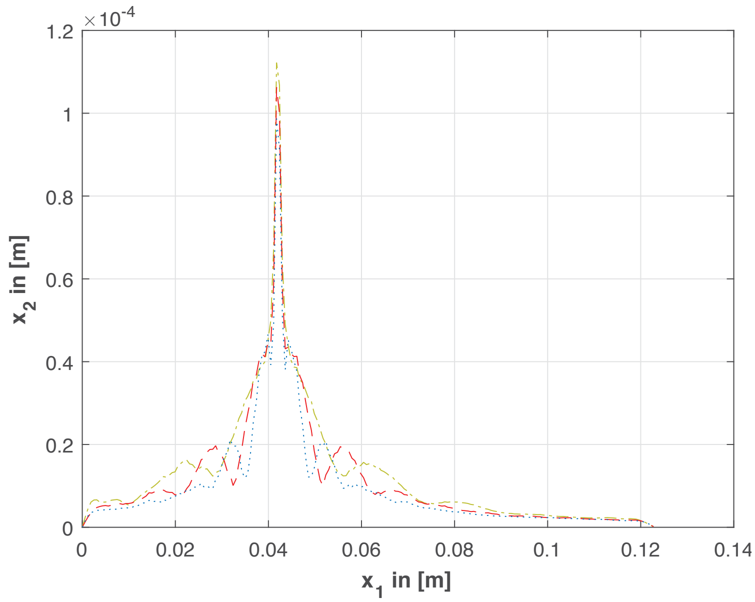

(b)

Figure 5–23: Effects of shear modulus on the envelope function of a (a) 300 Hz simulation ·: Nr.4 ; –: Nr.5 ; –·: Nr.6 and (b) 600 Hz simulation ·: Nr.7 ; –: Nr.8 ; –·: Nr.9.

coefficient, β_d, increased the dissipation and therefore shortened the amplitude of the propagating wave. It was observed that the position of the lobes did not change by manipulating β_d. Increasing the shear modulus highly effected the wave speed as well as the wavelength. The lobes shifted further from the source of excitation with each increase in shear modulus. To further investigate the conclusions made, an analysis based on the mathematical theory in chapter 2 was performed. Surface displacements of the computational models were extracted to mimic the laboratory experiment and to calculate the material properties.

Figure 5–24 shows the Rayleigh wave speed and shear modulus for all 9 simulations. The results obtained were not dependent on the damping and therefore the simulations yielded perfectly overlapping results. This was predicted by the before-mentioned analysis, because the damping did not effect the wavelength or wave speed. Simulations were grouped and plotted together. Simulation Nr.3,6,9 (Group 3) had a shear modulus of 40 kPa, Nr.2,5,8 (Group 2) of 20 kPa and Nr.1,4,7 (Group 1) of 10 kPa. In Figure 5–24 (a) the prediction show that an increase in shear modulus increased the wave speed. Group 3 has the highest shear modulus and therefore the highest reported wave speed, followed by Group 2 and Group 1. In addition, to the shift in wave speed, the shear modulus had an effect on the slope of the speed development. Group 3 with a very steep slope for a bandwidth of 100 Hz to 800 Hz distinguished itself from other groups where no obvious slope development was recognizable above 400 Hz. The interpretation can be as follows. With an increase in shear modulus, constant density and incompressibility parameter, the wave speed development took longer to reach it's final asymptotic value. That means the material was more dispersive for higher shear modulus. In Figure 5–24 (b) the asymptotic shear modulus's value at high frequency differed from the shear modulus defined in the simulation. In addition, a greater the shear modulus in the simulation caused the shear modulus calculated based on the mathematical model to diverge from the correct value. One possible explanation was that a combination of Rayleigh and body waves may have been generated. In Figure 5–7, 5–2, 5–23 (b) and 5–24 (b) the envelope functions decayed exponentially. Further investigations based on the spatial Fourier transform showed no significant additional wave at a different wave speed. It was assumed that the blade perturbation did not create the specific boundary conditions to create a perfect single Rayleigh wave. Therefore, a detailed investigation of the boundary conditions was needed.

5.4.3 Influence of boundary condition at drive point

To obtain one single Rayleigh wave, the transverse and longitudinal displacement imposed at the driving point must be consistent with Eqs. (2.36) and (2.37). However, in the experiment the surface perturbation of the shaker is purely uniaxial which is in contradiction with the displacement definition of the Rayleigh wave (Eqs. (2.36) and (2.37)). This leads to additional wave components propagating in the material as described in section 5.3.2. In fact, an exponential amplitude decay was rarely observed (Figure 5–7 and 5–2), which indicated the presence of multiple wave components.

The Rayleigh wave displacement with depth was analyzed. Plotting Eqs. (2.36) and (2.37) in Figure 5–25 revealed multiple interesting trends. It was observed that the motion of the particles was not always elliptical anti-clockwise. At a certain

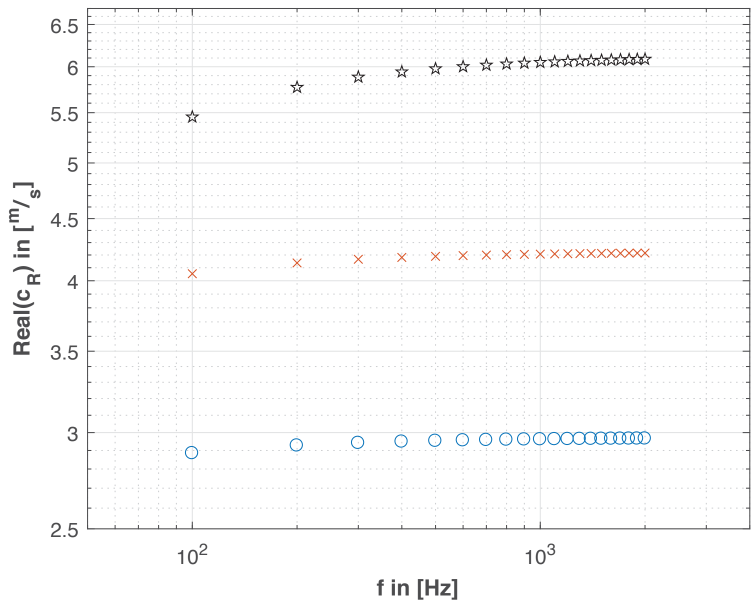

(a)

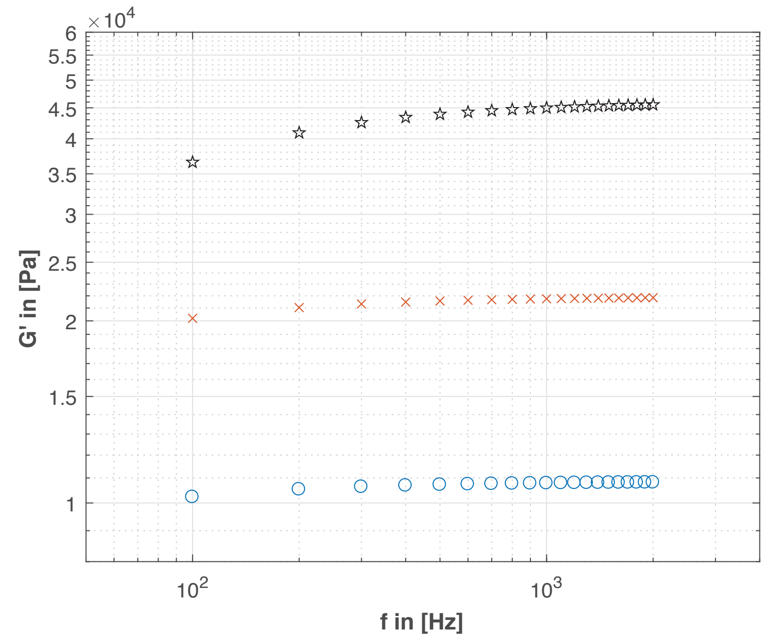

(b)

Figure 5–24: Rayleigh wave speed (a) and shear modulus (b) vs. frequency for the computational models. ☆: Nr.3,6,9 ; ×: Nr.2,5,8 ; ∘: Nr.1,4,7.

point, the motion in propagation direction became negative and therefore changed its orientation.

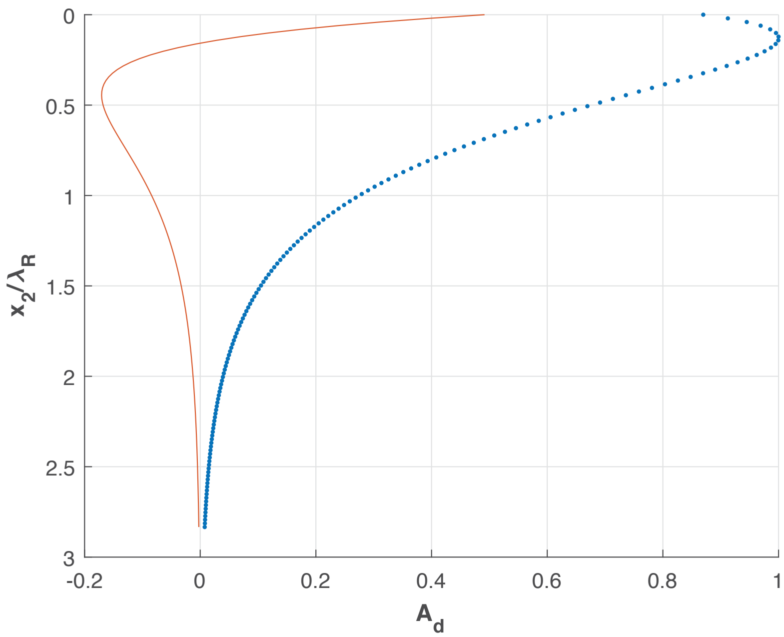

Figure 5–25: Normalized Rayleigh wave displacement A_d vs. normalized depth. –: normalized displacement along the x_1-direction ; ·: normalized displacement along the x_2-direction

The second and most significant observation was that the out-of-plane motion along the x_2-direction had it's maximum displacement below the surface of the material. Since the motion, experimentally and computationally, was a pure line source excitation without variations is depth, this fundamental characteristic of Rayleigh waves was absent. This hinted, that the difference in applied boundary conditions created additional energy, flowing into shear and compressional wave components.

Furthermore, no additional wave with different speed was visible in the wavenumber-frequency spectra, which indicates that the added body waves propagated at the same phase velocity.

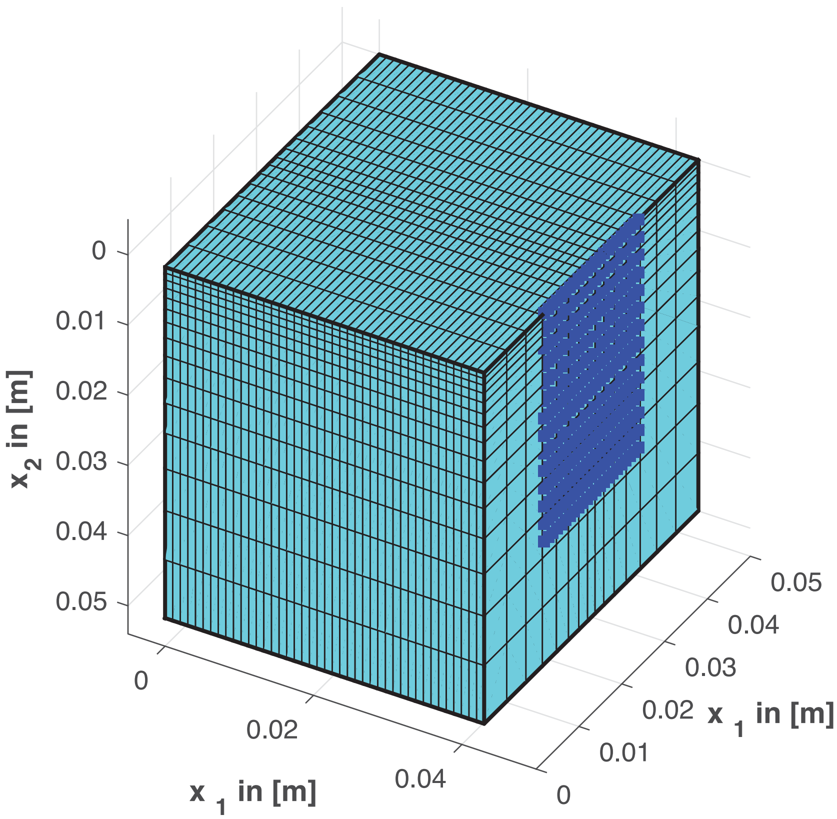

Figure 5–26: Cut of a material section, showing the individual nodes where displacements is applied. Displacement varied with depth of the material, dependent on the Rayleigh wave displacement.

To verify this hypothesis, the boundary conditions in the computational model were changed. The new boundary conditions were based on Eq. (2.37), replicating the Rayleigh out-of-plane motion, Figure 5–26. The coefficients to solve Eq. (2.37) were based on the wavenumber calculated from a computational experiment. In other words, first a simple blade excitation was performed and the specific wavenumber, characterizing the material, was identified. In the next step the wavenumber was used to solve the Rayleigh boundary condition equation. The exact Rayleigh displacement for each individual node was calculated, once the boundary conditions were solved. The result is shown in Figure 5–27. The orange dotted line represents the envelope function of the peak amplitudes when a line source excitation was applied on the surface of the sample Figure 5–26. As previously discussed, decay is not exponential. However, the blue line described the envelope function of the applied Rayleigh wave boundary condition to a cross section of the sample. The same material was tested but the results were very different. The decay with modified boundary conditions, was nearly perfectly exponential. This proved the hypothesis that the boundary conditions were responsible for the additional lobe visible in every experimentally or computationally obtained envelope function. The boundary conditions play a significant role in the development of different wave types. It was shown that with a modification into a more Rayleigh like boundary condition an almost perfect exponential decay was created and thus additional wave types propagating inside the material were eliminated. In the laboratory, it was nearly impossible to impose the Rayleigh wave conditions which were created in the simulation.

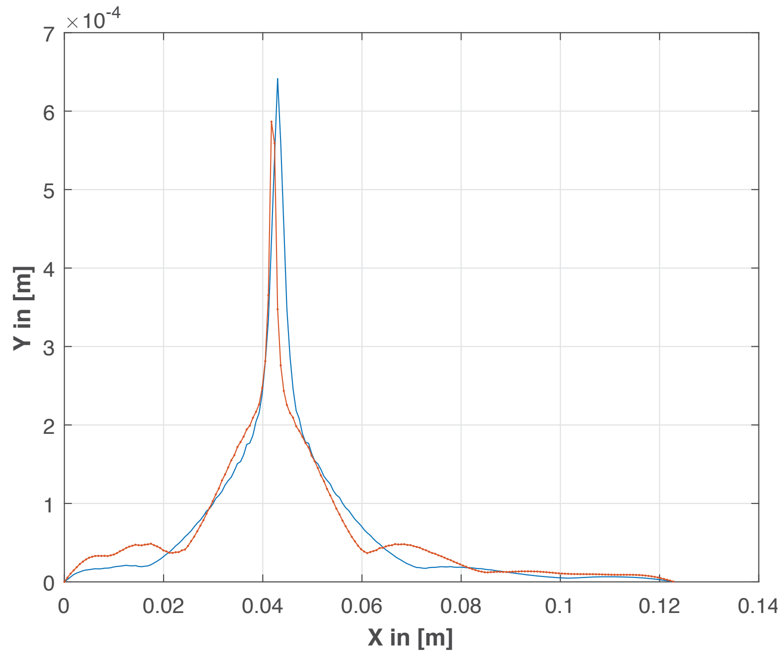

Figure 5–27: Applied Rayleigh displacement with depth compared to standard surface line source excitation. –: Rayleigh displacement with variation in depth ; –·: standard line source excitation.

CHAPTER 6
Conclusions and future work

6.1 Summary and conclusions

The goal of this thesis was to investigate the surface wave propagation behavior of viscoelastic materials and to quantify the visco-elastic properties of soft hydrogels over a frequency range up to 2 kHz. Different homogeneous and inhomogeneous materials were investigated, and their material properties quantified. A deeper understanding of the underlying physics was obtained following experimental investigations.

Firstly, a compressional wave propagation method for standing as well as traveling waves was investigated. Two cylindrical silicon rubber samples with different mixing ratio were tested. A method to calculate the response of the material based on the longitudinal wave speed was implemented. The surface displacements of the sides of the rod were measured and their cross-spectral density calculated. The wave speed and amplitude decay of the traveling compressional wave was quantified up to a frequency of 700 Hz. The wave speed for silicon rubbers with a mixing ratio of 1:1:1 and 1:1:0 reached a constant value of 5 $\frac{m}{s}$ and 10 $\frac{m}{s}$, respectively. Based on the measured wave speed, the shear modulus was calculated. The shear modulus for silicon rubbers with a mixing ratio of 1:1:1 and 1:1:0 reached a constant value of 5.5 kPa and 20 kPa, respectively. Results were compared to results obtained with the surface wave propagation. The trends were in good agreement up to a frequency of 700

Hz. Similar asymptotic trends previously observed in the Rayleigh wave propagation method were present. But the shear modulus values differed.

Based on the analytical Rayleigh wave model [31], the fundamental behavior of single- and multi-mode Rayleigh waves was elucidated. It was observed that a single Rayleigh wave has an anti-clockwise local particle motion. Moreover, the local particle motion for a multi-mode Rayleigh wave propagation is dependent on the number of different modes and the intensity. A numerical model was created with which the differentiation between different modes and their related speed were quantified.

The surface displacement created by the Rayleigh wave propagation, for four different materials was measured. The recorded data was further analyzed with the help of the cross-spectral density. A computational model was created which transformed the obtained experimental data into a wavenumber-frequency spectrum. The spectrum enabled to differentiate between waves propagating at different speeds. The wave propagation in silicon rubbers with different stiffness was investigated as well as the behavior of soft biomaterials under high frequency excitation. The wave speed in the silicon rubbers with a mixing ratio of 1:1:1, 1:1:0.5 and 1:1:0 reached a constant asymptotic value of 3.2 $\frac{m}{s}$, 4.9 $\frac{m}{s}$ and 6.5 $\frac{m}{s}$, respectively. The wave speed for the hydrogel was 2.1 $\frac{m}{s}$. Once the frequency-dependent wave speed was calculated, the material properties were obtained. The shear modulus for silicon rubbers with a mixing ratio of 1:1:1, 1:1:0.5 and 1:1:0 reached a constant asymptotic value of 15 kPa, 20 kPa and 50 kPa, respectively. The silicon rubber samples with higher ratio of silicon thinner were significantly softer and thus, had a smaller shear modulus. The hydrogel tested had the smallest shear modulus of 4 kPa. Results were compared with previous work [22] done over the same frequency range. The comparison between the results showed a good agreement for low frequencies, but no overlap for high frequencies. It was believed that the new results have a greater accuracy. The methodology followed in [22] relies on exponential regressions, which was found to be flawed.

The shear moduli of the samples tested were compared to experimental results obtained by rheometry. A good agreement between rheometry results and surface wave propagation was identified. The rheometry results complemented the low frequency spectrum of the shear modulus. The shear modulus for all materials tested was linearly increasing, complemented with a logarithmic increase and asymptotic values measured with the Rayleigh wave method. The effects of embedded fibers on the wave propagation and the material response were explored. It was observed that the alignment of embedded nylon fibers highly impacted the wave propagation and the shear modulus. When the fibers were aligned with the wave propagation the shear modulus significantly increased from 51 kPa without embedded fibers up to 100 kPa at a frequency of 600 Hz. When the fibers were transverse to the wave propagation the shear modulus increased slightly by 1 kPa. At low frequency, entangled fibers may have slipped relative passed each other, but at high frequencies cling to each other, thus stiffening the material. A two-layer method was investigated, but no interaction between multiple Rayleigh waves was observed.

Computational methods validated the observed physical behavior of the surface wave propagation. The experimentally obtained development of the peak amplitudes was successfully replicated. Frequency-dependent damping was successfully implemented to simulate viscoelastic material behavior. A high-fidelity model of the laboratory experiment was created. The same post processing as for the experimental data was applied to the computational model. Material properties were successfully obtained based on the Rayleigh wave method, validating the approach. Simulations with the shear modulus of 10 kPa, 20 kPa and 40 kPa were successfully reversely determined to yield around 11 kPa, 21 kPa and 45 kPa, respectively, at high frequency. The simulated wave propagation features were in good agreement with the one in the experiment. A parametric study showed the effect of a variation of damping and shear modulus on the wave propagation. It was observed that the Rayleigh damping only affected the amplitude development. With increasing Rayleigh damping the amplitude decreased. The shear modulus only affected the phase development. The wavelength was increased with increasing shear modulus. Different boundary conditions were investigated which explained experimental observations. The nodal surface displacement created a combination of shear and Rayleigh wave propagating at the same speed. This created an interference between wave components. It was possible to isolate the Rayleigh wave components and explain why envelope functions developed the way they did. A single Rayleigh wave excitation was found to be possible if the excitation amplitude varied with depth.

6.2 Future work

Not many experiments have covered as wide a bandwidth as the present study. Jia et al. performed experiments with a modified rheometer examining viscoelastic materials up to 500 Hz, in 2006. It would be interesting to compare the Rayleigh wave results with the results of that rheometer over the same frequency range.

An upgrade of the computational model to investigate the two-layer method seems desirable. A few test runs were performed with promising results. The focus should lay on how to choose the top layer thickness to ensure a Rayleigh wave interaction, and what the damping parameters need to be to prevent excessive dissipation. The computational model offers an ideal platform for the reverse determination of the material properties. This can be achieved by adjusting the simulation parameters (damping and shear modulus) to replicate the same envelope function of the peak amplitudes. If the envelope functions of the peak amplitudes are in agreement, one knows the material properties. The code would have to be based on an initial guess and an iterative method.

The effect of the fibrous structure should be further investigated. To further understand the effect of fibers on the material properties, the amount of fibers used, the thickness and the distance between the fibers should be varied. A further expansion of the experiment would bring light into the stated theory of matrix-fiber interaction. By using nylon fibers embedded in viscoelastic elastic material, the behaviour of fibrous tissue can be mimicked. This basic model can be linked to the mechanical behavior of collagen and elastin components in tissue [50]. A future project should be the investigation of embedding fibers in viscoelastic material to replicate tissue properties.

In future projects, the surface wave characterization method can be used to determine the change of material properties with regards to external modifications. One future project could be to investigate the effect of cells seeded in viscoelastic materials and their effect on the material properties [51]. If cells are placed in an environment they start creating an extracellular matrix (EM) in which they can move and communicate with other cells [28]. This EM might have an influence on the material properties of the gel they are seeded in [52]. The surface wave characterization method is the perfect approach the quantify this change. Lots of research has been done on human derived fibroblasts and their behaviour under induced vibration [53]. However, the effect of acoustical waves on cells is not fully understood [54]. One hypothesis to verify is that cells reacted to vibrations which directly effects the proliferation [55]. The proposed experiments could be used to investigate the effect of frequency-dependent vibrations on cells.

References

[1] N. Latifi, H. Heris, S. Kazemirad, and L. Mongeau, "Development of a self-oscillating mechanical model to investigate the biological response of human vocal fold fibroblasts to phono-mimetic stimulation," in *ASME 2014 International Mechanical Engineering Congress and Exposition: American Society of Mechanical Engineers*, 2014.

[2] N. Latifi, M. Asgari, H. Vali, and L. Mongeau, "A tissue-mimetic nano-fibrillar hybrid injectable hydrogel based on collagen type iii, collagen type i and glycol-chitosan for soft tissue engineering," *in review*.

[3] M. Khaleghi, C. Furlong, J. Cheng, and J. Rosowski, "Characterization of acoustically-induced forces of the human eardrum," in *Mechanics of Biological Systems and Materials, Volume 6*, pp. 147–154, Springer, 2016.

[4] E. Kozin, N. Black, J. Cheng, M. Cotler, M. McKenna, D. Lee, J. Lewis, J. Rosowski, and A. Remenschneider, "Design, fabrication, and in vitro testing of novel three-dimensionally printed tympanic membrane grafts," *Hearing research*, vol. 340, pp. 191–203, 2016.

[5] H. Herzel, D. Berry, I. Titze, and M. Saleh, "Analysis of vocal disorders with methods from nonlinear dynamics," *Journal of Speech, Language, and Hearing Research*, vol. 37, no. 5, pp. 1008–1019, 1994.

[6] A. Chan, L. Mongeau, and K. Kost, "Vocal fold vibration measurements using laser doppler vibrometry," *The Journal of the Acoustical Society of America*, vol. 133, no. 3, pp. 1667–1676, 2013.

[7] N. Lagakos, J. Jarzynski, J. Cole, and J. Bucaro, "Frequency and temperature dependence of elastic moduli of polymers," *Journal of applied physics*, vol. 59, no. 12, pp. 4017–4031, 1986.

[8] J. Park, *Effects of mechanical properties of sealing systems on aerodynamic noise generation inside vehicles*. PhD thesis, 2002.

[9] M. Kimura, T. Mau, and R. Chan, "Viscoelastic properties of phonosurgical biomaterials at phonatory frequencies," *The Laryngoscope*, vol. 120, no. 4, pp. 764–768, 2010.

[10] T. Royston, Z. Dai, R. Chaunsali, Y. Liu, Y. Peng, and R. Magin, "Estimating material viscoelastic properties based on surface wave measurements: A comparison of techniques and modeling assumptions," *The Journal of the Acoustical Society of America*, vol. 130, no. 6, pp. 4126–4138, 2011.

[11] R. Chan and I. Titze, "Hyaluronic acid (with fibronectin) as a bioimplant for the vocal fold mucosa," *The Laryngoscope*, vol. 109, no. 7, pp. 1142–1149, 1999.

[12] R. Chan and I. Titze, "Viscosities of implantable biomaterials in vocal fold augmentation surgery," *The Laryngoscope*, vol. 108, no. 5, pp. 725–731, 1998.

[13] R. Chan and I. Titze, "Viscoelastic shear properties of human vocal fold mucosa: measurement methodology and empirical results," *The Journal of the Acoustical Society of America*, vol. 106, no. 4, pp. 2008–2021, 1999.

[14] S. Klemuk and I. Titze, "Viscoelastic properties of three vocal-fold injectable biomaterials at low audio frequencies," *The Laryngoscope*, vol. 114, no. 9, pp. 1597–1603, 2004.

[15] X. Jia, Y. Yeo, R. Clifton, D. S. Jiao, T.K., J. Kobler, S. Zeitels, and R. Langer, "Hyaluronic acid-based microgels and microgel networks for vocal fold regeneration," *Biomacromolecules*, vol. 7, no. 12, pp. 3336–3344, 2006.

[16] T. Pritz, "Transfer function method for investigating the complex modulus of acoustic materials: rod-like specimen," *Journal of Sound and Vibration*, vol. 81, no. 3, pp. 359–376, 1982.

[17] C. Lai and G. Rix, *Simultaneous inversion of Rayleigh phase velocity and attenuation for near-surface site characterization.* School of Civil and Environmental Engineering, Georgia Institute of Technology Georgia, 1998.

[18] S. Foti, *Multistation methods for geotechnical characterization using surface waves.* PhD thesis, Politecnico di Torino, 2000.

[19] L. Kinsler, A. Frey, A. Coppens, and J. Sanders, "Fundamentals of acoustics," *Fundamentals of Acoustics, 4th Edition, by Lawrence E. Kinsler, Austin R. Frey, Alan B. Coppens, James V. Sanders, pp. 560. ISBN 0-471-84789-5. Wiley-VCH, December 1999.*, p. 560, 1999.

[20] J. Achenbach, *Wave propagation in elastic solids*, vol. 16. Elsevier, 2012.

[21] L. Boeckx, P. Leclaire, P. Khurana, C. Glorieux, W. Lauriks, and J. Allard, "Investigation of the phase velocities of guided acoustic waves in soft porous layers," *The Journal of the Acoustical Society of America*, vol. 117, no. 2, pp. 545–554, 2005.

[22] S. Kazemirad and L. Mongeau, "Rayleigh wave propagation method for the characterization of a thin layer of biomaterials," *The journal of the Acoustical Society of America*, vol. 133, no. 6, pp. 4332–4342, 2013.

[23] S. Kazemirad, *Wave Propagation Methods for the Experimental Characterization of Soft Biomaterials and Tissues*. PhD thesis, McGill University, 2014.

[24] N. Gucunski and R. Woods, "Use of rayleigh modes in interpretation of sasw test," *Proc. of the 2nd Int. Conf. on Recent Advances in Geotechnical Earthquake Engineering and Soil Dynamics*, pp. 1399–1408, 1991.

[25] G. Bhashyam, "Ansys mechanicala powerful nonlinear simulation tool," *ANSYS Inc, Canonsburg, PA*, 2002.

[26] S. Adhikari, *Damping models for structural vibration*. PhD thesis, University of Cambridge, 2001.

[27] I. Chowdhury and S. Dasgupta, "Computation of rayleigh damping coefficients for large systems," *The Electronic Journal of Geotechnical Engineering*, vol. 8, no. 0, pp. 1–11, 2003.

[28] Y. Luo, J. Xia, R. Miller, J. Liu, Y. Xu, and Q. Liu, "Application of high-resolution linear radon transform for rayleigh-wave dispersive energy imaging and mode separating," in *SEG Technical Program Expanded Abstracts 2008*, pp. 1233–1237, Society of Exploration Geophysicists, 2008.

[29] J. Bolton and Y. Kim, "Visualization of the tire vibration and sound radiation and modeling of tire vibration with an emphasis on wave propagation," tech. rep., 2003.

[30] J. Capon, "High-resolution frequency-wavenumber spectrum analysis," *Proceedings of the IEEE*, vol. 57, no. 8, pp. 1408–1418, 1969.

[31] E. Zabolotskaya, Y. Ilinskii, T. Hay, and M. Hamilton, “Greens functions for a volume source in an elastic half-space,” *The Journal of the Acoustical Society of America*, vol. 131, no. 3, pp. 1831–1842, 2012.

[32] H. Zhao, M. Urban, J. Greenleaf, and S. Chen, “Elasticity and viscosity estimation from shear wave velocity and attenuation: a simulation study,” in *Ultrasonics Symposium (IUS), 2010 IEEE*, pp. 1604–1607, IEEE, 2010.

[33] I. Cremer and M. Heckl, “Definition, measurement, and generation of structure-borne sound,” in *Structure-Borne Sound*, pp. 1–74, Springer, 1988.

[34] T. Kundu, *Ultrasonic nondestructive evaluation: engineering and biological material characterization*. CRC press, 2003.

[35] K. Graff, *Wave motion in elastic solids*. Courier Corporation, 2012.

[36] A. Mal and S. Singh, *Deformation of elastic solids*. Prentice Hall, 1991.

[37] D. Hesse and P. Cawley, “Surface wave modes in rails,” *The Journal of the Acoustical Society of America*, vol. 120, no. 2, pp. 733–740, 2006.

[38] P. Nicholson and R. Strelitzki, “On the prediction of youngs modulus in calcaneal cancellous bone by ultrasonic bulk and bar velocity measurements,” *Clinical rheumatology*, vol. 18, no. 1, pp. 10–16, 1999.

[39] G. Kino, *Acoustic waves: devices, imaging and analog signal processing*. No. 43 KIN, 1987.

[40] N. Apetre, M. Ruzzene, L. Jacobs, and J. Qu, “Measurement of the rayleigh wave polarization using 1d laser vibrometry,” *NDT & E International*, vol. 44, no. 3, pp. 247–253, 2011.

[41] K. Addo and P. Robertson, “Shear-wave velocity measurement of soils using rayleigh waves,” *Canadian Geotechnical Journal*, vol. 29, no. 4, pp. 558–568, 1992.

[42] W. Lauriks, L. Boeckx, and P. Leclaire, “Characterization of porous acoustic materials,” in *SAPEM 2005 Symposium on the Acoustics of Poro-Elastic Materials*, 2005.

[43] T. Pritz, “Measurement methods of complex poisson’s ratio of viscoelastic materials,” *Applied acoustics*, vol. 60, no. 3, pp. 279–292, 2000.

[44] Y. Fan, S. Dixon, R. Edwards, and X. Jian, "Ultrasonic surface wave propagation and interaction with surface defects on rail track head," *Ndt & E International*, vol. 40, no. 6, pp. 471–477, 2007.

[45] J. Allard, G. Jansens, G. Vermeir, and W. Lauriks, "Frame-borne surface waves in air-saturated porous media," *The Journal of the Acoustical Society of America*, vol. 111, no. 2, pp. 690–696, 2002.

[46] N. Geebelen, L. Boeckx, G. Vermeir, W. Lauriks, J. Allard, and O. Dazel, "Near field rayleigh wave on soft porous layers," *The Journal of the Acoustical Society of America*, vol. 123, no. 3, pp. 1241–1247, 2008.

[47] J. Bendat and A. Piersol, *Random data: analysis and measurement procedures*, vol. 729. John Wiley & Sons, 2011.

[48] R. Lakes, *Viscoelastic materials*. Cambridge University Press, 2009.

[49] L. Boeckx, P. Leclaire, C. Glorieux, W. Lauriks, and J. Allard, "Measuring the dynamic shear modulus of poroelastic foams in the audible frequency range," in *18th International Congress on Acoustics (ICA2004)*, 2004.

[50] E. Breen, "Mechanical strain increases type i collagen expression in pulmonary fibroblasts in vitro," *Journal of applied physiology*, vol. 88, no. 1, pp. 203–209, 2000.

[51] J. K. Kutty and K. Webb, "Vibration stimulates vocal mucosa-like matrix expression by hydrogel-encapsulated fibroblasts," *Journal of tissue engineering and regenerative medicine*, vol. 4, no. 1, pp. 62–72, 2010.

[52] D. Kim, J. Lim, and S. Kwon, "Development of vibrational culture model mimicking vocal fold tissues," *Annals of biomedical engineering*, vol. 44, no. 10, pp. 3136–3143, 2016.

[53] J. Wolchok, C. Brokopp, C. Underwood, and P. Tresco, "The effect of bioreactor induced vibrational stimulation on extracellular matrix production from human derived fibroblasts," *Biomaterials*, vol. 30, no. 3, pp. 327–335, 2009.

[54] N. Juncosa-Melvin, K. Matlin, R. Holdcraft, V. Nirmalanandhan, and D. Butler, "Mechanical stimulation increases collagen type i and collagen type iii gene expression of stem cell–collagen sponge constructs for patellar tendon repair," *Tissue engineering*, vol. 13, no. 6, pp. 1219–1226, 2007.

[55] J. Gaston, B. Rios, R. Bartlett, C. Berchtold, and S. Thibeault, "The response of vocal fold fibroblasts and mesenchymal stromal cells to vibration," *PloS one*, vol. 7, no. 2, p. e30965, 2012.

Appendices

APPENDIX A
Matlab code

Matlab version 2016b for Windows operating system.

A.1 Green's function implementation

```

% Clear Working space
clc;
clear;
close all;

%% Constants
fs= 2^12; % Sampling rate
sec=5; % Simulate 5 seconds of propagation
Col=1; % Number of columns travers propagation direction
Row=100; % Number of rows in propagation direction
P=Col*Row; % Number of total points measured
rho = 1011; % Specimen density in kg/meter^3
poisson=0.4; % Poisson ratio
L2=0.000762; % Distance between points
k=(2-2*poisson)/(1-2*poisson);
```

```
%% Greens function based on Zabolotskaya et al., 2011

yy= 300; % Defined frequency
r= 0.00001:L2:Row*L2; % Array points in Row
rr= 0.0015875; % Radius plunger diameter
xx= 0.015875; % Displacement of plunger in meter
Q= pi * rr^2 * xx; % Volume velocity
omegaR = 2*pi*yy; % Radial frequency
k1=1000; % Defined wavenumber
k2=700;

for k_R = [k1,k2]
c_R= omegaR/k_R;% Rayleigh wave speed
xi= 0.95;
xi_l= sqrt( 1 - xi^2 * k^-1 );
xi_t= sqrt( 1 - xi^2 );
eta= -2 * sqrt( 1 - xi^2 ) / ( 2-xi^2 );
c_t= c_R/xi;
c_l= c_t * sqrt(k);
s= -rho * c_l^2 * Q / ( 1i * omegaR);
u0= 1 / ( sqrt(2) * pi ) * ( xi_t + 1 / xi_t + eta^2 * (
    xi_l + 1 / xi_l ) + 4*eta )^-0.5;
```

```
P11= ( xi_t + eta ) * (hilbert( k_R^2 * besselj(1,abs(k_R)*r) * sign(k_R)) + 1i * k_R^2 * besselj(1,abs(k_R)*r) * sign(k_R)) ;
P22= -1i * k_R^2 * ( 1 + eta * xi_l ) * besselh(0,2,abs(k_R * r));
Gr=( pi^2 * s * eta * u0^2 ) / ( rho * c_l^2 ) * P11;
Gz=( pi^2 * s * eta * u0^2 ) / ( rho * c_l^2 ) * P22;

if k_R == k1
Gz1=Gz;%/(max(Gz));
end
if k_R == k2
Gz2=Gz;%/(max(Gz));
end
end

v = VideoWriter('peaks.avi');
open(v);
delete(gcp('nocreate'))
fId = figure('position',[200 -200 550 450],'Visible','on');
axis tight manual
ax = gca;
ax.NextPlot = 'replaceChildren';
```

```
for t=0:1/10000:0.0003
T=exp(1i*omegaR*t);
figure(fId);
%disp vs distance
Uz1=T.*Gz1;
Uz2=T.*Gz2;
Ur=T.*Gr;
hold on
plot(r+Ur,Uz1,'ko');
title('Surface displacement','FontWeight','bold');
grid on
axis([0 max(r) -0.000015 0.000015])
%axis([-0.000008 0.000008 -0.00008 0.00008])
ylabel('Disp. (m)');
xlabel('length axis of specimen (m)');


frame = getframe(gcf);
writeVideo(v,frame);
end

for p=1:length(r)
```

```
io=1;
for t=0:1/fs:sec
U(p,io)=Gz(p)*exp(1i*omegaR*t);
io=io+1;
end
ACCn(:,p)=real(U(1,:));
LDVn(:,p)=real(U(p,:));
end

%% Splitting signals to several segments
Ns=5;
Np=2^12;
for it=1:length(r)
for k = 1
for kk = 1:Np
% B1s(kk,it,k) = U(it,kk);
B1s(kk,it,k) = LDVn(kk,it);
B2s(kk,it,k) = ACCn(kk,it);
end
end
for k = 2:Ns
for kk = 1:Np
B1s(kk,it,k) = LDVn(((k-1)/2)*Np+kk,it);
```

```
B2s(kk,it ,k) = ACCn(((k-1)/2)*Np+kk,it);
end
end
end

%% Windowing Han
Wh = hann(Np,'periodic');
for it=1:length(r)
for k = 1:Ns
for d = 1:Np

B1s(d,it ,k) = B1s(d,it ,k).*Wh(d);
B2s(d,it ,k) = B2s(d,it ,k).*Wh(d);

end
end
end

%% Creating 2D Matrix
for ix=1:Ns
p=1;
for iz=1:length(r)
ML(:,iz ,ix)=B1s(:,p,ix);
```

```
MA(:,iz,ix)=B2s(:,p,ix);
p=p+1;
end
end

%% FFT in time
s = size(ML);
for ix=1:Ns
FFT_MA1(:,:,ix)=fft(MA(:,:,ix),[],1);
FFT_ML1(:,:,ix)=fft(ML(:,:,ix),[],1);
FFT_F1(:,:,ix)=sqrt(8/3)*(FFT_ML1(:,:,ix)./FFT_MA1(:,:,ix));
end

%% ZeroPadding
Zero_Padd=5;
FFT_F1(:,Row:Row*Zero_Padd,:)=0;
Row=length(r)*Zero_Padd;
P=Row*Col;
ss1=size(FFT_F1);

%% Spatial windowing:
% win=tukeywin(ss1(2));
% for ix=1:Ns
```

```
%       for poi=1:length(FFT_F1(:,1,1))
%         for poi1=1:ss1(2)
%         FFT_F11(poi,poi1,ix)=FFT_F1(poi,poi1,ix)*win(poi1);
%         end
%       end
% end

%% FFT in space
for ix=1:Ns
FFT_F(:,:,ix)=fft(FFT_F1(:,:,ix),[],2)/(ss1(2));
end

%% Amplitude correction
for ix=1:Ns
FFT_F(:,:,ix) = sqrt(8/3)*FFT_F(:,:,ix);
end

%% Averaging
FFT_AV = mean(FFT_F,3);

%% Spacing
Kx_s = 1 / L2;
f=fs*linspace(-0.5,0.5,ss1(1));
```

```
kx=Kx_s*linspace(-0.5,0.5,ss1(2));
Nf = length(f);
Nx = length(kx);

%% Surface plot
[c ff] = min(abs(f-yy));
[f_m, kx_m] = meshgrid(f,kx);
Z = reshape(FFT_AV(1:Nf,1:Nx),Nf,Nx);

%% Plotting spatial FFT
To=fftshift(abs(Z));
figure
surf(f_m', -kx_m'*2*pi, fftshift(abs(Z)),'EdgeColor','none',
    'LineStyle','none');
Title=[ 'Normal,Row=' num2str(Row) ',Col=' num2str(Col) ',
    Freq=' num2str(yy) 'Hz'];
title(Title)
set(gca,'xlim',[f(ff)-0.01 f(ff)+0.01])
set(gca,'ylim',[-real(k_R)-1000 real(k_R)+1000])
caxis([0, max(To(ff,:))])
set(gca,'zlim',[0, max(To(ff,:))])
ylabel('Spatial Frequency')
xlabel('Time Frequency')
```

```
TT=fftshift(abs(Z));
[o,gg]=min(abs(f-100));
figure
plot(kx*2*pi,TT(gg,:))
set(gca,'xlim',[0 max(kx*2*pi)])
```

A.2 Spatial FFT for separate frequency excitation

```
clc;
clear;
close all;

%% Const
Fs =  2^13;
S = 10*2^13;
G1 = 0.005;    % LVD gain in (m/s)/V
G2 = 0.01062; % Accelerometer gain in reading the
    acceleration in mV/(m/s^2)

%% Import
Col=1;
Row=100;
P=Col*Row;
```

```
Zero_Padd=8;
whertobegin=1;
rho = 1011;
poisson=0.4;
L2=0.0004445;
k=(2-2*poisson)/(1-2*poisson);

poi=1;
for  yy=300
Col=1;%Orthogonal to Blade
Row=100;%Parallel to Blade
P=Col*Row;
p1=[ 'FirstOutput_' num2str(yy) '_Hz_P.tdms'];
[finalOutput,metaStruct] = TDMS_readTDMSFile(p1);
Data = TDMS_readTDMSFile(p1);
data=Data.data;

p=1;
for it=3:3:length(data)
T1=data(it);
T2=data(1+it);
TT1=T1{1,1};
TT2=T2{1,1};
```

```
LDVn(:,p)=TT1(Fs+1:S)*G1;
ACCn(:,p)=TT2(Fs+1:S-1)/G2;

p=p+1;
end

%% Zero padding
s9=size(ACCn)

%% Velocity to Acceleration

for it=1:P
B1(1,it)=LDVn(1,it)*Fs;
for ii = 2:length(LDVn)-1
B1(ii,it)=(LDVn(ii,it)-LDVn(ii-1,it))*Fs;
end
end

%% Acceleration to Velocity
% for it=1
% for ii = 1:40960-1
%    V1(ii,it)= sum(ACCn(1:ii,it)+ACCn(2:ii+1,it))/2.0/Fs;
%    V1_LDV(ii,it)= sum(B1(1:ii,it)+B1(2:ii+1,it))/2.0/Fs;
```

```
% end
% end
%
% V1 = detrend(V1);
%
% t= (1:length(V1))';
% opol= 120;
% [p,s,mu]= polyfit(t,V1,opol);
% f_y = polyval(p,t,[],mu);
% V1d= V1 - f_y;

%% velocity to dist
% for ii = 1:40960-2
%    D1(ii,it) = sum(V1(1:ii,it)+V1(2:ii+1,it))/2.0/Fs;
% end
% D1= detrend(D1);
% t= (1:length(D1))';
% opol= 120;
% [p,s,mu]= polyfit(t,D1,opol);
% f_y= polyval(p,t,[],mu);
% D1 = D1 - f_y;

```

```
clear LDVn s9 TT2 TT1 T2 T1 data Data p1 finalOutput
    metaStruct
%% Splitting signals to several segments
Ns=300;
Np=400;
for it=1:P
for k = 1
for kk = 1:Np
B1s(kk,it,k) = B1(kk,it);
B2s(kk,it,k) = ACCn(kk,it);
end
end
for k = 2:Ns
for kk = 1:Np
B1s(kk,it,k) = B1(((k-1)/2)*Np+kk,it);
B2s(kk,it,k) = ACCn(((k-1)/2)*Np+kk,it);
end
end
end

clear B1
%% Windowing (Han)
Wh = hann(Np,'periodic');
```

```
for it=1:P
for k = 1:Ns
for d = 1:Np
B1s(d,it,k) = B1s(d,it,k).*Wh(d);
B2s(d,it,k) = B2s(d,it,k).*Wh(d);
end
end
end

%% Creating 3D Matrix
for ix=1:Ns
p=1;
for iz=1:Row
for iy=1:Col
ML(:,iz,ix)=B1s(:,p,ix);
MA(:,iz,ix)=B2s(:,p,ix);
p=p+1;
end
end
end
clear B1s B2s ACCn
for ix=1:Ns
for iz=2:2:Row
```

```
ML(:,iz,ix)=ML(:,iz,ix);
MA(:,iz,ix)=MA(:,iz,ix);
end
end

%% FFT
for ix=1:Ns
FFT_MA1(:,:,ix)=fft(MA(:,:,ix),[],1);
FFT_ML1(:,:,ix)=fft(ML(:,:,ix),[],1);
FFT_F1(:,:,ix)=sqrt(8/3)*(FFT_ML1(:,:,ix)./FFT_MA1(:,:,ix));
end

rrr=linspace(0,1,100)*L2;
test=mean(FFT_F1,3);
rrr=linspace(0,100,100)*L2;
test=mean(FFT_F1,3);
f1=linspace(0,1,length(FFT_MA1(:,1,1)))*Fs;

for i=1:length(FFT_MA1(:,1,1))
tt2(i,:)=unwrap(angle(test(i,:)));
tt3(i,:)=unwrap(abs(test(i,:)));
end
for gi=1:P
```

```
jj=yy;
%finding phase shift and amplitude for point 1
for ee=30:-0.1:0
if find(yy-ee<f1 & f1<yy+ee)
else
phase(1,jj)=find(yy-(ee+0.1)<f1 & f1<yy+(ee+0.1));
ff = phase(1,jj);
break;
end
end
end

t4=tt2(ff,:);
figure
plot(tt2(ff,:))
hold on
figure
plot(tt3(ff,:))
hold on
(tt2(ff,36)-tt2(ff,35))/L2
clear ML MA FFT_MA1 FFT_ML1

```

```
FFT_F1(:,Row:Row*Zero_Padd,:)=0;
Row=Row*Zero_Padd;
P=Row*Col;

for iyy=whertobegin;
ss1=size(FFT_F1);
FFT_F=1;
clear FFT_F
for ix=1:Ns
FFT_F(:,:,ix)=fft(FFT_F1(:,iyy:ss1(2),ix),[],2)/(ss1(2));
end
s=size(FFT_F);
clear FFT_F1

%% Averaging
FFT_AV = mean(FFT_F,3);
s1=size(FFT_AV);
Kx_s = 1 / L2;
f=Fs*linspace(-0.5,0.5,s1(1));
kx=Kx_s*linspace(-0.5,0.5,s1(2));
Nf = length(f);
Nx = length(kx);
[c ff] = min(abs(f-yy)); %point of interest
```

```
%% Surface plot

[f_m, kx_m] = meshgrid(f,kx);
Z = reshape(FFT_AV(1:Nf,1:Nx),Nf,Nx);
TT21=fftshift(abs(Z));
%contourf(f_m', -kx_m', fftshift(abs(Z)),'EdgeColor','none
    ','LineStyle','none');
% surf(f_m', -kx_m', fftshift(abs(Z)),'EdgeColor','none','
    LineStyle','none'); %filter outliers
%surf(f_m',kx_m',fftshift(abs(mean(FFT_F1(:,:,2,:),4))),'
    EdgeColor','none','LineStyle','none');
%surf(f_m',kx_m',fftshift(angle(mean(FFT_F1(:,:,2,:),4))),'
    EdgeColor','none','LineStyle','none');
% Title=[ 'Zoom,Freq=' num2str(yy) 'Hz,Row=' num2str(Row) ',
    Excluded points=' num2str(iyy) ',Distance from blade='
    num2str(L2*iyy) 'm'];
% title(Title)
% view([100,10,10])
% caxis([0, max(TT21(ff,:))])
%colormap(jet(4))
% set(gca,'zlim',[0 max(TT21(ff,:))])
% view([100,5,10])
```

```
%set(gca, 'ZScale', 'log')
% set(gca,'xlim',[f(ff) f(ff)+0.1])
%set(gca,'xlim',[f(ff)-0.01 f(ff)+0.01])
%set(gca,'ylim',[-max(kx)*2*pi max(kx)*2*pi])
% set(gca,'ylim',[0 800])
% ylabel('Spatial Frequency')
% xlabel('Time Frequency')
end
clear FFT_AV Wh Z Kx_s
T91(poi,:)=TT21(ff,:);
poi=poi+1;
end
for i=1:15
figure
plot(-kx,T91(i,:))
set(gca,'xlim',[0 800])
xlabel('Spatial frequency in m^{-1}')
ylabel('Relative amplitude')
Title=[ 'Wavenumber specctrum for ' num2str(i*100) 'Hz'];
title(Title)
grid on
end
```